



저작자표시-비영리-동일조건변경허락 2.0 대한민국

이용자는 아래의 조건을 따르는 경우에 한하여 자유롭게

- 이 저작물을 복제, 배포, 전송, 전시, 공연 및 방송할 수 있습니다.
- 이차적 저작물을 작성할 수 있습니다.

다음과 같은 조건을 따라야 합니다:



저작자표시. 귀하는 원저작자를 표시하여야 합니다.



비영리. 귀하는 이 저작물을 영리 목적으로 이용할 수 없습니다.



동일조건변경허락. 귀하가 이 저작물을 개작, 변형 또는 가공했을 경우에는, 이 저작물과 동일한 이용허락조건하에서만 배포할 수 있습니다.

- 귀하는, 이 저작물의 재이용이나 배포의 경우, 이 저작물에 적용된 이용허락조건을 명확하게 나타내어야 합니다.
- 저작권자로부터 별도의 허가를 받으면 이러한 조건들은 적용되지 않습니다.

저작권법에 따른 이용자의 권리는 위의 내용에 의하여 영향을 받지 않습니다.

이것은 [이용허락규약\(Legal Code\)](#)을 이해하기 쉽게 요약한 것입니다.

[Disclaimer](#)

공학박사 학위논문

A Novel Design and Optoelectronic
Analysis of Inverted Organic Light
Emitting Diodes for Efficient Flexible
and Transparent Devices

고효율의 유연한 소자 및 투명 소자 구현을 위한
인버티드 유기 발광 다이오드의 새로운 구조 설계
및 광전자 특성 분석

2014 년 2 월

서울대학교 대학원

재료공학부 하이브리드재료 전공

이 정 환

A Novel Design and Optoelectronic Analysis of Inverted Organic Light Emitting Diodes for Efficient Flexible and Transparent Devices

지도 교수 김 장 주

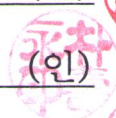
이 논문을 공학박사 학위논문으로 제출함
2014 년 2 월

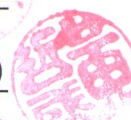
서울대학교 대학원
재료공학부 하이브리드재료 전공
이 정 환

이정환의 공학박사 학위논문을 인준함
2014 년 2 월

위 원 장 _____ 조 원 호 (인) 

부위원장 _____ 김 장 주 (인) 

위 원 _____ 박 수 영 (인) 

위 원 _____ 황 철 성 (인) 

위 원 _____ 유 승 협 (인) 

Abstract

A Novel Design and Optoelectronic Analysis of Inverted Organic Light Emitting Diodes for Efficient Flexible and Transparent Devices

Jeong-Hwan Lee

Department of Materials Science and Engineering

The Graduate School

Seoul National University

Inverted organic light emitting diodes (OLEDs), combined with oxide thin film transistors (TFTs), are one of the most promising candidates for next generation displays and lighting devices such as flexible and transparent OLEDs. In spite of their importance, inverted OLEDs have not been actively investigated because of their relatively lower efficiency compared to conventional OLEDs. If the efficiency of inverted OLEDs can be significantly improved, the technological boundaries of the applications for OLEDs can be extended since simple and new devices will be realizable.

In this dissertation, a novel design of inverted OLEDs has been described to

improve the efficiency of the devices. The main issue for iOLEDs is the electron injection from the bottom electrode to the organic layer due to the high energy barrier between them compared to those of conventional OLEDs. To overcome this problem, n-type doped organic layers have been widely adopted between the electrode and the organic layer to reduce the electron injection barrier. Unfortunately, it induces another energy barrier between the doped and undoped organic junctions, which influences the efficiency of inverted OLEDs. The importance of the energy barrier in homo-junctions as well as the interface between the cathode and the n-doped organic layer for efficient electron injection into an emitting layer have described in **chapter 2**. In addition, by properly selecting an electron transporting material that has no energy barrier in organic homo-junctions, a high performance inverted green emission OLED with a maximum External Quantum Efficiency (EQE) of 20% and a maximum power efficiency of 80 lm/W was realized.

A new method for efficient electron injection independent of the work function (W_F) of the bottom electrode is proposed using an organic p-n junction in **chapter 3**. The organic p-n junction is composed of a p-CuPc/n-Bphen layer that shows very efficient charge generation under a reverse bias reaching 100 mA/cm² at 0.3 V, and efficient electron injection from indium tin oxide (ITO) when adopted in inverted OLEDs. This is a valuable advantage for flexible displays.

Inverted OLEDs with oxide TFTs are very proper in transparent active matrix OLEDs (AMOLEDs) due to the high transmittance of the oxide TFTs in visible light unlike other opaque TFTs. Unfortunately, transparent OLEDs have rarely been demonstrated because of the serious damage that can occur during the sputtering process in the formation of transparent conducting electrodes on organic layers. In

chapter 4, 1, 4, 5, 8, 9, 11-hexaazatriphenylenehexacarbonitrile (HATCN) was successfully introduced as an efficient organic buffer layer. HATCN, a discoid organic molecule, effectively protected the underlying organic emission layers from damage caused by the sputter deposition of the indium zinc oxide (IZO) top electrode, and simultaneously showed good hole injection performance from the transparent top electrode into an organic hole transporting layer. As a result, a high performance transparent inverted OLED with a total maximum luminance efficiency of 67 cd/A, and power efficiency of 67 lm/W was realized, and these are the highest values among the reported ones up to now. Moreover, transparent inverted OLEDs showed an average transmittance of around 81% in the visible range; this value is very close to that of ITO/glass itself. To reveal the reason of the high performance transparent inverted OLED, the molecular alignment and nanostructure of HATCN thin films were directly examined using the grazing incidence wide-angle x-ray scattering method in **chapter 5**. HATCN molecules were found to be stacked with a (001)_{hex} preferred orientation on organic surfaces and the orientation was maintained with increasing thickness, in contrast to growth on metal surfaces. The structure factor from the grazing incidence small-angle x-ray scattering measurement indicated that the HATCN films formed with regularly distributed nanograins on a hydrophobic organic surface. The nanograins maintained their arrangement, even after forming the IZO electrode on the HATCN film via the sputtering process. As a result, the transparent inverted OLED described in chapter 4 showed high performance without leakage currents due to the effective protection of the organic layers by the HATCN layer.

The best efficiency of the inverted OLEDs has been reported in the literature as being as high as 20%, which is 1.5 times lower than that of conventional OLEDs because the charge balance in the inverted OLEDs is very sensitive due to the problematic electron injection. Therefore, a new structural design is required to improve the efficiency in the inverted OLEDs. One solution is use of an exciplex co-host with a phosphorescent dopant as an emitting layer. Based on the exciplex co-host system and the methods discussed in the previous chapter, recently, a highly efficient inverted top-emitting OLED with a maximum EQE of 23.4%, a power efficiency of 75 lm/W, and low efficiency roll-off up to 20,000 cd/m² was realized. In **chapter 6**, the recombination and emission mechanisms of the OLEDs were investigated to unveil the reasons behind high performance OLEDs with the exciplex forming co-host based on the current–voltage–luminance characteristics in a diffusion current region, transient electroluminescence and capacitance measurements. In the study, two different PhOLEDs with a single host, 4,4'-Bis(carbazol-9-yl)biphenyl, and an exciplex-forming co-host were investigated. The trap-assisted recombination with the large amount of trapped charges is dominant in the PhOLED with the single host due to the large energy gap between the host and dopant states. The recombination characteristics were not different from prevailing most PhOLEDs reported up to now. In contrast, the bimolecular Langevin recombination is dominant in the PhOLED with the exciplex forming co-host, although phosphorescent dye is doped in the co-host. As a result, the accumulated charge density is lower in the co-host system than the single host Emissive Layer (EML), leading simultaneously to the high efficiency and the extremely low efficiency roll-off.

Keywords: inverted organic light emitting diode, transparent organic light emitting diode, flexible device, recombination and emission mechanism, electron injection

Student Number: 2010-30783

Contents

Abstract	i
Contents	vi
List of Tables	ix
List of Figures	x
Chapter 1. Introduction	1
1.1 Organic light emitting diodes.....	1
1.1.1. Brief history of OLEDs	1
1.1.2. Classification of OLEDs.....	2
1.2 Operating principles of OLEDs	5
1.2.1. Understanding of <i>J-V</i> characteristics in OLEDs.....	5
1.2.2. External quantum efficiency of OLEDs	8
1.2.3. Energy transfer between host and dopant materials	11
1.3 Inverted OLEDs for flexible devices	14
1.4 Issues in inverted OLEDs	20
1.5 Outline of thesis	26
Chapter 2. A high performance inverted OLED using an electron transporting material with low energy barrier for electron injection	28
2.1 Introduction.....	28
2.2 Experimental	30
2.3 Result and Discussion	32
2.4 Conclusion	45

Chapter 3. An organic p-n junction as an efficient and cathode independent electron injection layer for flexible inverted OLEDs	46
3.1 Introduction.....	46
3.2 Experimental	49
3.3 Result and Discussion	50
3.4 Conclusion	58
Chapter 4. A high performance transparent inverted OLED with 1, 4, 5, 8, 9, 11-hexaazatriphenylene-hexacarbonitrile as an organic buffer layer	59
4.1 Introduction.....	59
4.2 Experimental	63
4.3 Result and Discussion	65
4.4 Conclusion	75
Chapter 5. Molecular alignment and nanostructure of HATCN thin films on organic surfaces	76
5.1 Introduction.....	76
5.2 Experimental	79
5.3 Result and Discussion	80
5.4 Conclusion	93
Chapter 6. Langevin and trap-assisted recombination in phosphorescent OLEDs	94
6.1 Introduction.....	94
6.2 Experimental	96

6.3	Result and Discussion	99
6.3.1.	Device performance of the green PhOLEDs	99
6.3.2.	Determination of the recombination type in the PhOLEDs.....	101
6.3.3.	Time resolved electroluminescence.....	104
6.3.4.	Analysis of trapped charges from C-V measurements	110
6.4	Conclusion	113
Chapter 7. Summary and Outlook		114
Bibliography		117
초 록	130
CURRICULUM VITAE		133
List of Publications.....		135
List of Presentations.....		139
List of Patents		144
Acknowledgement (감사의 글).....		145

List of Tables

Table 1. Characteristics of inverted OLEDs with three different electron transporting materials (ETMs).	44
Table 2. The morphology characteristics of the two thin films from the AFM measurement before and after O ₂ plasma treatment. R _{pv} is the value of the peak to valley roughness, and R _{rms} is the value of the root mean square roughness.	74

List of Figures

Fig. 1.1 Outlines of the OLEDs.....	4
Fig. 1.2 Current density-Voltage (J - V) characteristics of the OLEDs can be distinguished as three parts; Ohmic, diffusion dominated, and space charge limited current region depending on the external voltage bias. The energy level alignment of the device also described here in the case of (1) $V \sim 0V$, (2) $V = V_{bi}$, and (3) $V > V_{bi}$, respectively.	6
Fig. 1.3 Emission patterns depending on the dipole orientation. (a) A light emitted from the vertically oriented dipoles is guided through the parallel direction with respect to the substrate, and (b) a light from the horizontally oriented dipoles is effectively emitted out to the air. (c) Contour plots as a function of the orientation of the dipoles and their PL quantum efficiency taken from [23].....	10
Fig. 1.4 Schematic illustration of (a) Förster and (b) Dexter energy transfer mechanisms, respectively.....	13
Fig. 1.5 Comparison of the technological suitability among different backplane technology. [Source: IDTechEx, 31].....	17
Fig. 1.6 Schematic diagrams of pixel circuit for active matrix OLED (AMOLED). (a) n-type TFT connected with inverted OLED, (b) n-type TFT connected with conventional OLED. (c) Image sticking test using circuit (a), and (d) using circuit (b), respectively. Images taken from [32,33].....	18
Fig. 1.7 Compensation circuits for AMOLED based on the oxide (IGZO) TFTs with OLEDs from (a) Samsung Display and (b) Sharp and	

Semiconductor Energy Laboratory (SEL). Images taken from [35,36]	19
.....	19
Fig. 1.8 Schematic diagram of (a) pixel of flexible AMOLED, taken from [37]	
(b) energy diagram of inverted OLEDs, and (c) energy diagram of	
conventional OLEDs.....	21
Fig. 1.9 (a) <i>J-V</i> characteristics of electron only device depending on the	
deposition sequence of LiF layer. Image is taken from [38] (b) The	
device structures used in (a).....	22
Fig 2.1 (a) The device structure of the iOLEDs with three different ETMs. (b)	
HOMO and LUMO levels of the ETMs and illustration of n-doping via	
charge transfer from the LUMO level of Rb ₂ CO ₃ to the ETMs.	37
Fig. 2.2 The <i>J-V-L</i> characteristics of the iOLEDs with three different ETMs,	
B3PYMPM (square), Bphen (circle), and TPBi (triangle), respectively.	
In addition, closed symbols represent the <i>J-V</i> curves and open symbols	
denote the <i>L-V</i> curves, respectively.....	39
Fig. 2.3 (a) The device structures of two different electron only devices. (b)	
the <i>J-V</i> characteristics of the electron only devices with Bphen (square),	
B3PYMPM (circle), and TPBi (triangle). Closed symbols are for the	
type 1 and open symbols denote for the type 2 of the electron only	
devices, respectively. (c) It can be inferred that the results of (b) are	
attributed to the energy barrier between the n-ETL/ETL junctions	40
Fig. 2.4 Developments of UPS spectra near (1) the onset and (2) the valence	
band region of (a) ITO/n-B3PYMPM/B3PYMPM, (b) ITO/n-	
Bphen/Bphen, and (c) ITO/n-TPBi/TPBi structures, respectively. The	
inset shows the resulting energy level alignment, and all binding	

energies are referenced to the Fermi level (EF) of ITO. The vacuum level (VL) shift and HOMO level position can be analysed with increment of thickness of organic material, and they are indicated with vertical lines, respectively. The valance band regions are focused to analyse the behaviour of energy level movements in detail.43

Fig. 2.5 (a) EQE vs. Luminance, and (b) the current and power efficiency vs. current density of the three different iOLEDs with B3PYMPM (square), Bphen (circle), and TPBi (triangle). In Fig. 2.5(b), closed symbols represent the current efficiency and open symbols are depicted the power efficiency, respectively.47

Fig. 2.6 Semi-log plots of EL spectra of the iBOLEDs with (a) B3PYMPM, (b) Bphen, and (c) TPBi, respectively, depending on the applied current density. The extra emission near 430 nm was only observed in (a), and the emission was originated from the exciplex formed between B3PYMPM/CBP interfaces.....48

Fig. 2.7 The energy level diagram of the CBP, Ir(ppy)₃, B3PYMPM, and exciplex formed by CBP and B3PYMPM, respectively. The energy level of the exciplex was obtained from the PL measurement at low temperature. The radiative and non-radiative decays are additionally illustrated based on the energy transfer mechanism, and the figure is taken from [27].....49

Fig. 3.1 Illustration of an inverted OLED device with a p-n junction as an electron injection layer (EIL). The organic p-n junction acts as an EIL by generating an electron hole pair at the junction under reverse bias with negligible voltage loss to perform as an efficient EIL.51

Fig. 3.2 (a) The current density-voltage (J - V) characteristics of two different devices with organic p-n junctions of ITO/p-MeO-TPD (15 nm)/n-Bphen (30 nm)/Al and ITO/p-CuPc (15 nm)/n-Bphen (30 nm)/Al, respectively. (b) Comparison of the J - V characteristics of the ITO/n-Bphen (30 nm)/Al device and ITO/p-CuPc (15 nm)/n-Bphen (30 nm)/Al device under negative bias on the ITO electrode.52

Fig. 3.3 (a) Current density-voltage-luminance (J - V - L) characteristics and (b) current and luminous efficiencies of the iOLEDs with p-CuPc/n-Bphen (device A) and n-Bphen (device B) as the electron injection layer, respectively.....54

Fig. 3.4 Schematic diagrams illustrating the electron injection mechanism in (a) a normal electrode/organic junction and (b) an electrode/p-n junction.....55

Fig. 3.5 (a) Current density–voltage (J – V) characteristics and (b) luminance–voltage (L – V) characteristics of the inverted OLEDs with n-Bphen (devices C and D) and p-CuPc/n-Bphen (devices E, F, and G) as the electron injection layer fabricated on UV- O_3 treated (devices D and E) and non-treated ITO electrodes (devices C and F) and on PEDOT:PSS (device G), respectively. (c) The work function of the bottom electrodes are indicated.57

Fig. 4.1 Optimized structure of the transparent inverted OLED and the molecular structure of the organic materials.64

Fig. 4.2 Contour plots of luminance efficiencies (LEs) of the transparent OLEDs as functions of the hole transporting layer and electron transporting layer thicknesses, according to the emission direction; (a)

is the case of bottom emission, (b) is the case of top emission, and (c) is of sum of both directions.66

Fig. 4.3 The electrical and optical characteristics of the transparent inverted OLED; (a) current density-voltage-luminance (*J-V-L*) characteristics, and (b) current and power efficiencies, depending on the emission direction, bottom emission through the glass substrate (square), top emission through the IZO electrode (circle), and total sum of both emission (triangle).....68

Fig. 4.4 Transmittance of (a) the transparent inverted OLED and (b) the ITO/glass itself in the visible light region, and photographs before and after turn-on of the device. The average transmittance of the device is about 81%, and the value is represented as the dashed line.....70

Fig. 4.5 Surface morphology and phase images of a 40 nm thick TAPC film on ITO ((a) and (b), respectively), and a 50 nm thick HATCN grown on the ITO/TAPC (40 nm) ((d) and (e), respectively) measured using an AFM, before O₂ plasma treatment. After the O₂ plasma treatment, the morphology of (c) the TAPC thin film is significantly changed compared to that of (f) the HATCN thin film.73

Fig. 5.1 GISAXS images measured at a 0.142° incidence angle. (a), (b) Two HATCN films, 20 nm and 50 nm thick, respectively, were grown on a 20 nm thick TAPC layer. (c) A 10 nm thick IZO layer was grown on a 50 nm thick HATCN film, which had been grown on a 20 nm thick TAPC layer. (d)–(f) 50 nm thick HATCN films grown on 20 nm thick B3PYMPM, Bphen, and TPBi layers, respectively. (g) Horizontal line cuts (dotted lines in (a)–(c)) of the GISAXS images of the HATCN

films on a TAPC layer show the separated wings corresponding to regularly distributed HATCN nano-grains.....	81
Fig. 5.2 Distilled water contact angle for TAPC, Bphen, B3PYMPM, TPBi, and HATCN, respectively.....	83
Fig. 5.3 (a) x-ray off-specular reflection data for the 20 nm and 50 nm thick HATCN layers grown on a 20 nm thick TAPC layer. The intensity modulations correspond to the 10 nm thick IZO layer grown on the HATCN layers. (b) Schematic diagram showing the specular and off- specular reflectivity in reciprocal space. (c)–(f) AFM images of the sample surfaces: TAPC/HATCN (20 nm), TAPC/HATCN (50 nm), TAPC/HATCN (20 nm)/IZO (10 nm), TAPC/HATCN (50 nm)/IZO (10 nm), respectively.	84
Fig. 5.4 Schematic diagrams of the HATCN nanograins on a 20 nm thick TAPC layer, based on the analysis of the GISAXS data. The morphology of the IZO layer grown by sputtering followed the HATCN nanograin morphology.	86
Fig. 5.5 The phase image of (a) TAPC (40 nm), (b) TAPC/HATCN (20 nm), and (c) TAPC/HATCN (50 nm), respectively, from AFM measurement. The figure (d) show the line scan images from the figure (b) and (c), respectively.....	88
Fig. 5.6 Open symbols show Power Spectral Density (PSD) profiles of TAPC/HATCN (20 nm) and TAPC/HATCN (50 nm) films, respectively, from AFM measurements. Red line shows the simulation data using ABC model.	89

Fig. 5.7 (a) GIWAXS data of a 50 nm thick HATCN film grown on a 20 nm thick TAPC layer. (b) Reciprocal space of a preferentially ordered HATCN film with (001). In this configuration, (001) peaks are observed in the normal direction, while (hk0) peaks are observed in the horizontal direction, respectively.	91
Fig. 5.8 Crystal size of 50 nm thick HATCN films grown on different organic layers. Error values are also summarized.....	92
Fig. 6.1 Device structures, the energy levels of each layer, and the molecular structures of the two different PhOLEDs.....	98
Fig. 6.2 (a) <i>J-V-L</i> characteristics and (b) (semi-log scale) EQE-luminance (η - <i>L</i>) characteristics of the TCTA:B3PYMPM:Ir(ppy) ₂ (acac) based PhOLED (device 1) and the CBP:Ir(ppy) ₂ (acac) based PhOLED (device 2). The inset of Fig. 2(b) is depicted in a linear scale.	100
Fig. 6.3 (a) <i>J-V-L</i> characteristics of the two PhOLEDs in diffusion dominated current region. (b) The recombination parameter (η) was calculated from Fig. 6.3(a) by using equation (2).	103
Fig. 6.4 Normalized intensity of transient EL, depending on the reverse bias after turn-off of the voltage pulse in (a) device 1 and (b) device 2. The voltage pulse width was 100 μ s and the pulse frequency was 100 Hz. The voltage pulse height corresponds to a current density of 10 mA/cm ² . The magnitude of the reverse bias after the voltage turn-off was gradually increased up to saturation. The initial overshoots caused by the trapped charges in the emission layer are observed only in device 2, and they gradually decrease as the reverse bias magnitude increases.	105

Fig. 6.5 Normalized transient EL intensity depending on the frequency of the voltage pulse in (a) device 1, and (b) device 2. The voltage pulse width was 100 μ s and the voltage pulse height corresponds to a current density of 10 mA/cm². The frequency of the voltage pulse was gradually increased from 100 Hz to 900 Hz. The initial part of the transient EL was magnified, as shown in the inset. The initial overshoots are still observed and the luminance onset time gradually increases as the frequency increases in device 2. In contrast, there are no changes in device 1 that depend on variation of the frequency.....106

Fig. 6.6 Normalized intensity of the transient EL at the decay part, depending on the reverse bias of the voltage pulse after turn-off in (a) device 1, and (b) device 2.....108

Fig. 6.7 Capacitance-voltage (C-V) plots and current density-voltage curves for the two different PhOLEDs112

Chapter 1. Introduction

1.1 Organic light emitting diodes

1.1.1. Brief history of OLEDs

Organic light emitting diodes (OLEDs) convert electrical energy into light through the recombination of injected charges in emitting layers under electrical excitation. Although organic materials for OLEDs are electrically insulator due to large band gap of about 2–3 eV and their conductivity is much lower, by a factor of as much as 10^3 – 10^6 , when compared to that of metal or inorganic semiconductors, interestingly, OLEDs emit light rather efficiently.

The discovery of this contradictory finding in organic materials was introduced by Tang *et al.* in 1987.¹ The first OLED introduced by Tang *et al.* was composed of bi-layered organic structures with a hole transporting layer (HTL) and electron transporting layer (ETL). Unfortunately, however, the efficiency of the device was very low less than one percent because the fluorescence from a singlet exciton was only harvested due to the forbidden relaxation of triplets in the system. Therefore, this is regarded as the first generation of OLEDs.

To activate the radiative decay of phosphorescence, Baldo *et al.* introduced 2, 3, 7, 8, 12, 13, 17, 18-octaethylporphine platinum (II) (PtOEP) dye.² The heavy metal (platinum or iridium)–based organometallic compounds emitted phosphorescent light even at room temperature due to strong spin-orbit coupling. This was the first phosphorescent OLED (PhOLED) and is regarded as the second generation of

OLEDs. They opened the way to the achievement of almost 100% internal quantum efficiency of the OLEDs. After their pioneering work, the efficiency of PhOLEDs has been significantly improved (by 30%)³⁻⁵, but PhOLEDs still have too many stability issues for practical applications, particularly in blue-emitting OLEDs. An alternative way to improve both the stability and efficiency of OLEDs is harvesting triplet excitons by converting them to singlet excitons via a reverse intersystem crossing (RISC).⁶ This is the third generation of OLEDs, and has recently garnered tremendous attention, particularly for blue emitting OLEDs. The operating principle and the emission mechanism of the OLEDs will be further discussed in the next sections.

1.1.2. Classification of OLEDs

OLEDs consist of multilayered organic layers between conductive metal electrodes. Depending on the direction of light propagation with respect to the substrate, OLEDs are mainly classified into “top emitting” and “bottom emitting,” as shown in **Fig. 1.1**. Light is emitted through the transparent bottom electrode in the bottom emitting OLEDs, and are emitted through the transparent top electrode in the top emitting OLEDs. Both OLEDs contain one reflective metal electrode, and one transparent electrode. For AMOLEDs, top-emitting OLEDs integrated with an opaque transistor backplane are preferred to bottom emitting OLEDs to obtain a high aperture ratio.

When both electrodes are transparent, light is emitted in both directions simultaneously. This is called a transparent OLED, and they are being developed for

new technologies such as smart windows, head-up displays, and augmented reality applications. In addition, OLEDs are classified as inverted or conventional (normal) OLEDs according to the position of the cathode (anode) and the deposition sequence of the organic layers. Inverted OLEDs (iOLEDs) have a reversed sequence of organic layers compared to conventional OLEDs with respect to bottom electrode, leading to electron (hole) injection from bottom (top) electrode to electron (hole) transporting organic layers.

The first conventional OLED was invented by Tang *et al.*, in 1987 as mentioned before, and has been very actively studied to investigate mechanisms for improvement of the device in the academic research field. In addition, it is a commercial success in the market. The first iOLED was introduced by Baigent *et al.* in 1994.⁷ The structure of the device was a top emitting iOLED using a high-electron-affinity conjugated polymer, cyano-polyphenylene vinylene (CN-PPV), on an aluminum (Al) cathode to enhance the electron injection from bottom electrode to the organic layer. But still, improving the electron injection to achieve a good charge balance is the main issue for iOLEDs, and has to be overcome in order to make highly efficient iOLEDs. In 1996, Bulovic *et al.* made the first transparent OLED by using a semitransparent electrode composed of indium tin oxide (ITO) on a Mg-Ag thin layer.⁸ However, the fabrication conditions of transparent OLEDs are very sensitive compared to other OLEDs due to the remarkable damage that can occur during the sputtering process for the formation of transparent top electrode.

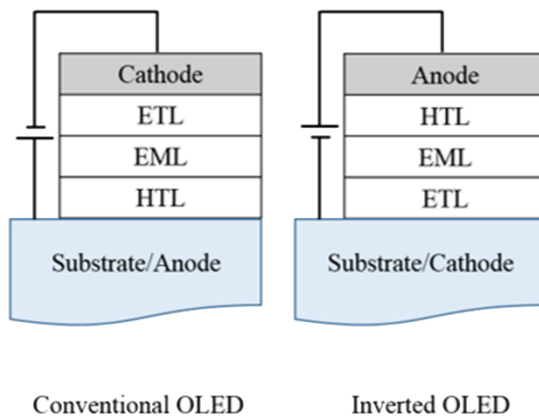
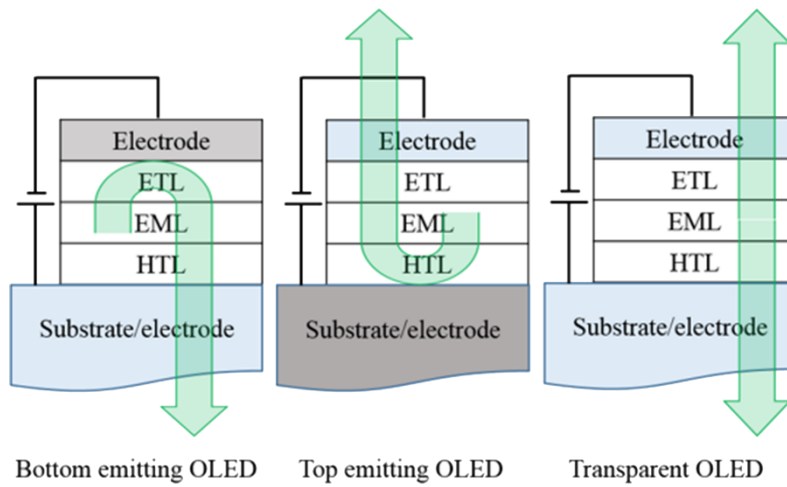


Fig. 1.1 Outlines of the OLEDs.

1.2 Operating principles of OLEDs

1.2.1. Understanding of J - V characteristics in OLEDs

OLEDs emit light by converting electrical energy in the following manner: Under electrical excitation, charges (electron and hole) are injected and transported to EML, followed by forming an exciton via recombination of charges in the EML. Finally, light is generated and emitted to the air. This behavior is reflected in the J - V characteristics of the device shown in **Fig. 1.2**. For an easy explanation, bi-layered organic layers are considered here.

When organic layers are sandwiched between two different electrodes, a built-in potential (V_{bi}) is formed inside the device due to the difference of the work functions between two electrodes as shown in case 1 of **Fig.1.2**. As the external voltage increases, the band diagram of the device also gradually changes, especially in the slope of the energy level of the organic layers. Moreover, the major component of the current is switched at $V = V_{bi}$, resulting in different J - V characteristics. This voltage dependence of the current characteristics can be described as three parts; Ohmic, diffusion dominated, and space charge limited current region. At a low voltage bias near 0 V, the J - V behavior is governed by the Ohmic current, which is actually a parasitical current. The currents are linearly proportional to the external voltage. When it is set up with a voltage lower than V_{bi} , the diffusion current originates from the charge reservoir of the metal electrode and goes to the charge-deficient organic layer that dominantly influences the J - V characteristic of the device,

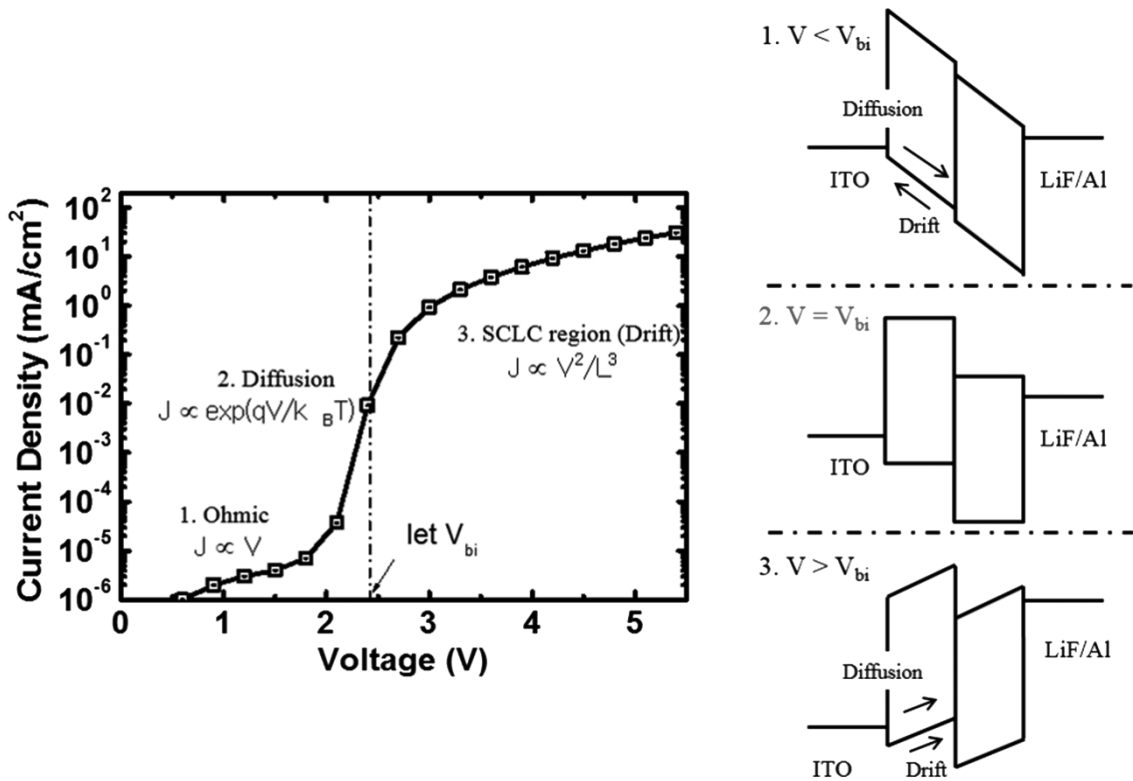


Fig. 1.2 Current density-Voltage (J - V) characteristics of the OLEDs can be distinguished as three parts; Ohmic, diffusion dominated, and space charge limited current region depending on the external voltage bias. The energy level alignment of the device also described here in the case of (1) $V \sim 0V$, (2) $V = V_{bi}$, and (3) $V > V_{bi}$, respectively.

leading to the exponential dependence of the current on the external voltage governed by the Shockley equation.⁹

$$J = J_0 \left[\exp\left(\frac{qV}{\eta kT}\right) - 1 \right], \quad (1)$$

where J_0 denotes the saturation current density, k is the Boltzmann constant, T is the temperature, and q is the unit charge. In addition, in the diffusion dominated regime, the drift current is negligible compared to the diffusion current due to low intrinsic carriers in the organic layers. As the voltage corresponds to V_{bi} , the J - V characteristics are transited from diffusion-dominated current to space charge-limited current, thereby a quadratic dependence of the current on the external voltage can be derived in accordance with the Mott-Gurney square law, given by¹⁰

$$J = \frac{9}{8} \varepsilon_0 \varepsilon_r \mu \frac{V^2}{L^3}, \quad (2)$$

where ε is the permittivity, μ is the mobility of the organic layer, V is the external voltage, and L is the layer thickness.

1.2.2. External quantum efficiency of OLEDs

The External Quantum Efficiency (EQE) of OLEDs is defined as the ratio of the number of emitted photons to the amount of charge injected into device, and can be expressed by the following equation.¹¹

$$\eta_{EQE} = \eta_{int} \times \eta_{out} = \gamma \times \eta_{s/t} \times q \times \eta_{out} \quad (3)$$

Here, γ is the charge balance factor, η_{int} the Internal Quantum Efficiency (IQE), $\eta_{s/t}$ the ratio of singlet to triplet excitons ($\eta_{s/t} = 0.25$ for fluorescent, $\eta_{s/t} = 1$ for phosphorescent emitters), q_{PL} is the photoluminescence (PL) of the quantum yield, and η_{out} is the out-coupling efficiency of the emitted light. Using eq. (3), a maximum EQE has been predicted at 30% for green phosphorescent OLEDs (PhOLEDs).

Recently, however, it has been reported that the orientation of the transition dipole with respect to the substrate greatly influences the EQE of a device with micro-cavity structures.¹²⁻²² In particular, emissions from horizontally-oriented dipoles (parallel to the substrate) contribute more to the out-coupling efficiency of the OLEDs than the emissions from vertically-oriented ones, because most of the emitted light from the vertically-oriented dipoles is propagated through the parallel direction with respect to the substrate as shown in **Fig. 1.3(a) and (b)**. These effects have been demonstrated and confirmed in the polymers as well as the small-molecules-based OLEDs.¹²⁻²² Therefore, the orientation factor must be added to eq. (3) for a more precise calculation.

Recently, Kim *et al.*²³ applied the orientation factors to eq. (3) referred to the previous reports as follows:²³⁻²⁵

$$\eta_{EQE} = \gamma \times \eta_{s/t} \times q_{eff}(\phi_{PL}, \Theta, \Gamma) \times \eta_{out}(\Theta, \Gamma) \quad (4)$$

where q_{eff} is the effective quantum yield, Θ is the orientation factor, and Γ is a geometric factor related to the device's structure. They expanded the boundaries of the EQE from 30% to 46% in the PhOLEDs with the horizontally-oriented emitter, and proposed a new map of the EQE depending on the values of the q_{PL} and Θ as shown in **Fig. 1.3(c)**. Based on the prediction, an EQE of over 40% can be achievable in practice with $q_{PL} = 0.95$ and $\Theta = 0.95$ in the PhOLEDs.²³

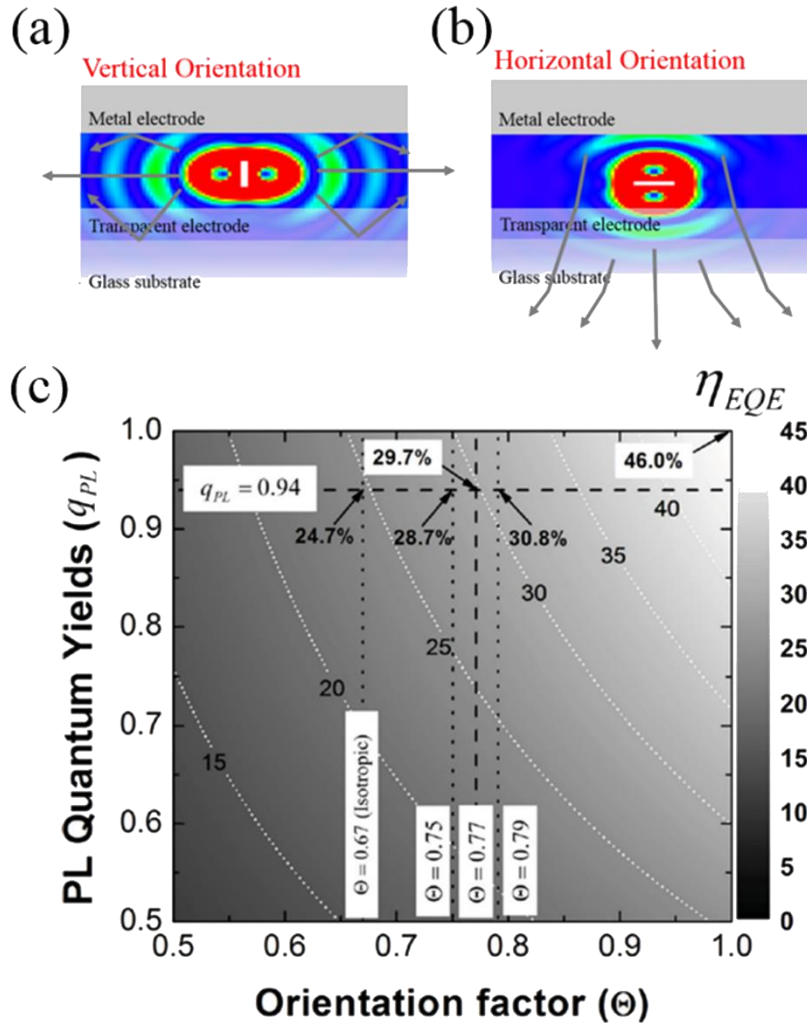


Fig. 1.3 Emission patterns depending on the dipole orientation. (a) A light emitted from the vertically oriented dipoles is guided through the parallel direction with respect to the substrate, and (b) a light from the horizontally oriented dipoles is effectively emitted out to the air. (c) Contour plots as a function of the orientation of the dipoles and their PL quantum efficiency taken from [23].

1.2.3. Energy transfer between host and dopant materials

In PhOLEDs, injected charges are recombined within organic host materials and transferred to an organometallic compound to enable the efficient emission of the phosphorescence. An alternate path is direct emission from the dopant via charge trapping. The former is governed by Förster and/or Dexter mechanisms.^{26, 27} Förster energy transfer denotes the non-radiative energy transfer from an excited donor to an acceptor, resulting from the dipole–dipole interactions between them. This is called “resonant dipole coupling” as shown in **Fig. 1.4(a)**.²⁷ The rate of the Förster energy transfer is a function of the fluorescence lifetime of the host (donor), τ_D , and the effective distance between the host and dopant (acceptor), R_0 , as follows:

$$K_F = \frac{1}{\tau_D} \left(\frac{R_0}{R} \right)^6 \quad (5)$$

The K_F is equal to $1/\tau_D$, the rate of fluorescence of the host at $R = R_0$, and R_0 is defined as

$$R_0^6 = \frac{9000 \ln(10) \kappa^2}{128 \pi^5 n^4 N_a} \int_0^\infty F_D(\tilde{\nu}) \epsilon_A(\tilde{\nu}) \tilde{\nu}^{-4} d\tilde{\nu} \quad (6)$$

Here κ^2 is the dipole angular orientation of each molecule, n is the refractive index, N_a is Avogadro’s number, $\tilde{\nu}$ is the wavenumber, F_D is the normalized PL spectrum of the host, and ϵ_A is the molar extinction coefficient of dopant.

The Förster energy transfer is a long range transfer within 100 \AA . It allows the transition from the singlet of the host to the singlet of the dopant (S–S); from the

singlet of the host to the triplet of the dopant (S–T); or from the triplet of the host to the triplet of the dopant (T–T). For efficient Förster energy transfer, the fluorescence lifetime of the host has to be sufficiently long. In addition, the more spectral overlap between the absorption spectrum of dopant and the emission spectrum of host, the better the energy transfer that takes place. The overlap factor can be expressed as

$$J = \int_0^{\infty} F_D(\lambda)\varepsilon_A(\lambda)\lambda^4 d\lambda \quad (7)$$

where λ is the wavelength.

Dexter energy transfer is defined as the process of electron exchange between the host and the dopant as shown in **Fig. 1.4(b)**.²⁶ It allows the transition from the singlet of the host to the singlet of the dopant (S–S) or from the triplet of the host to the triplet of the dopant (T–T). In addition, the range of the energy transfer is relatively short, within 10 Å, compared to the Förster energy transfer.

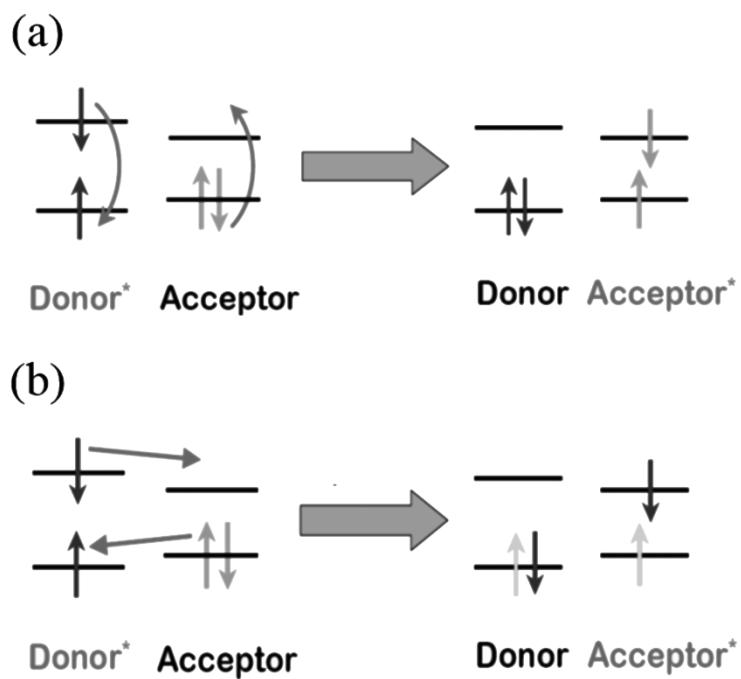


Fig. 1.4 Schematic illustration of (a) Förster and (b) Dexter energy transfer mechanisms, respectively.

1.3 Inverted OLEDs for flexible devices

Flexible OLEDs are one of the most promising technological developments for next generation displays and solid-state lighting devices beyond the current generation of displays and lighting devices such as plasma display panels (PDP), liquid crystal displays (LCD), fluorescent tubes and incandescent bulbs. OLEDs are self-light-emitting devices from thin layers without back light units and eco-friendly light sources without harmful elements. Moreover, a very high contrast ratio of almost infinity in a dark ambient environment is able to be realized using OLEDs due to their zero luminance in the off-state. Therefore, OLEDs are very useful in flexible devices beyond the previous sources. Flexible OLEDs are defined as light sources with stable operation under external deformations such as repetitive bending, folding, rolling, stretching, or twisting. To achieve high performance, the structural concept or design of the devices first has to be understood because the conditions for the fabrication of flexible devices is more complicated and strict than current devices.

Most current devices for lighting or displays are fabricated based on glass substrates due to their good optical characteristics and easy handling; it has high transparency in visible light regions, low water-vapor permeability, high thermal stability, and easy fabrication. However, glass substrates are so brittle that they are not suitable in flexible devices. The alternative candidates are barrier coated plastics, papers, or thin metal foils. Among them, barrier coated plastic substrates are the best choice for flexible substrates due to their flexibility, flat surface morphology, light weight, low price, transparency, and thickness.

When glass substrates are replaced by plastics, the processing temperature for the fabrication of the device has to be reduced significantly due to the way plastic substrates deform when exposed to high temperatures. As a result, oxide thin-film transistors (TFTs) are a promising candidate for the active-matrix (AM) circuit on the plastic substrates out of the various types of TFT, because oxide TFTs not only have a suitable low processing-temperature, but also have superior properties such as high mobility, flexibility, good uniformity, and improved stability compared to conventional amorphous silicon, polycrystalline silicon TFTs, or organic TFTs, as shown in **Fig. 1.5**.²⁸⁻³¹ Moreover, oxide TFTs are appropriate for large-scale, low-cost fabrication due to the capabilities of the solution process with roll-to-roll or spin-casting methods. Another advantage of oxide TFTs is that a simple pixel circuit design can enable large size AMOLEDs because the uniformity of oxide TFTs is maintained in both the long and short range thanks to their amorphous nature. Therefore, the simplest pixel architecture, composed of two TFTs and one capacitor (2T + 1C), is available for practical AMOLED circuits. In the circuit, one TFT is used to store a data voltage to the capacitor during addressing, and the other TFT provides a driving current to the OLED, and this simple 2T + 1C equivalent circuit is suited for AMOLED backplanes.

Oxide TFTs have n-type characteristics with electron mobility greater than $10 \text{ cm}^2 \text{ V}^{-1} \text{ s}^{-1}$, as such, inverted OLEDs (iOLEDs) are preferred over conventional OLEDs in order to gain voltage controlled current sources (VCCS) for the stable operation of the iOLEDs as shown in **Fig. 1.6**.³² If conventional OLEDs are connected to the n-type TFTs (**Fig. 1.6b**), the OLEDs are controlled by the gate voltage of the TFTs, so that the operation of OLEDs is vulnerable to the degradation

of the TFTs. To supply a steady current to the OLEDs independently of the degradation of the TFTs, iOLEDs have to be connected to the drain of the n-type TFTs, instead of conventional OLEDs. Unfortunately, efficiency of an iOLED is not yet as good as that of conventional OLEDs. As a result, the complicated AM circuits such as 4T + 2C, 5T + 1C, 5T + 2C, or 6T + 2C with conventional OLEDs have been utilized instead of the simple 2T + 1C architecture with an iOLED and oxide TFT as shown in **Fig. 1.7**.³³⁻³⁶ If the efficiency of the iOLEDs is improved, a high-performance flexible device can be realized with simplicity and low power consumption.

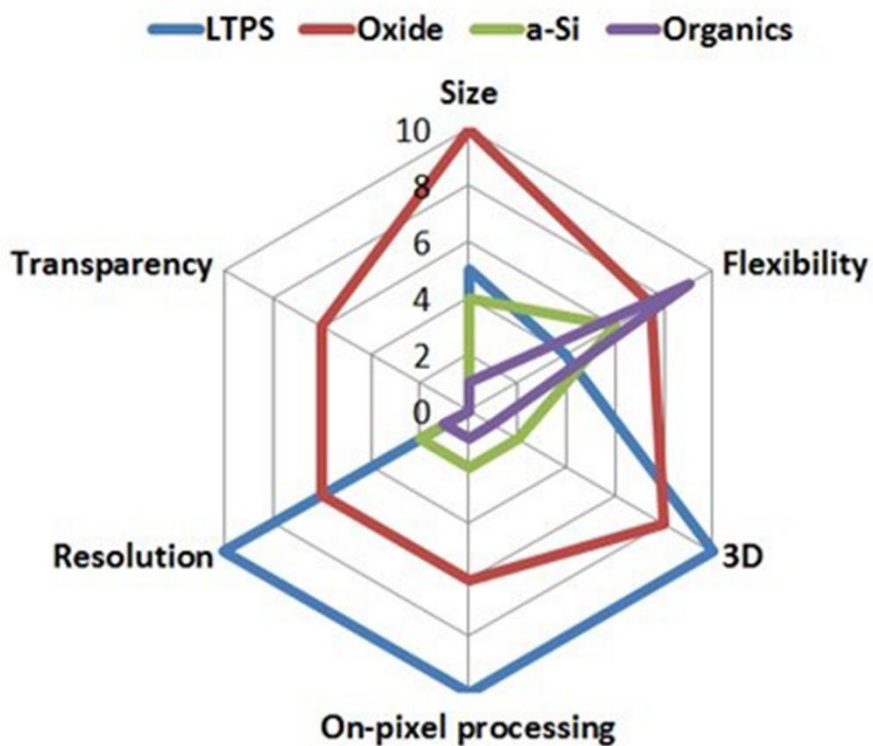


Fig. 1.5 Comparison of the technological suitability among different backplane technology. [Source: IDTechEx, 31]

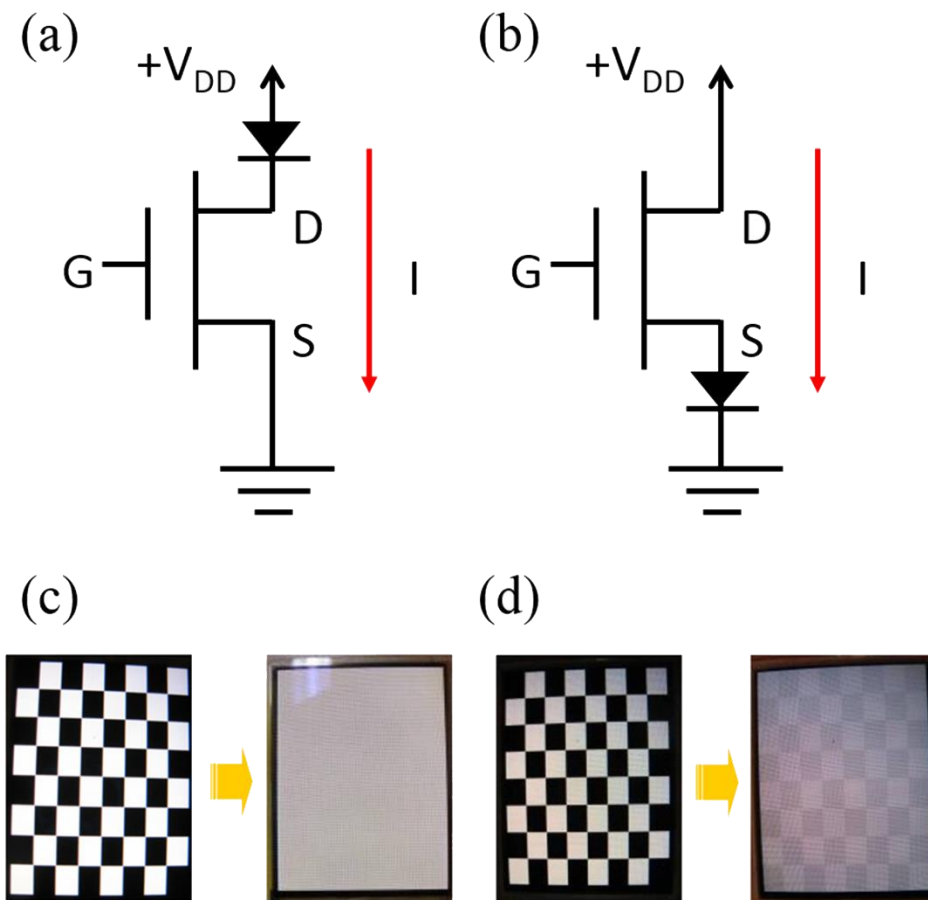


Fig. 1.6 Schematic diagrams of pixel circuit for active matrix OLED (AMOLED). (a) n-type TFT connected with inverted OLED, (b) n-type TFT connected with conventional OLED. (c) Image sticking test using circuit (a), and (d) using circuit (b), respectively. Images taken from [32,33]

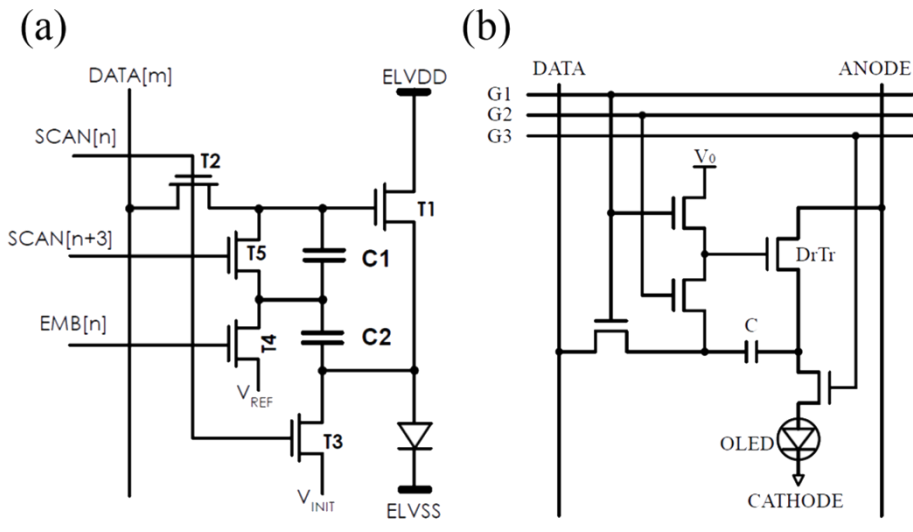


Fig. 1.7 Compensation circuits for AMOLED based on the oxide (IGZO) TFTs with OLEDs from (a) Samsung Display and (b) Sharp and Semiconductor Energy Laboratory (SEL). Images taken from [35,36]

1.4 Issues in inverted OLEDs

The representative materials for the electrode of OLEDs are indium tin oxide (ITO), silver (Ag), or aluminum (Al). These conducting materials are stable, easily form a smooth layer, and have suitable optical properties and high conductivity. The work function (W_F) of the materials are around -4.5 eV, resulting in an energetic mismatch at the interface between the electrodes and ETLs higher than 1.0 eV because the Lowest Unoccupied Molecular Orbital (LUMO) level of the ET materials is located at around -3.0 eV as shown in **Fig. 1.8**.³⁷ Therefore, one of the main challenges in the development of iOLEDs is electron injection (EI) from the bottom cathode to the organic layer due to relatively higher injection barrier height at the interface than that of conventional OLEDs. In addition, a lithium fluoride (LiF) thin layer, which is one of the representative EI layer in conventional OLEDs, is rarely activated in iOLEDs because of the reversed deposition sequence of the electrode/LiF/organic layer, instead of the sequence of organic layer/LiF/electrode as shown in **Fig. 1.9**.³⁸ The poor EI characteristics in iOLEDs causes low external quantum efficiency and low power efficiency, due to the required high driving voltages and loss of charge balance in the device.

The current density–voltage (J - V) characteristics of OLEDs are generally controlled by the charge injection and transported through the electrode/organic or organic/organic junctions, therefore control of the energy level alignment at the junctions, particularly for the bottom electrode/organic junction in the iOLEDs, is important for achieving Ohmic-like contact for high efficiency. To reduce the energy barrier for efficient electron injection and transport at the interface, various methods

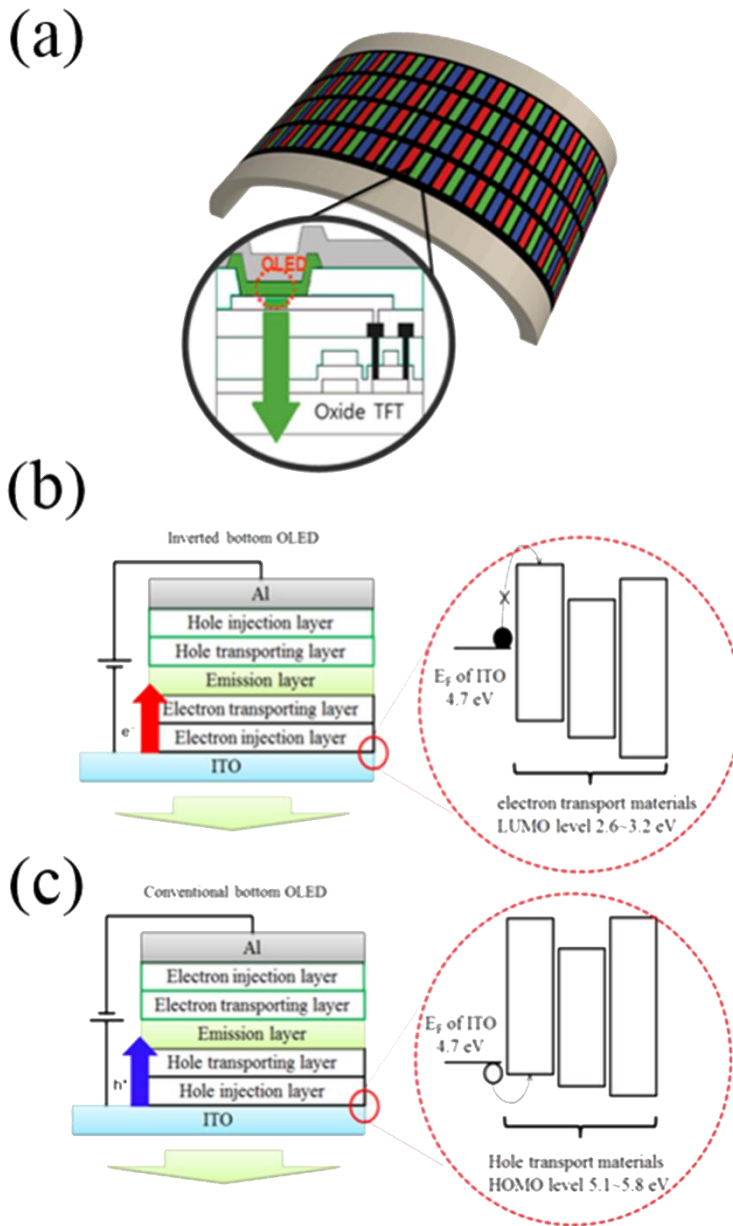


Fig. 1.8 Schematic diagram of (a) pixel of flexible AMOLED, taken from [37] (b) energy diagram of inverted OLEDs, and (c) energy diagram of conventional OLEDs.

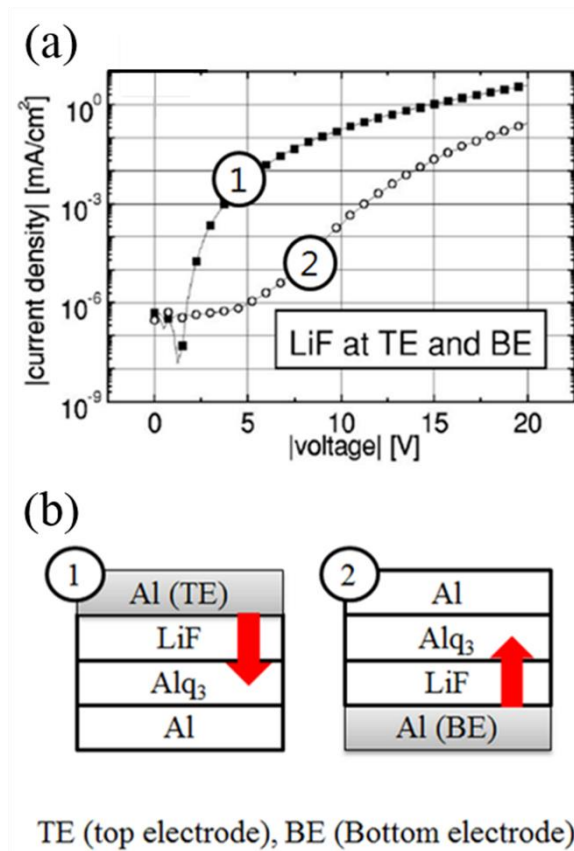


Fig. 1.9 (a) J - V characteristics of electron only device depending on the deposition sequence of LiF layer. Image is taken from [38] (b) The device structures used in (a).

have been introduced and adopted within the iOLEDs. A simple method to achieve Ohmic-like EI contact is to use various combinations of metal and organic material for a low energetic mismatch at the interface. A lot of metals such as Yb, Sm, Ca, and Mg, having low W_F , were adopted for the bottom cathode, but these materials are so unstable that they can cause stability issues.^{39, 40}

An alternative method is to use specific materials that have a low W_F of around 2–2.5 eV such as alkali metals (Li, Cs, Rb, Mg, K, and Na),⁴¹⁻⁴⁴ and metal carbonates (Cs_2CO_3 , Rb_2CO_3) on the stable bottom electrode.⁴⁵⁻⁴⁷ The materials are utilized as thin layer between the organic layer and the electrode, or as a guest inside an organic layer. The method is activated independently of the deposition sequence of the organic layer so that they are widely used in the iOLEDs as the EI layer. Moreover, the metal carbonates can be processed by a solution process.⁴⁸ The thin layer of the n-type dopant between the metal electrode and the organic layer reduces the electron injection barrier by modifying the interfacial potential due to the formation of surface dipoles,⁴⁹⁻⁵¹ leading to an enhancement of the electron injection in the iOLEDs.

Another method is the use of electrical doping in EI layer. Electrical doping in amorphous organic semiconductors (OSs) is one of the important technologies for enhancing charge carrier injection and transport characteristics.⁵²⁻⁵⁵ A fundamental difference of the OSs compared with the crystalline inorganic semiconductors (ISs) is the formation of free carriers in the doped layers. The free charges are generated by ionization in the ISs, but the charge transfer from the dopant to the organic layer and the separation of bounded charges are the main mechanisms in OSs. The doping efficiency of silicon-based ISs is almost 100% due to the low ionization energy.

However, the doping efficiency of the OSs is not as high as that of the ISs, so heavily doped organic layers have commonly been used as charge injection layers.

Electrical doping in OSs enhances the conductivity of the doped organic layer 10^5 times higher than that of the intrinsic layer, resulting in enhanced J - V characteristics, and influences the energy level alignment at the interface between the bottom electrode and the organic layer. Energetically, the electrical doping causes the band bending of the doped organic layers near the electrodes by increasing the carrier density in OSs, and induces a vacuum level shift by forming interfacial dipoles at the same time.⁵²⁻⁵⁷ As a result, electron injection is enhanced via tunneling through the narrow depletion layer at the interface between the bottom electrode and the OS.

Electrical doping has been successfully adopted in state-of-the-art n-i-p OLEDs.⁵⁸⁻⁶³ The operating voltage of n-i-p inverted OLEDs was significantly reduced by enhancing the electrical contact at the bottom electrode/organic interface. However, it might reduce the efficiency of the n-i-p device if the doped layer makes direct contact with the EML due to the exciton quenching effect caused by the bounded charges of the dopants. To solve it, additional intrinsic layers between the doped layer and the EML have been introduced. This resulted in the formation of the organic/organic (O/O) junction, which might influence the electron transport in the iOLEDs because of the energetic mismatch at the doped O/O interface.

The intrinsic organic layer has few charge carriers compared to metal and inorganic semiconductors due to large band gap of about 3 eV, therefore the energy level shifts caused by the interfacial dipole or bending are not pronounced at O/O interfaces, when compared to metal/organic (M/O) interfaces. However, the doped organic layer

considerably influences the electronic structure of the adjacent intrinsic organic layer owing to the large difference of the carrier density at the doped organic/intrinsic organic (DO/IO) junction.⁶⁴⁻⁶⁶ Therefore, control of the interfacial energy level alignment in the DO/IO junction is required to achieve good transport and reduce the operating voltage of the iOLEDs.

1.5 Outline of thesis

This thesis has described what issues exist (**Chapter 1**), how to solve these problems (**Chapter 2 and 3**), how to realize the high efficiency of inverted OLEDs for highly efficient flexible or transparent devices (**Chapter 4 and 5**), and how to reveal the origin of performance improvements in the inverted OLED (**Chapter 5 and 6**).

Requirements for high-quality inverted OLEDs are low driving and turn-on voltage, high EQE, and low efficiency roll-off, and these factors were achieved using the following methods: Management of the charge injection and transport characteristics with doping technology led to a good charge balance of $\gamma \sim 1$. In addition, lowering the energy barrier at the interface of the homo-junction as well as at the interface between the cathode and the n-doped organic layer are required for efficient electron injections into an emitting layer by a proper selection of the electron-transporting materials (**Chapter 2**). An organic p-n junction is one solution for the electron injection layer independent of the work function of the bottom electrode in inverted OLEDs (**Chapter 3**). Use of the exciplex host, TCTA:B3PYMPM, and energy transfer to phosphorescent dye, Ir(ppy)₂(acac), leads to an efficient light harvest, $\eta_{ST} = 1$, and a reduction of the TTA due to the broad distribution of the excitons. In addition, it results in a reduction in the residual charges attributed to Langevin recombination dominance, and the low driving voltage of the device due to the low energy barriers at the interfaces and efficient energy transfer mechanisms in the EML with the exciplex-forming co-host. Based

on the above methods, 29.1% of the max. EQE and 27.8% of the EQE at 10,000 cd m⁻² in conventional OLEDs and 23.6% of the max. EQE and 21.0% of the EQE at 10,000 cd m⁻² in inverted top-emitting OLEDs, were realized (**Chapter 6**). All the devices showed a low turn-on voltage of 2.4 V at 1 cd m⁻². The lower efficiency of the iOLED compared to the conventional OLED is attributed to a low electrical charge balance that can be optimized further, which is currently in progress. In addition, a highly efficient transparent iOLED with a total maximum luminance efficiency of 67 cd/A, and power efficiency of 67 lm/W was realized by using a very efficient organic buffer layer, HATCN (**Chapter 4**). It resulted from the very efficient protection of organic layers from sputtering bombardment by the HATCN layer due to a (001)_{hex} preferred orientation of HATCN molecules on the organic layer (**Chapter 5**).

Chapter 2. A high performance inverted OLED using an electron transporting material with low energy barrier for electron injection

2.1 Introduction

Organic light emitting diodes (OLEDs) have been successfully launched in the market of small size displays and large effort is given to increase the size of the display for TVs, especially for 3-dimensional TVs. Flexible OLEDs and OLED based solid state lighting are also now under active research. Active matrix OLEDs having thin film transistors (TFTs) in each pixel are desired for high-quality full color displays. Oxide TFTs are one of the best candidates for flexible OLEDs among various kinds of TFTs due to their flexibility under repeated bending combined with high carrier mobility, uniformity, and low temperature processing. Since the oxide TFTs are n-type in nature, inverted OLEDs (iOLEDs) with a bottom cathode are preferred to conventional OLEDs with a top cathode. When the conventional OLEDs are connected to n-type transistors, a voltage-controlled current source which is critical to the stability of the device cannot be achieved.³² Therefore, an iOLED connected to the drain end of the n-type TFTs must be used to solve this problem.

The major issue in the inverted bottom emission OLEDs (iBOLEDs) is the electron injection from the transparent bottom cathode to an electron transporting layer, because there is a limited choice of materials for the cathode. Transparent electrodes of indium tin oxide (ITO) and indium zinc oxide (IZO) or thin Al and Ag

electrodes have high work functions (> 4.3 eV) resulting in large energy barriers for the electron injection in the inverted structures. Various methods have been proposed to enhance the electron injection for the device.^{58,62,63,67-70} For example, Chen *et al.*⁶⁷ inserted an ultra-thin Mg layer onto ITO, but it is rather difficult to control the thin layer and the Mg can reduce the transparency. N-doping in electron transporting materials (ETMs) has also been successfully applied to get good electron injection from ITO to an electron transporting layer (ETL).^{58,62,63,68} Nevertheless, the external quantum efficiencies (EQEs) of the iBOLEDs were limited to below 15%. Most of the previous works focused mainly on the interface between the electrode and an organic layer,^{2,68-76} although other interfaces are also important in the inverted device structure.⁷⁷

In this chapter, it was demonstrated, based on the energy levels and the current density-voltage (J - V) characteristics of electron only devices, that the interface between an n-doped ETL (n-ETL) and an ETL is as important as the interface between the cathode and the n-ETL for efficient electron injection to an emitting layer. By properly selecting an ETM to have no energy barrier for electron injection between the n-ETL and the ETL, a high performance iBOLED with the maximum EQE of 20% and the maximum power efficiency of 80 lm/W was realized.

2.2 Experimental

The inverted bottom emission OLEDs have the structure of ITO/n-doped ETL (20 nm)/undoped ETL (30 nm)/8 wt. % Ir(ppy)₃ doped 4,4'-N,N'-dicarbazole-biphenyl (CBP) (15 nm)/undoped 1,1'-bis-(4-bis(4-methyl-phenyl)-amino-phenyl)-cyclohexane (TAPC) (30 nm)/8 wt. % ReO₃ doped TAPC (20 nm)/Al. The organic layers and the metal anode were successively deposited on pre-cleaned 150 nm-thick-indium tin oxide (ITO) patterned glass substrates. Three different ETMs of bis-4,6-(3,5-di-3-pyridylphenyl)-2-methylpyrimidine (B3PYMPM), 4,7-diphenyl-1,10-phenanthroline (Bphen), and 2,2',2''-(1,3,5-benzenetriyl)tris-[1-phenyl-1H-benzimidazole] (TPBi) were selected to investigate their effects on the performance of the inverted OLEDs depending on the different lowest unoccupied molecular orbital (LUMO) levels of the ETMs as shown in Fig. 2.1. Rb₂CO₃ was used as the n-dopant in the n-doped ETLs with a doping concentration of 15% for all the devices.^{47,50} ReO₃ was used as the p-dopant in the devices.^{53,78,79} The current density-voltage-luminance (*J-V-L*) characteristics of the devices were measured using a Keithley 237 semiconductor parameter analyser and a Photo Research spectrophotometer (PR-650).

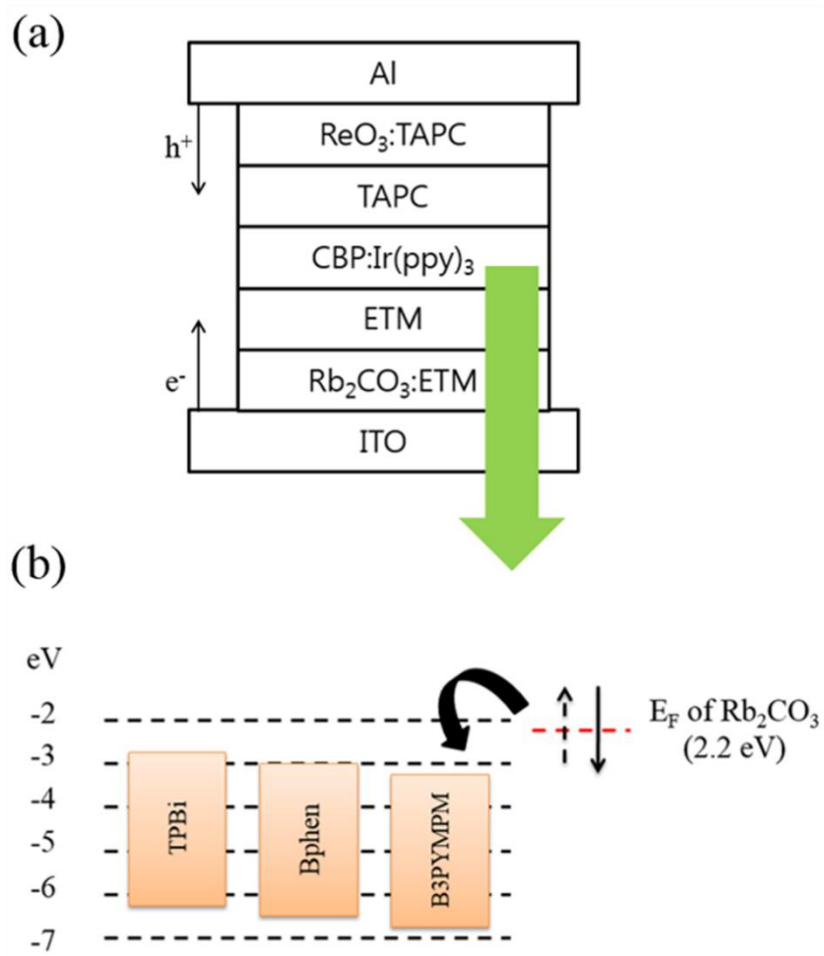


Fig 2.1 (a) The device structure of the iOLEDs with three different ETMs. (b) HOMO and LUMO levels of the ETMs and illustration of n-doping via charge transfer from the LUMO level of Rb_2CO_3 to the ETMs.

2.3 Result and Discussion

Figure 2.2 shows the J - V - L characteristics of the inverted OLEDs. Among the three ETMs, B3PYMPM resulted in the lowest charge injection and turn-on voltages of 1.9 V and 2.4 V, respectively. The injection voltage was defined as the voltage where the charge injection begins to rise, and the turn-on voltage was defined as the voltage where the luminance of 1 cd/m². The driving voltage at 1,000 cd/m² is only 4.3 V for the device with the B3PYMPM ETL followed by 5.4 V for the Bphen ETL and 7.4 V for TPBi ETL. These facts indicate that electrons are more easily injected and transported from the bottom cathode to the light emitting layer in the B3PYMPM device than the others because the hole injection layer and the hole transport layer are the same in the three devices. It is interesting to note that the difference between the injection voltage and the turn-on voltage is very small (0.5 V) for the B3PYMPM device but it is large, *i.e.* about 1.5 V, for the other devices, indicating a more balanced injection of electrons and holes in the B3PYMPM device than the other devices.

The electron injection and transport characteristics of the devices were interpreted using two different electron only devices: (1) ITO/n-ETL (50 nm)/Al; and (2) ITO/n-ETL (20 nm)/undoped ETL (30 nm)/Al. The three different ETMs were used as the ETLs and the doping concentration was 15% in all the devices. Negative bias was applied on the ITO electrode for the electron injection from ITO to the ETLs. Figure 2.3 shows the device structures of the electron only devices and the J - V characteristics of the devices. It is very interesting to note that the J - V

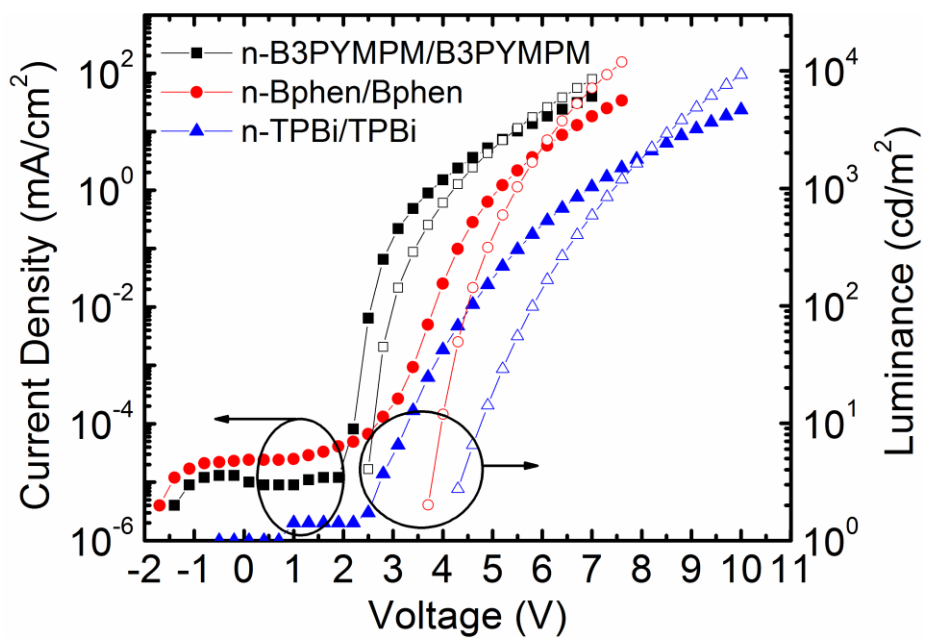


Fig. 2.2 The J - V - L characteristics of the iOLEDs with three different ETMs, B3PYMPM (square), Bphen (circle), and TPBi (triangle), respectively. In addition, closed symbols represent the J - V curves and open symbols denote the L - V curves, respectively.

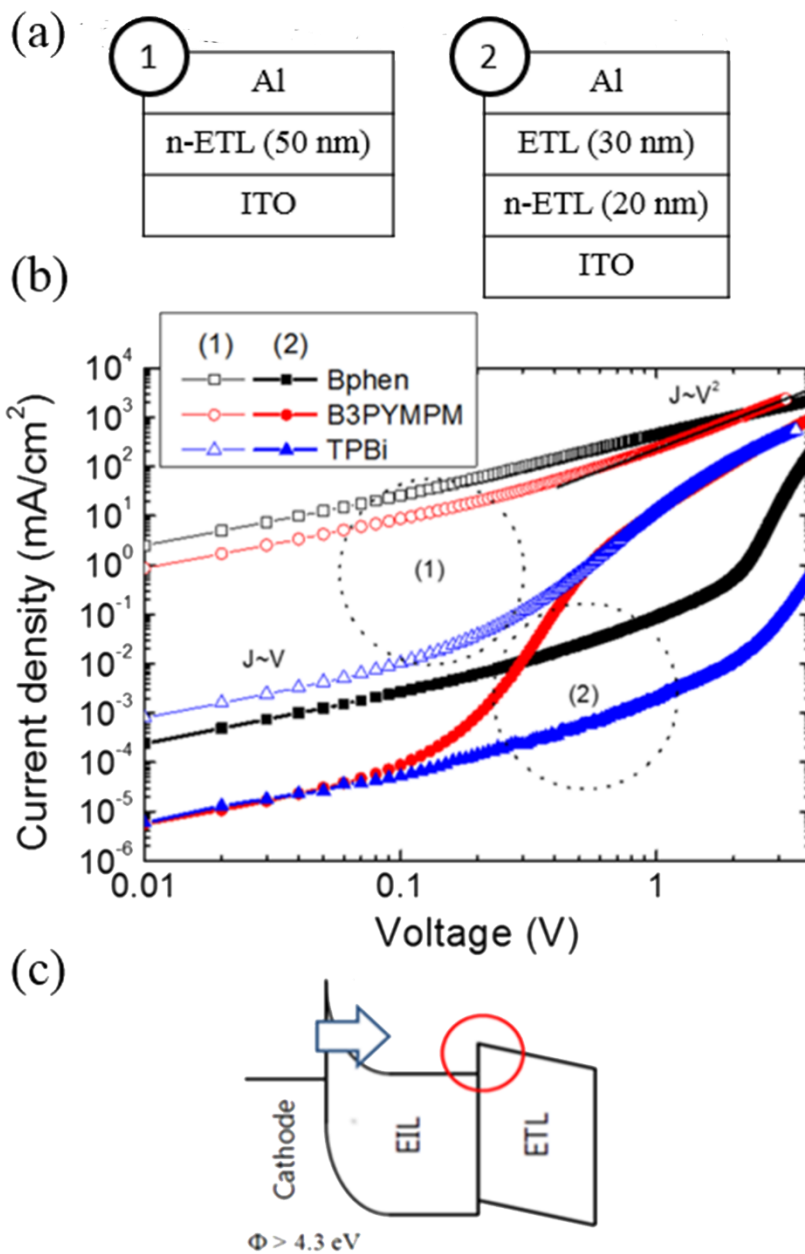


Fig. 2.3 (a) The device structures of two different electron only devices. (b) the J-V characteristics of the electron only devices with Bphen (square), B3PYMPM (circle), and TPBi (triangle). Closed symbols are for the type 1 and open symbols denote for the type 2 of the electron only devices, respectively. (c) It can be inferred that the results of (b) are attributed to the energy barrier between the n-ETL/ETL junctions.

characteristics of the electron only devices with the structure (1) are not consistent with the J - V characteristics of the iBOLEDs. In the type 1 of the electron only devices, the BPhen device shows the highest current among the three devices followed by the B3PYMPM and the TPBi devices. In addition, the device with the Bphen layer show an Ohmic current up to the current density of 10^3 mA/cm² and show the highest current-density among the three devices. However, the other devices with the B3PYMPM and TPBi layer show the transition from Ohmic to space charge limited current (SCLC) or from Ohmic to trap limited current (TCLC) followed by SCLC region, respectively. It is resulted from the different injection from ITO electrode and transport behaviours in the n-doped layers having different carrier density and mobility. In the OLEDs, however, the B3PYMPM device showed the higher current and luminance in the low voltage region than the BPhen device.

The difference can be understood using the electron only devices with the structure (b). Insertion of the intrinsic ETL between the n-ETL and the Al electrode in the electron only devices modified the J - V characteristics significantly as shown in Fig. 2.3(b). It lowers the current density by orders of magnitude in low voltage (Ohmic current) region. Also, all the J - V curves showed a transition from the Ohmic current where J is linearly proportional to applied voltage to the TCLC. Interestingly enough, the B3PYMPM layer exhibited the transition at a much lower voltage than the other two materials. The current density in the B3PYMPM based electron only device dramatically increases as the voltage increases over 0.1 V. This fact suggests that the barrier height for electron injection from the n-B3PYMPM layer to the undoped B3PYMPM layer is lower than for other materials as shown in Fig 2.3(c).

The injection characteristics and the energy band alignment at the interfaces of the devices were further investigated by ultraviolet photoelectron spectroscopy (UPS). UPS measurements were carried out with He I (21.2 eV) and He II (40.8 eV) as excitation sources at a base pressure at 10^{-10} Torr. The detailed experimental procedures were described in the previous reports.^{46,80} Fig. 2.4(a) to Fig. 2.4(b) illustrate the evolutions of UPS spectra near (1) the onset and (2) the valence band region during junction formation between undoped ETLs and n-doped ETLs. All binding energies are referenced to the Fermi level (E_F) of ITO. The vacuum level (VL) shift and HOMO level position can be analysed with increment of thickness of organic material from the figures, and they are indicated with vertical lines, respectively. In the B3PYMPM system as shown in Fig. 2.4 (a), when pristine B3PYMPM is deposited on n-doped B3PYMPM, there is no obvious change in onset spectra. This indicates that there is no interface dipole between n-doped B3PYMPM and pristine B3PYMPM. From valence band spectra shown in Fig. 2.4(b), Features in the valence band of n-B3PYMPM retain the same binding energy when the undoped films are formed. From the magnification of HOMO states as shown in the right hand side of Fig. 2.4(b), a nearly identical position of binding energy for HOMO states in both doped and undoped films is identified. The position of HOMO is determined by interpolating the shoulder of HOMO signal and background of spectra. As a result, there is little injection barrier between n-B3PYMPM and pure B3PYMPM since their HOMO states show good alignment. However when it comes to the cases of BPhen or TPBi, observable changes in UPS spectra are identified. Fig. 2.4(b) and Fig. 2.4(c) represent the evolutions of the valence bands and vacuum level in BPhen and TPBi films, respectively. According

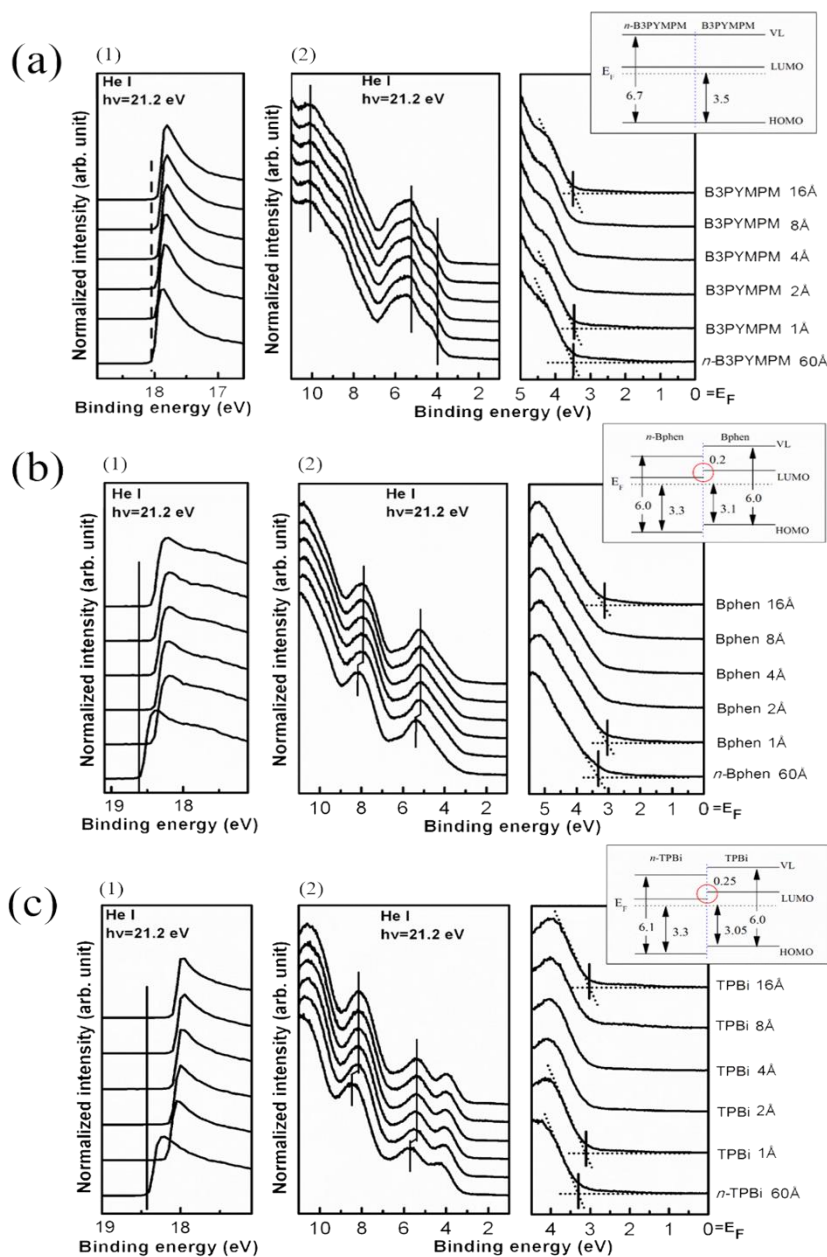


Fig. 2.4 Developments of UPS spectra near (1) the onset and (2) the valence band region of (a) ITO/n-B3PYMPM/B3PYMPM, (b) ITO/n-Bphen/Bphen, and (c) ITO/n-TPBi/TPBi structures, respectively. The inset shows the resulting energy level alignment, and all binding energies are referenced to the Fermi level (E_F) of ITO. The vacuum level (VL) shift and HOMO level position can be analysed with increment of thickness of organic material, and they are indicated with vertical lines, respectively. The valence band regions are focused to analyse the behaviour of energy level movements in detail.

to these two figures, shifts in vacuum level and valence band can be addressed. Upon deposition of pristine BPhen on n-doped BPhen, there are shifts in vacuum level toward the lower binding energy as shown in (1) of Fig. 2.4(b). This indicates that an interface dipole is formed between n-doped BPhen and pristine BPhen layers. Valence band features also show the same shifts as Figure in the right hand side of Fig. (2) of 2.4(b), demonstrates the shift in HOMO states when pristine BPhen is deposited on n-doped BPhen, and it indicates a 0.2 eV shift toward the lower binding energy. Following the same route a 0.25 eV shift can be found between n-doped TPBi and pristine TPBi as shown in Fig. 2.4(c).

Based on the results, the energy band diagrams of the ITO/n-ETL/ETL structure were constructed for the three different systems to demonstrate the electron injection barrier between n-ETL and ETL more clearly as shown in the insets in the Fig. 2.4(a) to Fig. 2.4(c). LUMO energy levels were included, and the values were calculated from the HOMO level and the lowest energy absorption edge of the UV-Vis absorption spectrum determining optical band gap of the material. Since optical band gap of doped organic film is as similar as that of pristine film,⁸¹ the complete energy band diagrams were constructed in both n-doped ETL and undoped ETL regions using the optical band gap of 3.6 eV for B3PYMPM,³ of 3.4 eV for Bphen,⁸² and of 3.5 eV for TPBi.⁸³ As a result, carrier injection barriers between n-ETLs and ETLs are found to be different in these three ETMs. B3PYMPM system shows negligible barrier, while the injection barrier observed in BPhen system is 0.2 eV, and the barrier in TPBi system is 0.25 eV. These results are consistent with the *J-V* characteristics of iBOLEDs and electron only devices in which the lowest injection and turn on

voltage (Fig. 2.2) and the lowest transition voltage (Fig. 2.3) were observed in the devices using B3PYMPM as ETLs.

The energy barrier between n-ETL and ETL is an important factor for the performance of inverted OLEDs as shown in Fig. 2.5. The B3PYMPM based device exhibited the maximum EQE of 19.8% (at 45 cd/m²) which is the highest efficiency reported up to now in the iBOLEDs to the best of our knowledge. It is more than a 30% increase from the previous best efficiency of 15%.⁷⁶ The maximum power efficiency (η_{power}) of the device with the B3PYMPM ETL is very high with the value of 79.8 lm/W, and it is 1.8 times higher than that of 42.7 lm/W for TPBi ETL and 37.3 lm/W for Bphen ETL as summarized in Table 1. However, the η_{power} of the device with the B3PYMPM rapidly decreases after 100 cd/m², and finally reached 33.3 lm/W at 1,000 cd/m². It is just 1.2 times higher than that of 27.2 lm/W for the device with Bphen ETL, indicating that roll off in the device with B3PYMPM is much larger than the other devices due to the formation of an exciplex. To elucidate the formation of an exciplex, the electroluminescence (EL) spectra of the three iOLEDs were additionally investigated as shown in Fig. 2.6. The extra peaks of EL spectra were only observed in the device with B3PYMPM at the region around 430 nm as luminance increases. There were no extra peak in the other iOLEDs with Bphen or TPBi except the emission from the Ir-dopant.

The origin of the peaks in the device with B3PYMPM was from the exciplex formation at the interface between B3PYMPM and CBP layer. The energy level difference between LUMO level of B3PYMPM and HOMO level of CBP is 2.9 eV, and this value accurately corresponds to extra peak depicted in figure Fig. 2.6. The

efficiency roll-off related to the formation of the exciplex in the PhOLEDs was further investigated based on the energy transfer process from the exciplex to the phosphorescent dopant. Based on analysis of the low temperature photoluminescence (PL) spectrum of CBP:B3PYMPM co-deposited film, the energy level of the exciplex was inferred and the energy level diagram of the triplet excited state (T_1) and singlet excited state (S_1) with respect to ground state at the interface of the EML/ETL in the OLEDs was obtained as shown in Fig. 2.7.⁸⁴ It indicates that the triplet excitons in the exciplex is transferred to the CBP via energy transfer process followed by an energy transfer to the Ir(ppy)₃, because the T_1 level of the CBP is smaller than the energy gap of the triplet exciplex. However, at high luminance region, all the excitons of the exciplex is not fully transferred to the dopant, leading to the emission from the exciplex. The emission from the exciplex causes the significant efficiency roll-off in the device, because the PL efficiency of the exciplex is just 0.11 which is approximately 9 times lower than that of the Ir-dopant.

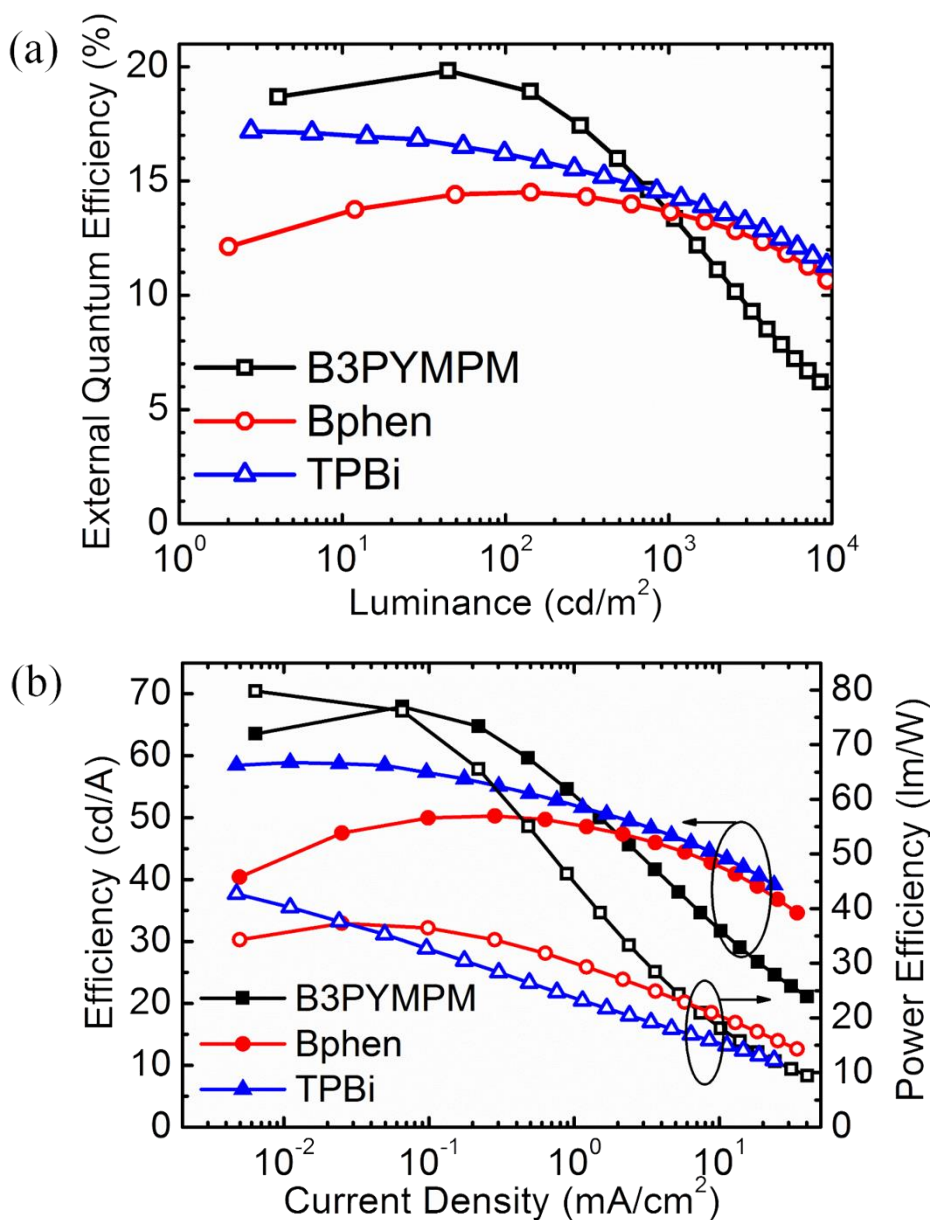


Fig. 2.5 (a) EQE vs. Luminance, and (b) the current and power efficiency vs. current density of the three different iOLEDs with B3PYMPM (square), Bphen (circle), and TPBi (triangle). In Fig. 2.5(b), closed symbols represent the current efficiency and open symbols are depicted the power efficiency, respectively.

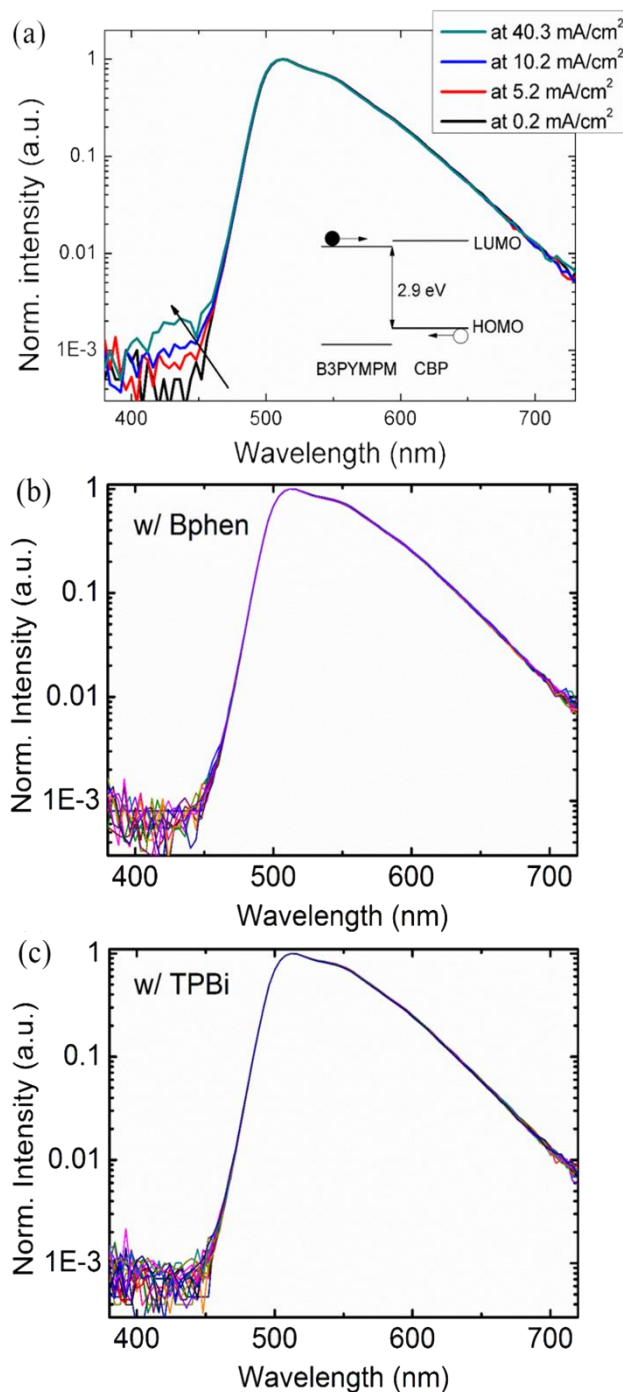


Fig. 2.6 Semi-log plots of EL spectra of the iBOLEDs with (a) B3PYMPM, (b) Bphen, and (c) TPBi, respectively, depending on the applied current density. The extra emission near 430 nm was only observed in (a), and the emission was originated from the exciplex formed between B3PYMPM/CBP interfaces.

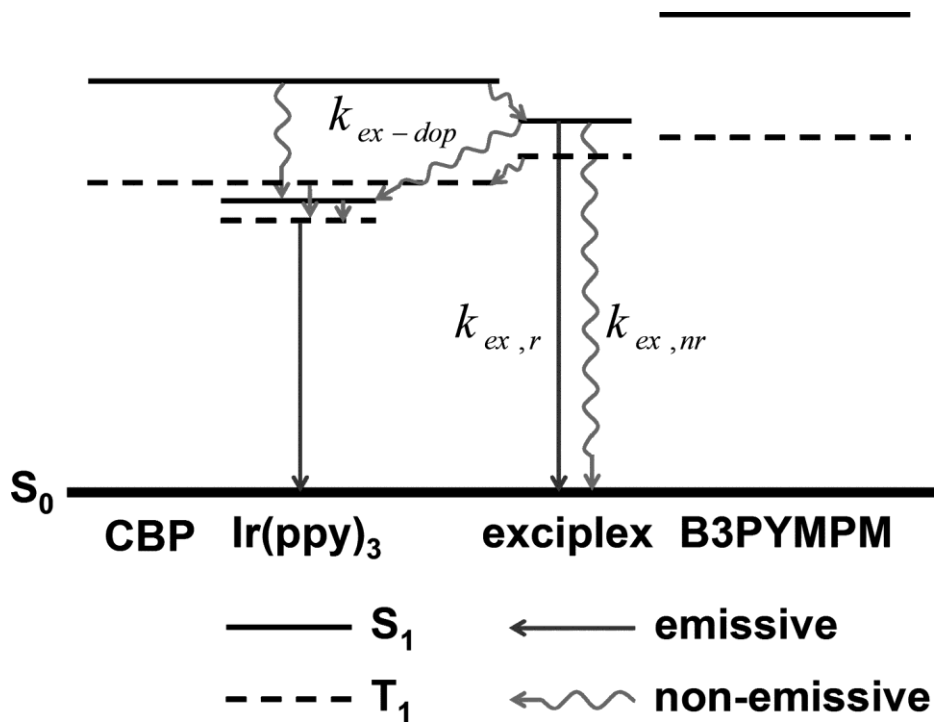


Fig. 2.7 The energy level diagram of the CBP, Ir(ppy)₃, B3PYMPM, and exciplex formed by CBP and B3PYMPM, respectively. The energy level of the exciplex was obtained from the PL measurement at low temperature. The radiative and non-radiative decays are additionally illustrated based on the energy transfer mechanism, and the figure is taken from [27].

Table 1. Characteristics of inverted OLEDs with three different electron transporting materials (ETMs).

ETM	$V_{\text{Injection}}^{\text{a)}}$	$V_{1\text{cd/m}^2}^{\text{b)}$	EQE (%)			η_{power} (lm/W)	
			Max.	@ 100 cd/m ²	@ 1,000 cd/m ²	Max.	@ 1,000 cd/m ²
B3PYMPM	1.9 V	2.4 V	19.8	19.2	13.5	79.8	33.3
Bphen	2.2 V	3.6 V	14.2	14.5	13.6	37.3	27.2
TPBi	2.4 V	4.0 V	17.1	16.1	14.3	42.7	21.2

a) $V_{\text{injection}}$ (injection voltage) defined as the voltage where the charge injection begins to rise.

b) $V_{1\text{cd/m}^2}$ (turn-on voltage) defined as the voltage where the luminance of 1 cd/m².

2.4 Conclusion

In summary, a high performance inverted OLED was realized and investigated the effect of the n-ETL/ETL interface on the performance of inverted OLEDs. Among the three ETMs, B3PYMPM resulted in the lowest injection and turn-on voltages of 1.9 V, and 2.4 V, respectively, and the highest maximum EQE of 19.8% at low voltage. UPS measurements showed that there is no energy barrier for electron injection between n-B3PYMPM and B3PYMPM, while Bphen and TPBi have energy barriers of 0.2 eV and 0.25 eV, respectively. As a result, the electron only device exhibited a large increase in current at a much lower voltage than the other two materials. The energy barrier between n-ETL and ETL is one of the most important factors for high performance inverted OLEDs.

Chapter 3. An organic p-n junction as an efficient and cathode independent electron injection layer for flexible inverted OLEDs

3.1 Introduction

Recently OLEDs have been successfully launched in small sized mobile displays, and a large effort has been made to develop larger sized and flexible OLEDs. Flexible OLEDs on plastic substrates require flexible driving circuits fabricated at low temperature. Oxide TFTs are considered as a candidate for this purpose because the materials satisfy the requirements along with high electron mobility. Moreover, the transistors can be fabricated using a solution process. Since the transition metal oxides are n-type semiconductors, inverted OLEDs are preferred to conventional OLEDs to utilize the oxide TFTs in active matrix OLEDs. The salient feature of inverted OLEDs compared with conventional OLEDs is the electron injection from the bottom electrode to an ETL. Most commonly used transparent electrodes such as ITO and indium IZO or thin aluminum (Al) and silver (Ag) have work functions larger than 4.3 eV, while the lowest unoccupied molecular orbital (LUMO) level of organic materials used for the ETL is in the region of 2.8 – 3.3 eV,⁸⁵ resulting in a large electron injection barrier from the electrode to the ETL. Moreover, solution processible electrodes such as graphene and poly(3,4-ethylenedioxythiophene):poly(styrenesulfonate) (PEDOT:PSS) have been proposed as transparent electrodes for displays and solar cells. It would be very valuable to

develop an electron injection layer operating efficiently independent of the work function of the cathode.

Many kinds of methods have been developed to enhance the charge injection at the metal/organic or organic/organic junctions.^{37,43,46,50,52,54,66,68,78,86-92} One of them is to use n-doping in ETLs using alkali metals or alkali metal carbonates as the dopants.^{37,43,46,50,52,54,78,90-92} When organic materials are doped with the dopants, the Fermi level is modified by increasing the free carrier density in the doped layer. As a result, electrons can be easily injected from the electrode to the doped organic layer over the lowered injection barrier. Another method is the modification of the work function of the electrodes using various kinds of metals or with various surface treatments on the metal substrates.^{4,93-95} In the previous report, Leem *et al.* reported that the charge carrier injection dominantly depends on the work function of the electrode even in doped film,⁹⁶ and another group also reported similar results.⁹⁷ It means that the bottom electrode in inverted OLED still acts as a bottleneck compared with conventional OLED. Recently, PEDOT:PSS, graphene, or halogen treatments lowering the work function of ITO more than 6.0 eV have been adopted in conventional OLED to enhance the hole injection from bottom anode to organic layer.⁴ Unfortunately, it would be useless in inverted OLEDs with bottom cathode.

In this chapter, an organic p-n junction is adopted as an efficient and cathode independent electron injection layer (EIL) for iBOLEDs. Organic p-n junctions are known to generate electrons and holes under reverse bias by tunneling of electrons from the HOMO level of the p-layer to the LUMO level of the n-layer through a narrow depletion layer at the junctions. Forward bias in the OLEDs to inject

electrons and holes into the device corresponds to the reverse bias in the p-n junction to generate electrons and holes at the junction.

The generated holes and electrons at the junction move toward the ITO and undoped ETL layer, respectively. Now the injection barrier for holes (ITO/p-HTL junction) and electrons (n-ETL/ETL junction) can be much lower than that for the direct injection of electrons from ITO to the n-ETL, resulting in an efficient injection of electrons. An overpotential to generate electrons and holes was minimized by using a p-doped copper phthalocyanine (CuPc)/n-doped Bphen layer as the charge generation layer, and this was the first successful application of an organic p-n junction as an EIL for organic electronics to the best of our knowledge. Furthermore, the electron injection characteristics of the p-n junction are independent of the work function of the electrodes.

3.2 Experimental

The iBOLEDs have the pn-i-p structure (device A) of ITO (cathode)/5 mol% ReO_3 doped CuPc (15 nm)/ 15 wt. % Rb_2CO_3 doped Bphen (15 nm)/undoped Bphen (20 nm)/1 wt. % 10-(2-benzothiazolyl)-1,1,7,7-tetramethyl-2,3,6,7-tetrahydro-1H,5H,11H-[1] benzopyrano [6,7,8-ij] quinolizin-11-one (C545T) doped 4,4'-N,N'-dicarbazole-biphenyl (CBP) (20 nm)/undoped TAPC (30 nm)/8 wt. % ReO_3 doped TAPC (20 nm)/Al. For direct comparison, the n-i-p structure (device B) of ITO (cathode)/15 wt. % Rb_2CO_3 doped Bphen (30 nm)/undoped Bphen (20 nm)/1 wt. % C545T doped CBP (20 nm)/undoped TAPC (30 nm)/8 wt. % ReO_3 doped TAPC (20 nm)/Al was also fabricated. Such high doping concentrations were selected because of low doping efficiency of n- and p-dopants in organic semiconductors.^{37,47,54,78} The organic layers and the metal anode were successively deposited using a shadow mask to define an active area of 4.0 mm^2 on a pre-cleaned 150 nm-thick-ITO patterned glass substrates at a base pressure of 10^{-7} Torr. Both UV- O_3 treated and PEDOT:PSS spin coated on ITO glass were used to modify the work function of the electrode. Rb_2CO_3 was used as the n-dopant, and ReO_3 was used as the p-dopant in the devices.^{37,47,50,53,78} The current density-voltage-luminance (J - V - L) characteristics of the devices were measured using a Keithley 237 semiconductor parameter analyzer and a Photo Research spectrophotometer (PR-650). All the devices were encapsulated in a dry nitrogen filled glove box prior to the measurement.

3.3 Result and Discussion

The electrical property of the organic p-n junction was investigated before inverted OLEDs were fabricated since the organic p-n junction should generate charge carriers with minimal extra voltage at the junction under reverse bias to apply it as an efficient EIL in inverted OLEDs, as shown in Fig. 3.1. Organic p-n junctions with two different hole transporting materials (HTMs) were fabricated and their *J-V* characteristics were measured, as shown in Fig. 3.2(a). The structure of the organic p-n junction was ITO/p-doped HTM/n-Bphen/Al. Two different HTMs of CuPc and *N,N,N',N'*-tetrakis(4-methoxyphenyl)-benzidine (MeO-TPD), possessing similar HOMO levels of 5.2 eV and 5.1 eV, but different hole conductivities, were selected to investigate the charge generation efficiency of the organic p-n junctions.^{52,98}

The device with the p-CuPc shows a 10^3 – 10^6 orders of magnitude higher current density than the device with p-MeO-TPD at a given voltage, and symmetric *J-V* characteristics under forward and reverse biases. In particular, more than 100 mA/cm² of current density flow in the device at just 0.3 V for both forward and reverse biases. Since the HOMO levels of the CuPc and MeO-TPD are almost same, the difference must be related to the charge transport in organic films. The conductivity of the doped CuPc is 10^2 orders of magnitude higher than that of the doped MeO-TPD.⁵² As a result, the generated charge carriers are easily transported in the CuPc based device with little voltage drop.

The electron injection ability of the organic p-n junction of p-CuPc/n-Bphen is compared with an n-doped Bphen using the ITO (cathode)/n-doped Bphen/Al device, which is widely used as an efficient EIL in the n-i-p OLEDs. As shown in

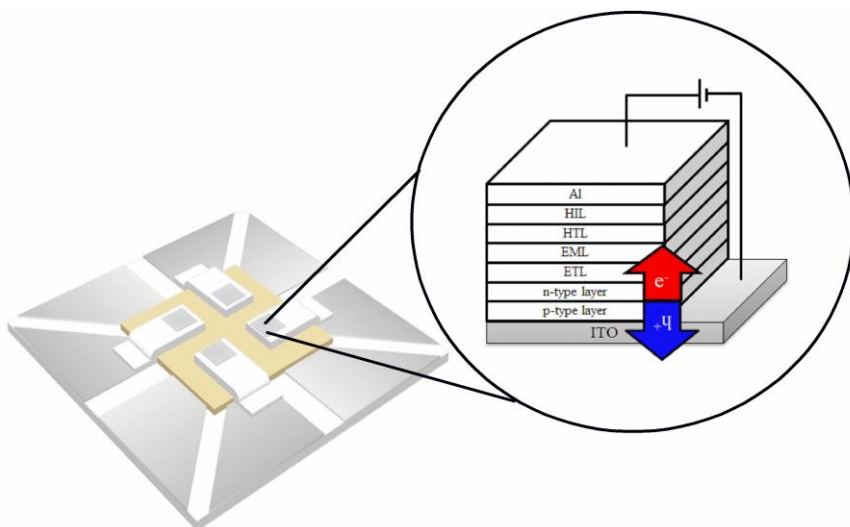


Fig. 3.1 Illustration of an inverted OLED device with a p-n junction as an electron injection layer (EIL). The organic p-n junction acts as an EIL by generating an electron hole pair at the junction under reverse bias with negligible voltage loss to perform as an efficient EIL.

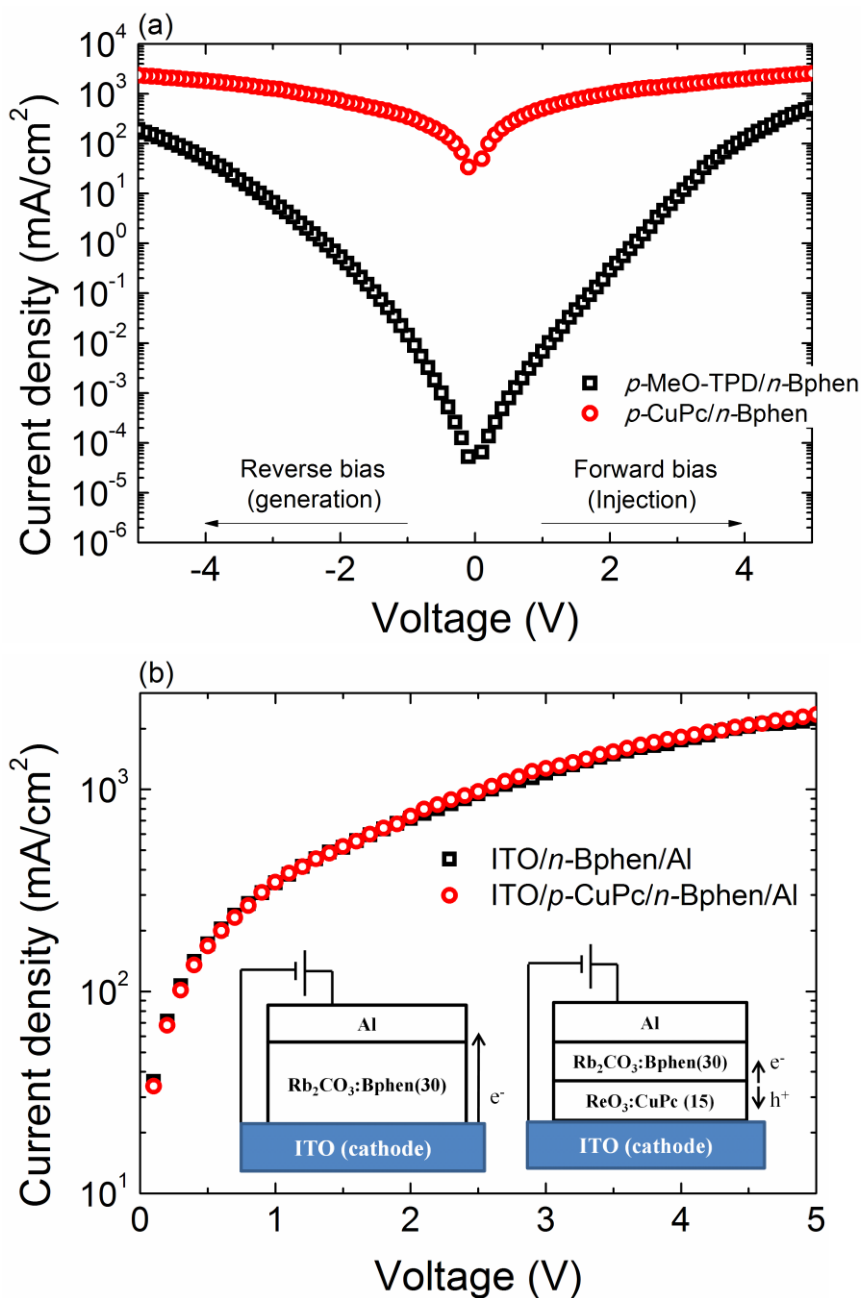


Fig. 3.2 (a) The current density–voltage (J – V) characteristics of two different devices with organic p-n junctions of ITO/ $p\text{-MeO-TPD}$ (15 nm)/ $n\text{-Bphen}$ (30 nm)/Al and ITO/ $p\text{-CuPc}$ (15 nm)/ $n\text{-Bphen}$ (30 nm)/Al, respectively. (b) Comparison of the J – V characteristics of the ITO/ $n\text{-Bphen}$ (30 nm)/Al device and ITO/ $p\text{-CuPc}$ (15 nm)/ $n\text{-Bphen}$ (30 nm)/Al device under negative bias on the ITO electrode.

Fig. 3.2(b), the current density of the device with the p-n junction is almost the same as that of the device with n-Bphen, demonstrating the efficient electron injection ability of the p-n junction.

Figure 3.3 shows the J - V - L characteristics and the efficiencies of the two different iBOLEDs, devices A and B. The electrical and luminous characteristics of the two iBOLEDs are almost the same. The charge injection and turn-on voltages are 2.4 V and 3.1 V, respectively, and the driving voltage at 1,000 cd/m² is 5.1 V for both devices. The injection voltage (V_{inject}) is defined as the voltage where the charge injection begins to rise, and the turn-on voltage ($V_{turn-on}$) as the voltage at the luminance of 1 cd/m². The current and luminous efficiency of device A are also comparable to those of device B. The maximum values of the current and luminous efficiency are 14.7 cd/A, and 10.3 lm/W for device A, respectively, compared to 15.0 cd/A, and 10.5 lm/W for device B, respectively, as shown in Fig. 3.3(b).

A notable feature of device A is that the organic p-n junction can inject and supply electrons to an emission layer efficiently, independently of the work function of the bottom cathode. Electrons are usually injected over the injection barrier by thermionic emission or a tunnelling mechanism from the electrode to the organic layer in a conventional device, as shown in Fig. 3.4(a). To reduce the injection barrier, electrical doping is widely used. However, the injection current still depends on the work function (W_F) of the electrode, even in the doped organic films.^{96,97} This problem is covered by the new pn-i-p structure supplying holes to the electrode and electrons to the emission layer simultaneously from the interface of the junction, as shown in Fig. 3.4(b). Because of the different mechanisms of electron injection, the electron injection ability must be independent of the work function of the cathode.

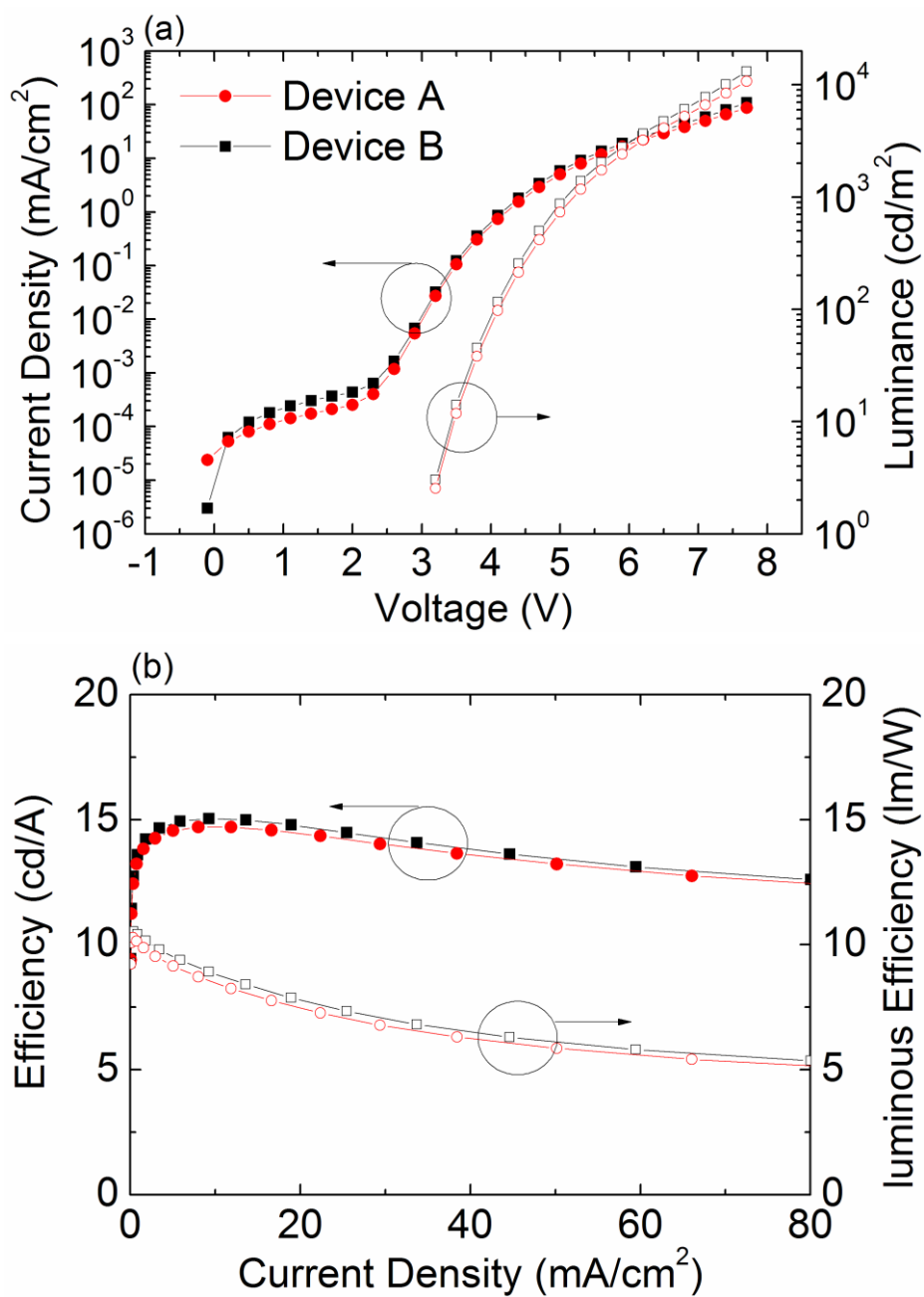


Fig. 3.3 (a) Current density-voltage-luminance ($J-V-L$) characteristics and (b) current and luminous efficiencies of the iOLEDs with p-CuPc/n-Bphen (device A) and n-Bphen (device B) as the electron injection layer, respectively.

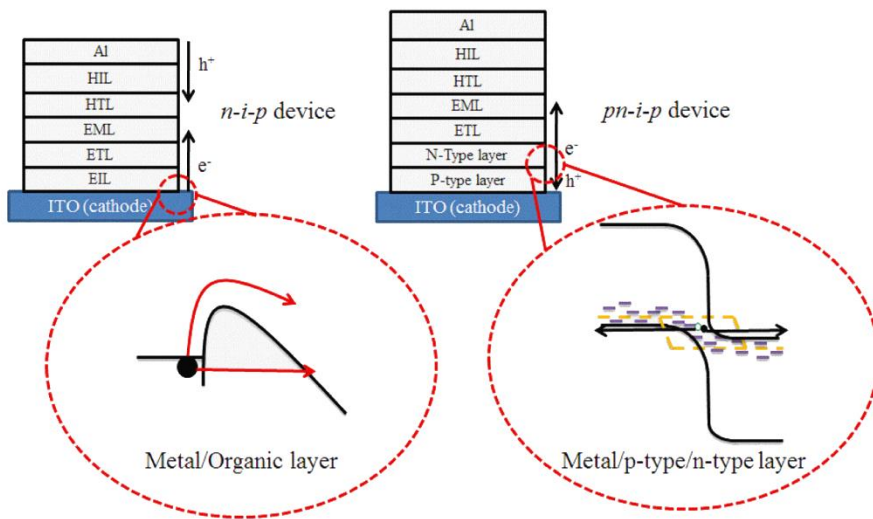


Fig. 3.4 Schematic diagrams illustrating the electron injection mechanism in (a) a normal electrode/organic junction and (b) an electrode/p-n junction.

The advantage of the new EIL based on the p-n junction was confirmed by the iBOLEDs with three different cathodes of PEDOT:PSS, UV-O₃ treated ITO and non-treated ITO electrodes. PEDOT:PSS is spin-coated on ITO glass at 4000 rpm for 40 s, followed by baking at 200°C for 5 min to achieve a thickness of 40 nm. The W_{FS} of PEDOT:PSS, UV-O₃ treated ITO and untreated ITO are 5.2 eV, 4.9 eV, and 4.5 eV, respectively. The $J-V$ and $L-V$ characteristics of the iBOLEDs with different bottom electrodes are shown in Fig. 3.5(a) and (b), respectively. For direct comparison, the structures of devices A and B in Fig. 3.3 were adopted once again except for the bottom electrodes. Devices C and D with an n-i-p structure were prepared on the non-treated and UV-O₃ treated ITO electrodes, respectively, and devices E and F with a pn-i-p structure were also set on the UV-O₃ treated and non-treated ITO electrodes, respectively. Finally, device G with a pn-i-p structure was fabricated on a PEDOT:PSS electrode. Devices C and D showed remarkable differences in their $J-V$ and $L-V$ characteristics. The V_{inject} and $V_{turn-on}$ values of device C are 2.4 V and 3.1 V, respectively, however, those of device D are 2.8 V and 3.9 V, respectively. These differences are attributed to the bottom electrode modification within the n-i-p structured device. The situation is, however, somewhat different when the pn-i-p structured iBOLEDs with various electrodes are compared. Device E has V_{inject} and $V_{turn-on}$ values of 2.4 V and 3.1 V, respectively, and those of device F are 2.4 V and 3.2 V, respectively. Moreover, the $J-V$ and $L-V$ characteristics of device G with the PEDOT:PSS electrode also show little deviation from those of the two devices. Device G has a V_{inject} value of 2.5 V and a $V_{turn-on}$ value of 3.3 V, respectively, and the minor differences may come from leakage currents compared to other devices.

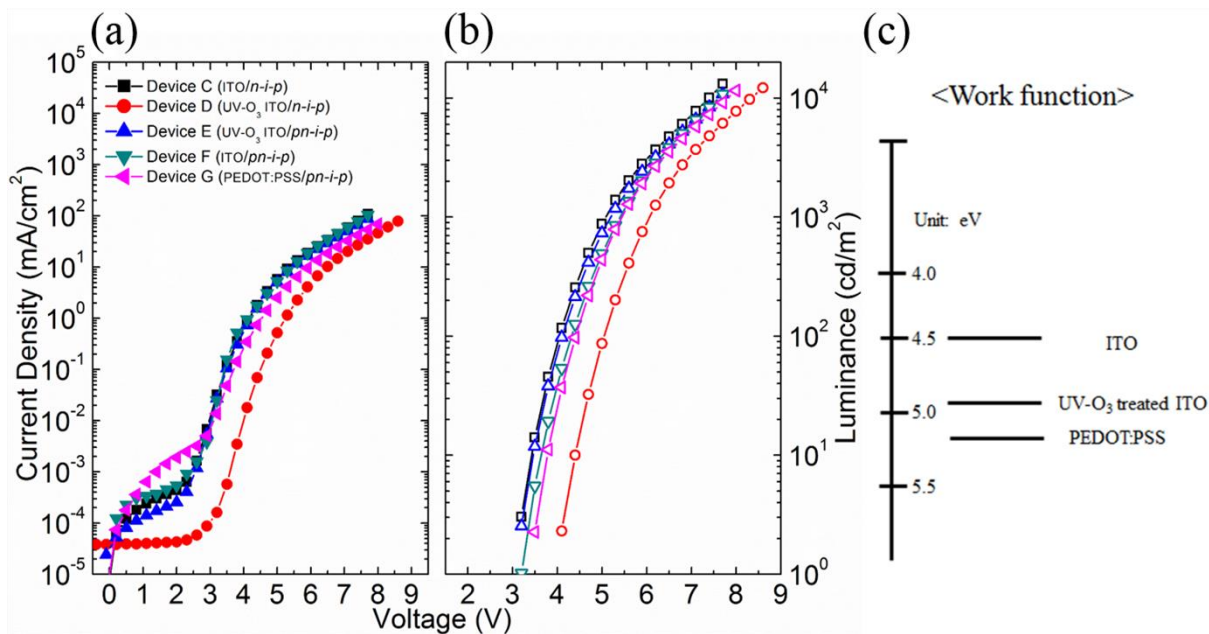


Fig. 3.5 (a) Current density–voltage (J – V) characteristics and (b) luminance–voltage (L – V) characteristics of the inverted OLEDs with n-Bphen (devices C and D) and p-CuPc/n-Bphen (devices E, F, and G) as the electron injection layer fabricated on UV-O₃ treated (devices D and E) and non-treated ITO electrodes (devices C and F) and on PEDOT:PSS (device G), respectively. (c) The work function of the bottom electrodes are indicated.

3.4 Conclusion

In summary, an organic p-n junction was successfully adopted as a new EIL for iBOLEDs. The organic p-n junction composed of a p-CuPc/n-Bphen layer showed almost the same electron injection characteristics for the cathodes with different work functions whereas the injection characteristics of the n-Bphen EIL significantly depends on the work function of the cathode. These facts indicate that the new pn-i-p structure with the organic p-n junction can be efficiently applied for high performance flexible organic electronics, regardless of the electrodes.

Chapter 4. A high performance transparent inverted OLED with 1, 4, 5, 8, 9, 11-hexaazatriphenylene-hexacarbonitrile as an organic buffer layer

4.1 Introduction

In recent years, OLEDs have been successfully introduced in the market as small size displays, and they have gradually expanded toward large size displays such as TVs. Furthermore, OLEDs have not only replaced the existing displays, but have also opened the door for new applications which are not easily attainable with other displays. One example is the technology of transparent OLEDs which are integrated into windows, eyeglasses displays, or head-up displays in automobiles. OLEDs are the best candidate for transparent displays because the organic materials used for the devices are transparent in the visible spectrum range, and the devices are thin and processible at low temperatures.

The structure of conventional OLEDs must be significantly modified to realize high performance transparent OLEDs. First of all, the most widely used Al cathodes must be replaced by a transparent electrode. Various transparent conducting oxides (TCOs), such as ITO, IZO, and Al doped zinc-oxide (AZO), have been used to replace the Al electrode with very limited success.⁹⁹⁻¹⁰² The TCOs are mostly deposited by a sputtering process under oxygen plasma which easily degrades OLEDs composed of soft organic materials. Moreover, reproducibility is not guaranteed. To solve the problem, thin metals such as Ag, Ag-Mg, Au and

multilayers such as ITO/metal/ITO, tungsten oxide (WO_3)/Ag/ WO_3 , silicon dioxide (SiO_2)/Ag/ SiO_2 , and Al/Al doped SiO_2 have been used.^{58,99,1,103-107} Even though such electrodes can achieve a low sheet resistance of less than $10 \Omega/\square$, form a good electrical contact with the organic layers, and have a high transparency of around 80% at a certain spectral range, they showed poor electron injection properties and their transmittances were not as good as the performance of the TCOs when the whole visible light spectrum is considered. Because of these reasons, the best performed transparent OLEDs reported up to now show results below 40 cd/A and 30 lm/W, which is much poorer than the conventional bottom emission OLEDs which show about 90 cd/A and 100 lm/W with green light emission.^{4,108}

Secondly, the opaque low temperature poly-silicon (LTPS) based backplane must be replaced by a transparent backplane. Recently, the performance of oxide TFTs have been significantly improved and become good candidates as transparent backplanes, not only because of their high transparency in the visible range, but also because of their high carrier mobility, flexibility, low temperature processing, and improved stability. Even solution processing is actively studied now. For high efficiency transparent OLEDs, not only the OLED part but also the backplane part must have a high transparency over 70% in the visible range.^{100,109,110} Therefore, oxide TFTs are preferred to opaque silicon based TFTs, and inverted OLEDs are required for stable performance of the device, since the oxide TFTs are n-type in contrast to the p-type LTPS.³²

Finally, a stable buffer layer must be additionally formed between a TCO and the organic layers to protect the underlying active organic layers from damage during the sputtering process. The desirable buffer materials are the ones possessing little

absorption of light in the visible wavelength and a good charge injection performance from a TCO. Furthermore, they can be deposited directly onto the organic layer without any damage to the organic layers, preferentially by thermal evaporation at low temperature. Although various organic and inorganic materials, such as Ni(acac)^{100,101} CuPc,¹⁰² WO₃,¹⁰⁸ PEDOT:PSS,¹¹¹ pentacene,¹¹² 3,4,9,10-perlyenetetracarboxylic dianhydride (PTCDA),¹¹³ and 2,9-dimethyl-4,7 diphenyl-1,10-phenanthroline (BCP)/Li,¹¹⁴ have been adopted for a buffer layer to OLEDs, the efficiencies of the devices were still low. For the improvement of the performance, a stable and easily controllable buffer material is required. Low efficiency in the most of the references except the ref. 108 is related to the improper buffer layers exemplified by the high leakage current or improper charge injection from electrode to organic layer. The ref. 108 reported low leakage current and good injection when the thickness of the WO₃ buffer layer becomes 60 nm. In the case, however, the refractive index of the WO₃ is about 2.3 at the visible wavelength¹¹⁵ so that large amount of the emitted light is expected to be waveguided in the layer, resulting in a reduced efficiency. For the improvement of the performance, a stable and easily controllable buffer material with low refractive index is required.

In this chapter, 1, 4, 5, 8, 9, 11-hexaazatriphenylene-hexacarbonitrile (HATCN) was employed as an organic buffer layer between the active layer and the IZO top electrode to realize a high performance inverted transparent OLED. HATCN, a discoid organic molecule possessing a deep lying LUMO level, good hole injection characteristics,¹¹⁶⁻¹¹⁹ low refractive index of about 1.7 in the visible wavelength¹²⁰ and very high stability even in ambient air conditions, is thermally evaporated at low temperature below 300°C in vacuum. The device showed a total maximum

luminance and a power efficiency of 67 cd/A and 67 lm/W, respectively, when the emitted lights through both the bottom and top sides are summed, and this is almost double the efficiency compared to the best values reported up to now in transparent OLEDs, to the best of our knowledge. The experimental data showed excellent agreement with the optical simulation results based on classical electromagnetic theory with a full vectorial approach. The fact indicates that HATCN not only perfectly protects the organic active layers from sputtering bombardment, but also acts as a good hole injection layer even after sputter bombardment. Moreover, the inverted OLEDs showed the best transmittance reported up to now with an average transmittance of 81% in the visible spectrum range.

4.2 Experimental

Device fabrication: The transparent OLEDs have the structure of indium tin oxide (ITO) (70 nm)/cesium carbonate (Cs_2CO_3) (1 nm)/B3PYMPM (30 nm)/TPBi (15 nm)/8 wt. % Ir(ppy)₃ doped CBP (15 nm)/TAPC (40 nm)/HATCN (50 nm)/IZO (60 nm). The device structure and the chemical structure of the materials used as the HTL and ETL are shown in the Fig. 4.1. The organic layers were successively deposited at a base pressure of $< 5 \times 10^{-7}$ Torr on pre-cleaned 70 nm-thick-ITO patterned glass substrates, and then the substrate was transferred to another chamber through a load-lock chamber to form an IZO anode on top of the HATCN layer. The HATCN organic buffer layer was thermally deposited by a conventional thermal evaporator, and Cs_2CO_3 was used as the electron injection layer.

Characterization of devices and films: The *J-V-L* characteristics of the OLED devices were measured using a Keithley 237 semiconductor parameter analyzer and a Photo Research spectrophotometer (PR-650). A UV-Vis-NIR spectrophotometer (Cary 5000) was used for the optical measurement. Atomic force microscope (AFM) topographic and phase images of HATCN films on Piranha-treated wafers were taken using a PSIA XE-100 scanning probe microscope in the noncontact mode.

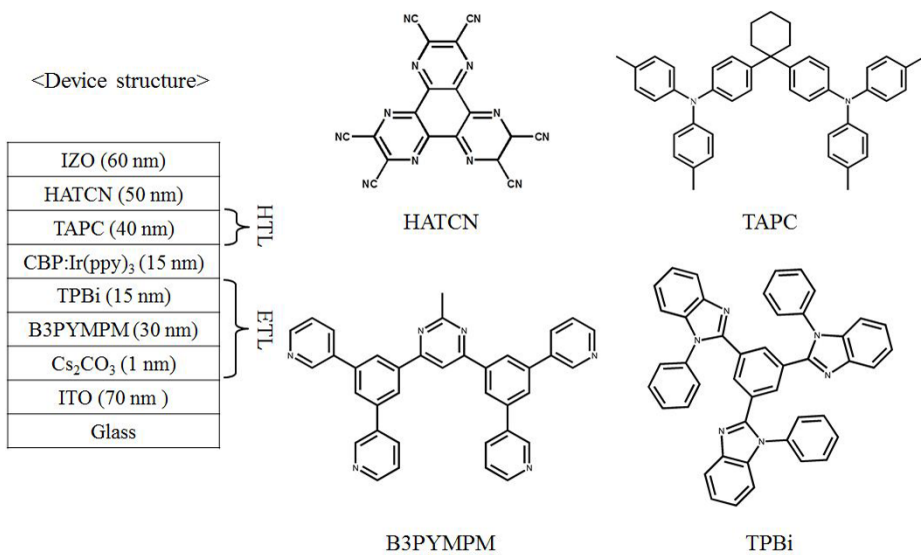


Fig. 4.1 Optimized structure of the transparent inverted OLED and the molecular structure of the organic materials.

4.3 Result and Discussion

First of all, an optical simulation, based on classical electromagnetic theory and developed by Chance, Prock and Silbey (CPS) with a full vectorial approach, was performed to obtain an optimized structure of the transparent inverted OLED.^{121,122} A simple structure of ITO (70 nm)/B3PYMPM (X nm)/CBP:Ir(ppy)₃ (15 nm)/TAPC (Y nm)/HATCN (50 nm)/IZO (60 nm) was used for the simulation. The thickness of the B3PYMPM and TAPC layer were systematically varied with the fixed thickness of other layers. After calculation, the structure is modified as displayed in Fig. 4.1 for electrical balance. The chemical structure of the materials used as the HTL and ETL are shown in the figure. A thin Cs₂CO₃ layer was inserted as an electron injection layer, and the TPBi layer is added between B3PYMPM and CBP layer to prohibit the formation of an exciplex at the interface of the two layers.^{37,84}

The calculated luminance efficiencies (LEs) of the transparent OLEDs are depicted as contour plots in Fig. 4.2 as functions of the HTL and ETL thicknesses for (a) the bottom emission, (b) the top emission, and (c) the sum of both emissions. It is interesting to note that the bottom emission is more influenced by the thickness of the ETL, and the top emission by the thickness of the HTL, due to the interference effect between the emitted and the reflected light. More light is emitted from the bottom glass side than the top IZO electrode side because more light is reflected at the IZO/air interface than the ITO/glass interface due to the high refractive index contrast. The simulation results predict that the maximum total LE of 70 cd/A can be obtained from the device structure when the thicknesses of the ETL and the HTL

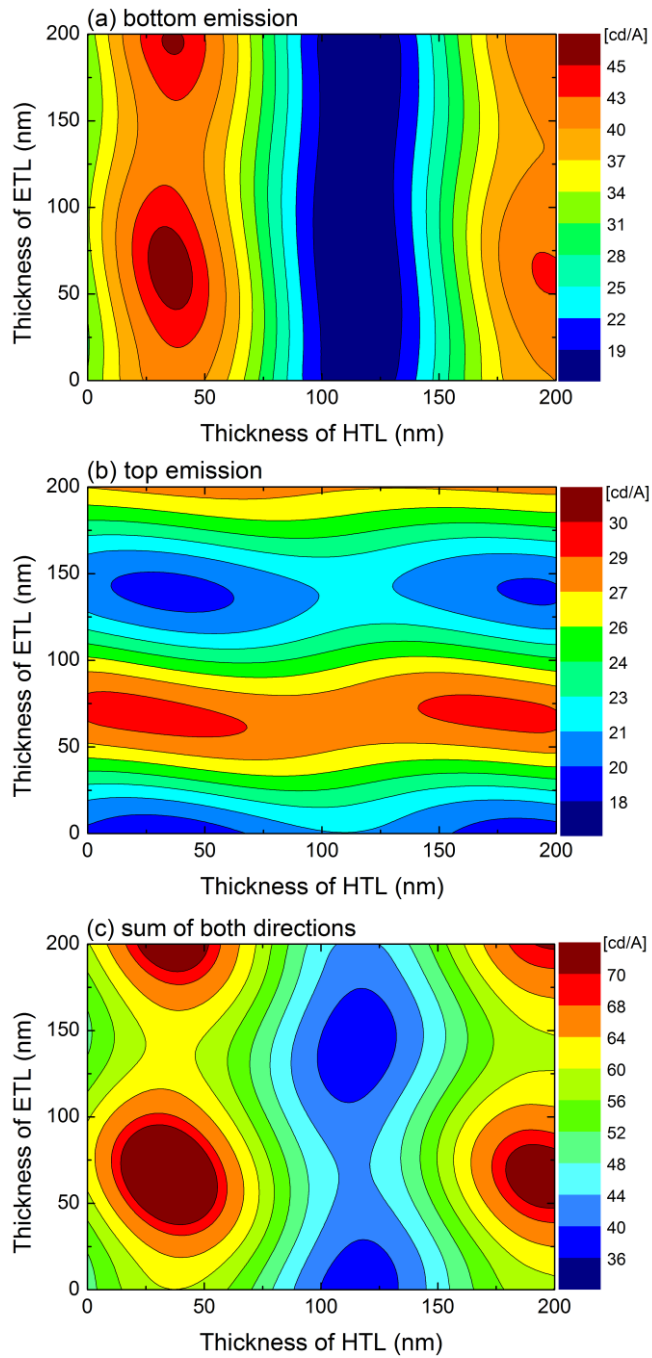


Fig. 4.2 Contour plots of luminance efficiencies (LEs) of the transparent OLEDs as functions of the hole transporting layer and electron transporting layer thicknesses, according to the emission direction; (a) is the case of bottom emission, (b) is the case of top emission, and (c) is of sum of both directions.

are 50 nm and 40 nm, respectively (Fig. 4.2c). Figure 4.3 shows (a) the J - V - L characteristics and (b) the efficiencies of the device which has the same thicknesses of the layer obtained from the optical simulation. The device shows very low leakage current below 10^{-4} mA cm $^{-2}$, as shown in Figure 4.3(a), demonstrating that the HATCN layer successfully protects the organic layers from the sputtering damage during the deposition of the top IZO electrode. In addition, the V_{inject} is at 2.5 V in the device, indicating that the HATCN layer also performs as an efficient hole injecting layer even after the sputtering of the IZO layer on top of the HATCN layer. In contrast, the device fabricated without the HATCN layer showed a high leakage current and no light was observed from the device.

As predicted by the optical simulation, the device shows an asymmetric emission. More light is emitted from the glass/ITO side (bottom side) than the top IZO side, and the ratio between the bottom and top emission is almost 2:1. The maximum LEs of the device in the case of the bottom emission and that of the top emission are 44.2 cd/A, and 22.7 cd/A, respectively, as depicted in Figure 4.3(b). These experimental results agree excellently with the simulated results. Furthermore, the device is turned-on at voltage of 2.9 V, and both sides of the luminance are about 1 cd/m 2 each. The luminance and power efficiencies of the device are 53.3 cd/A, and 33.3 lm/W with a driving voltage of 5.0 V at 1,000 cd/m 2 , respectively, when the emitted lights through both the bottom and top side are summed. It is interesting to note that the voltage gap between V_{inject} and $V_{\text{turn-on}}$ is just 0.4 V, indicating not only a good balanced injection of the electrons and holes, but also a good performance of the HATCN as the organic buffer layer. One of the most important factors in transparent OLEDs is, of course, the transparency of the device. Figure 4.4 shows

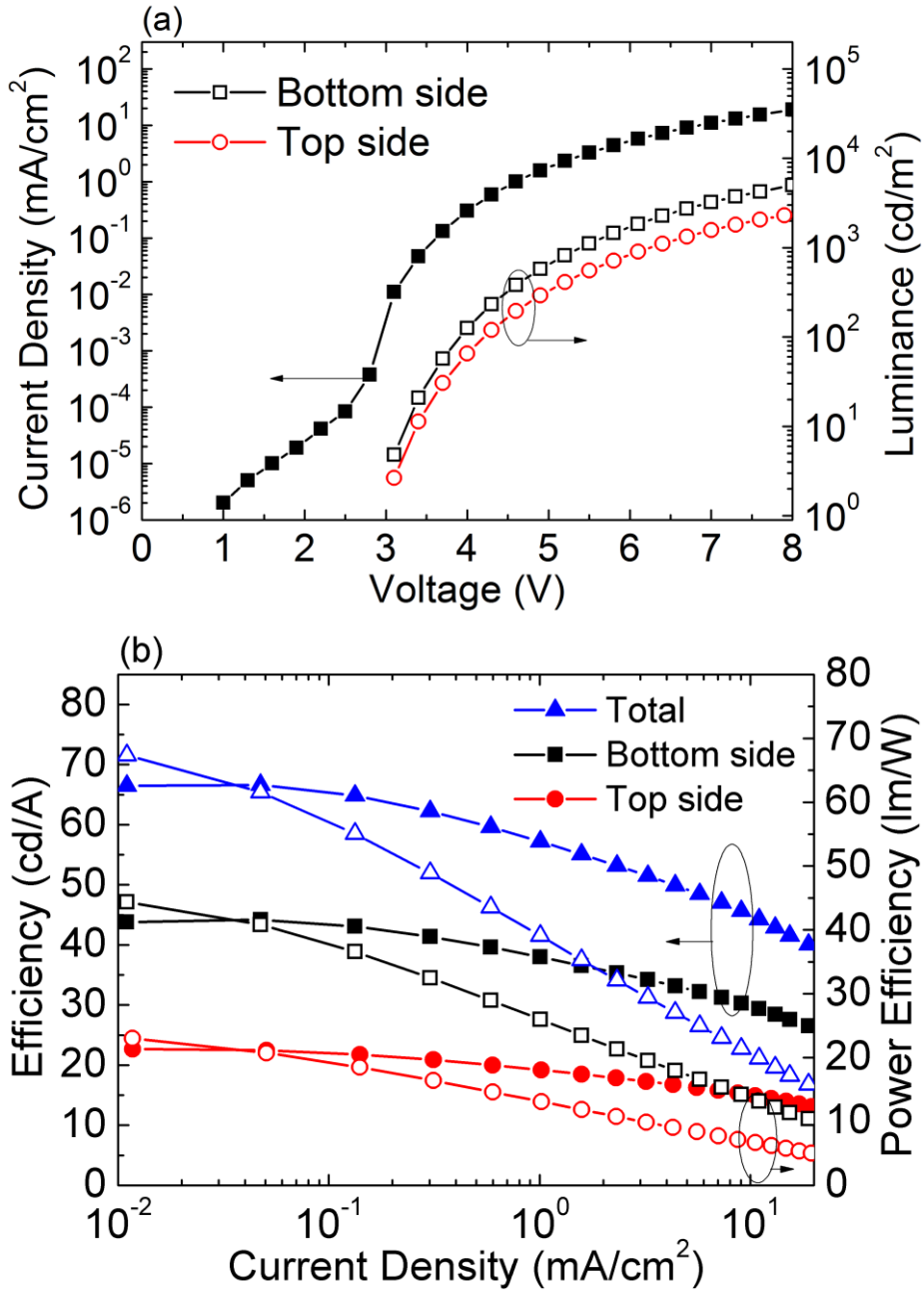


Fig. 4.3 The electrical and optical characteristics of the transparent inverted OLED; (a) current density-voltage-luminance (J - V - L) characteristics, and (b) current and power efficiencies, depending on the emission direction, bottom emission through the glass substrate (square), top emission through the IZO electrode (circle), and total sum of both emission (triangle).

transmittance of the device in the visible light region, and photographs before and after the turn-on of the device. The value of the transmittance includes whole layers with both transparent electrodes. For comparison, the transmittance of ITO/glass is additionally included in the figure. It is very interesting to note that the difference of the transmittance between the whole device and the ITO/glass itself is very low with an average excess loss of 5%, and the transmittance of the device is even higher than that of the ITO/glass in the range from 400 nm to 460 nm because of the interference effect. The average transmittance of the device in the whole visible light region is about 81%, which is the highest reported value up to now,^{99,101,102,108} and this value is represented as the dashed line in Fig. 4.4. When the device is turned off, the background images are clearly seen.

All the results clearly show that the HATCN layer plays three very important roles for the high performance transparent OLEDs at the same time: protection of the organic layer from IZO sputter bombardment, efficient hole injection, and high transparency. Since the molecular structure of HATCN is a discoid shape as shown in Fig. 4.1, and HATCN has crystalline structure with a complex hexagonal arrangement,¹²³⁻¹²⁵ the HATCN layer can effectively protect the underlying organic layer from the high energy of the sputtering if it is densely built up by thermal evaporation. In addition, HATCN has deep-lying LUMO level under 5.0 eV so that it is chemically stable against oxygen.^{117-119,126,127} The LUMO level of the HATCN layer is even lower than that of 7, 7, 8, 8-tetracyanoquinodimethane (TCNQ) which is a well-known stable n-type material under ambient conditions.¹²⁸ More than that, the low LUMO level of HATCN facilitates efficient hole injection from the IZO electrode to the organic layer.^{117-119,129} HATCN was easily controlled by using a

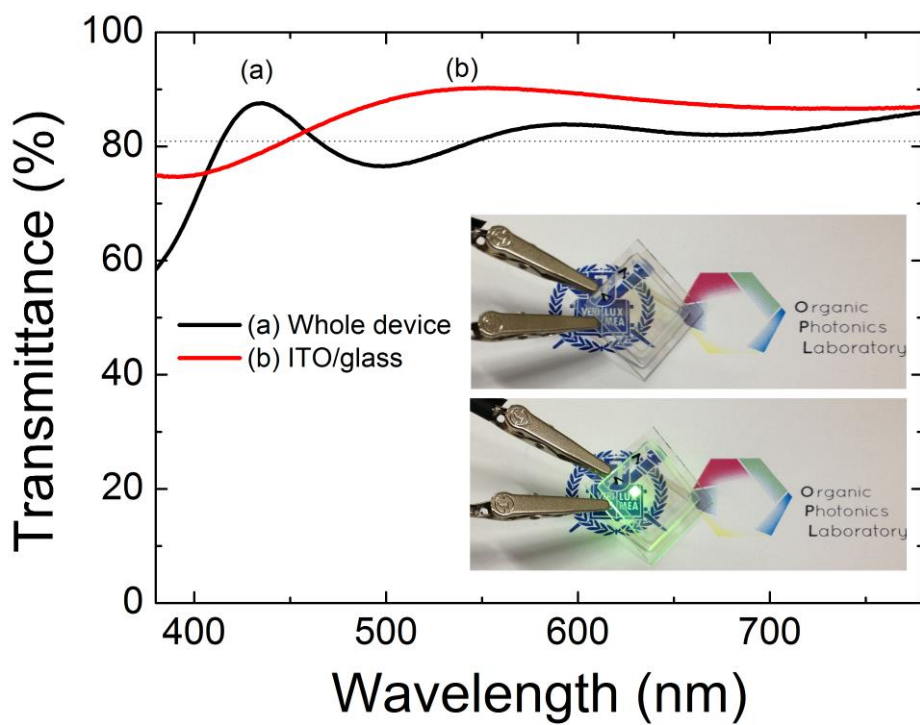


Fig. 4.4 Transmittance of (a) the transparent inverted OLED and (b) the ITO/glass itself in the visible light region, and photographs before and after turn-on of the device. The average transmittance of the device is about 81%, and the value is represented as the dashed line.

conventional evaporator because of its stability, even in air. Of course, HATCN is transparent in the visible wavelength region. All the characteristics of HATCN lead the material to be the best candidate as a buffer layer in transparent OLEDs.

To confirm how HATCN is grown onto the organic layer and to elucidate the stability under the sputtering condition, the surface morphology and phase were investigated using an AFM before and after O₂ plasma treatment, and the results are shown in Figure 4.5. For direct comparison, two different structures are used: (1) ITO/TAPC (40 nm), and (2) ITO/TAPC (40 nm)/HATCN (50 nm). Figures 4.5(a) and (d) show the topography of the pristine films (1) and (2), respectively, and Figures 5(b) and (e) show the phase of the thin films (1) and (2) before O₂ plasma treatment, respectively. Both the topography and phase are significantly changed when the HATCN is additionally deposited onto the organic layer. The surface of the TAPC layer is smooth with a peak to valley roughness (R_{pv}) of 6.2 nm (Figures 4.5a and b). In contrast, the HATCN grows with a columnar structure as expected with a much larger R_{pv} of 19.6 nm (Figures 4.5d and e), indicating that the rigid disk shaped HATCN grows with a compact face-on arrangement.

However, the situation is significantly changed after O₂ plasma treatment. After O₂ plasma treatment for 2 min., the morphology of the TAPC film becomes rough with an R_{pv} of 15.2 nm, as shown in Figure 4.5(e). The root mean square roughness (R_{rms}) of the film increases by 2.9 times from 0.8 nm to 2.35 nm after the O₂ plasma treatment. On the other hand, the TAPC/HATCN thin film became smooth by the O₂ plasma treatment. The R_{pv} value was decreased from 19.56 nm to 16.83 nm in Figure 4.5(f), and the R_{rms} value was also decreased from 2.55 nm to 2.22 nm. The values are summarized in Table 2. From the data, it was concluded that HATCN has a high

resistance after O₂ plasma treatment due to its deep lying LUMO level and its columnar structures after deposition onto the organic layer of TAPC. As a result, it effectively reduces the sputtering damage, resulting in the realization of a high performance transparent inverted OLED.

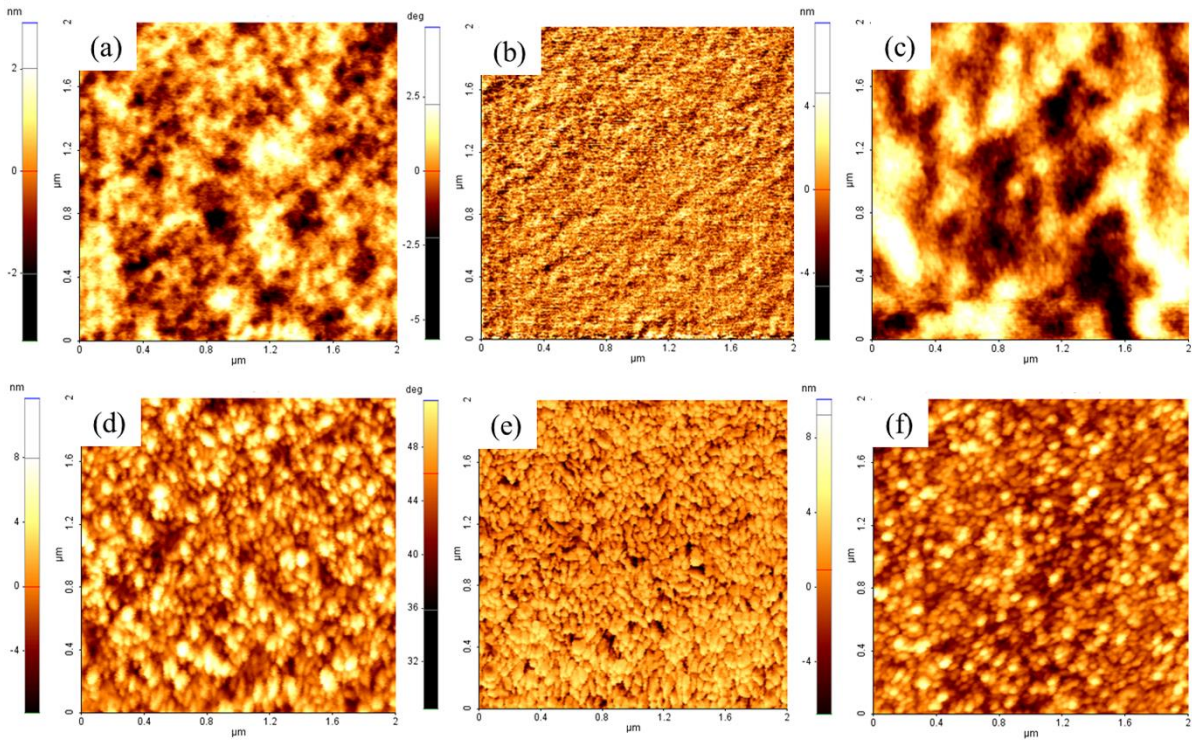


Fig. 4.5 Surface morphology and phase images of a 40 nm thick TAPC film on ITO ((a) and (b), respectively), and a 50 nm thick HATCN grown on the ITO/TAPC (40 nm) ((d) and (e), respectively) measured using an AFM, before O₂ plasma treatment. After the O₂ plasma treatment, the morphology of (c) the TAPC thin film is significantly changed compared to that of (f) the HATCN thin film.

Table 2. The morphology characteristics of the two thin films from the AFM measurement before and after O₂ plasma treatment. R_{pv} is the value of the peak to valley roughness, and R_{rms} is the value of the root mean square roughness.

Film and treatment conditions	R _{pv} (nm)	R _{rms} (nm)
TAPC (before the O ₂ plasma)	6.22	0.8
TAPC (after 120 sec. O ₂ plasma)	15.17	2.35
TAPC/HATCN (before the O ₂ plasma)	19.56	2.55
TAPC/HATCN (after 120 sec. O ₂ plasma)	16.83	2.22

4.4 Conclusion

In summary, a very high performance transparent inverted OLED was demonstrated using HATCN as the buffer layer between a hole transporting layer and the IZO electrode. The HATCN layer performed three important roles: protection of the underlying organic layers from sputter damage during the IZO deposition, efficient hole injection and high optical transparency. AFM measurements confirmed that the rigid disk shaped HATCN molecules were deposited with a columnar structure on a hole transporting layer, and that it has high resistance against O₂ plasma damage, protecting the underlying organic layers from the bombardments of the IZO sputtering. The low LUMO level of HATCN facilitates efficient hole injection from IZO. As a result, a very high luminous and power efficiency of 67 cd/A, and 67 lm/W were obtained, respectively, and this experimental data excellently agrees with the optical modelling. In addition, the device showed high transparency with an average transmittance of 81% in the visible range. It is expected that the transparent inverted OLED developed in this chapter can be directly adapted to a high performance transparent flexible display based on oxide thin film transistors because of its inverted structure.

Chapter 5. Molecular alignment and nanostructure of HATCN thin films on organic surfaces

5.1 Introduction

1, 4, 5, 8, 9, 11-Hexaazatriphenylene-hexanitride (HATCN) is a strongly electron-deficient molecule with a deep-lying lowest unoccupied molecular orbital (DL-LUMO) level.^{117-119,126} Recently, transition metal oxides (TMOs) or organic dopants possessing a DL-LUMO level have received significant attention for their powerful roles in organic semiconductors. TMOs or organic dopants not only increase the conductivity and carrier density of organic films when they are doped in an organic semiconductor,^{52-55,78,130-133} thin layers of the materials can enhance the injection efficiency of charge carriers from the electrode to the organic layer by adjusting the work function of the electrode.^{129,134,135} HATCN behaves similarly to TMOs and has, therefore, been widely used as a hole injection layer (HIL) or an interconnection unit (ICU) in tandem organic light-emitting diodes (OLEDs) and organic photovoltaic cells (OPVs).^{116,117,136-139} In contrast to TMOs, however, HATCN is highly conductive and transparent, even in layers that are several tens of nanometers thick, thereby minimizing optical and electrical power loss and improving the performance of organic electronic devices. HATCN has a refractive index of 1.7 lower than that of other TMOs, and it effectively protects organic layers below the HATCN layer from sputtering damage during the formation of a transparent electrode.¹⁴⁰ Pristine HATCN layers have been widely used in place of

doped layers because the doping efficiency of HATCN in organic semiconductors is relatively low.^{53,98}

The good electrical properties of a pristine HATCN layer may be related to the morphology and orientations of the film. The morphology and orientations of the HATCN films have been studied on metals surfaces and the previous studies reported that HATCN molecules rearrange on metal surfaces with increasing thickness. For instance, HATCN molecules stack with a face-on configuration during the initial stages of growth on metal surfaces, such as Au or Ag.^{124,141,142} The configuration transforms from the face-on to the edge-on configurations as the film thickness increases during island formation. HATCN islands preferentially orient along the (143) plane parallel to the Au (111) surface.¹⁴² In thick films, HATCN molecules do not show extensive π -stack, forming a complicated 3D hexagonal structure with 18 molecules in a unit cell.¹²³ However, the behavior of HATCN molecules on an organic layer has not been examined, to the best of our knowledge. In many cases, HATCN molecules form stacked structures on organic surfaces that act as HTLs or ETLs (hole- or electron-transporting layers) in tandem or inverted organic electronic devices.^{98,117,119,126,136,137} Furthermore, HATCN and typical HTLs such as TAPC, N,N'-diphenyl-N,N'-bis(1,1'-biphenyl)-4,4'-diamine (NPB), and 4,4',4''-tris(N-(2-naphthyl)-N-phenylamino)-triphenylamine (2-TNATA) formed organic hetero-junction so that they showed good electrical property by generating charge carriers at the junction interface.^{116-119,126,127,140} However, the crystallinity and nanostructure of such HATCN layers on organic surfaces have not been studied previously.

Here, the nanostructure and molecular alignment of HATCN molecules were examined on a typical HTL layer, TAPC, as well as on various ETLs, such as Bphen,

B3PYMPM, or TPBi by using x-ray analysis. The stability of the HATCN surfaces were additionally studied after the formation of a transparent indium zinc oxide (IZO) electrode by sputtering. HATCN molecules on these surfaces were stacked with a $(001)_{\text{hex}}$ preferred orientation on the TAPC layer. The ordered nano-grains retained their arrangement, even after the formation of an IZO layer. The preferential arrangement of HATCN molecules differed on each of the three different ETL surfaces. This is the first report describing the nanostructures and molecular arrangements of HATCN on practical organic surfaces.

5.2 Experimental

X-ray measurements: GISAXS (grazing incidence small-angle X-ray scattering) and GIWAXS (grazing incidence wide-angle X-ray scattering) measurements were performed at the 5A X-ray scattering beam line for materials science at the Pohang Light Source II (PLS-II) in Korea. The X-ray energy was 11.57 keV. The distance from the sample to the detector was 1801.6 mm for the GISAXS measurements and 440.7 mm for the GIWAXS measurements. A 2D image plate was used for both measurements. GISAXS and GIWAXS were all measured at an incidence angle of 0.20° , which was higher than 0.118° (measured by the X-ray reflectivity curve), the critical angle of HATCN films at 11.57 keV. Details of the method were described in our previous reports.^{143,144}

Morphology: Atomic force microscopy (AFM) topographic images of the HATCN films and IZO films on the organic films grown on Piranha-treated wafers were collected using a PSIA XE-100 scanning probe microscope in the noncontact mode. TAPC/HATCN films were deposited under a vacuum of 10^{-7} Torr on a Si wafer cleaned with a piranha solution. An IZO layer was formed on the HATCN layer by transferring a substrate to another chamber through a load-lock chamber.

5.3 Result and Discussion

Figures 5.1(a)-(c) show the grazing incidence small angle x-ray scattering (GISAXS) images of a HATCN film grown on a 20 nm thick TAPC layer. Figures 5.1(d)-(f) show GISAXS images of 50 nm thick HATCN films grown on various ETLs. Figures 5.1(a) and (b) show the separated wings derived from the structure factor, which is related to the correlation between nano-grains in the HATCN films. Separated wings were clearly observed in the horizontal line cuts, as shown in Fig. 5.1(g). The distance between wings followed the relation, $DQ_{||} = 4\rho/D_{ave}$, where D_{ave} is the average distance between grains. The full width at half maximum (FWHM) of the wings provides the average grain size, i.e., $FWHM = 2\pi/L_{ave}$, where L_{ave} is the average grain size. As shown in Fig. 5.1(g), the wings were observed after the formation of a transparent IZO electrode on the HATCN film via a sputtering process, indicating that the HATCN nano-grains were not affected by the sputtering process. The thickness of the IZO film was 10 nm, in this case. It is interesting to note that the scattering wings of the GISAXS were not observed on the ETL surfaces, as shown in Fig. 5.1(d)-(f). The absence of scattering wings on the ETL surfaces were investigated by measuring the contact angle using water droplets on the film surfaces as shown in Fig. 5.2. The ETL surfaces were more hydrophilic than the TAPC surfaces. The contact angle of the TAPC surface was 84° , the value of which was consistent with the reported data,¹⁴⁵ whereas the contact angle was $43^\circ - 56^\circ$ for the case of the ETL surfaces (Bphen = 44° , B3PYMPM = 43° , TPBi = 56°). The contact angle of the HATCN surface was almost 0° because the HATCN film surface was

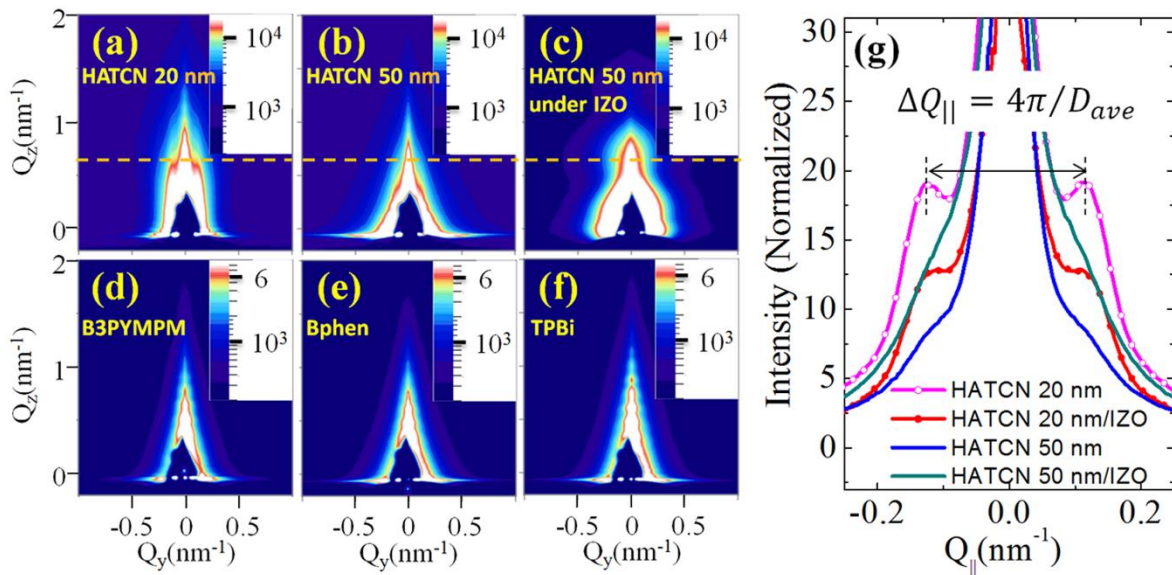


Fig. 5.1 GISAXS images measured at a 0.142° incidence angle. (a), (b) Two HATCN films, 20 nm and 50 nm thick, respectively, were grown on a 20 nm thick TAPC layer. (c) A 10 nm thick IZO layer was grown on a 50 nm thick HATCN film, which had been grown on a 20 nm thick TAPC layer. (d)–(f) 50 nm thick HATCN films grown on 20 nm thick B3PYMPM, Bphen, and TPBi layers, respectively. (g) Horizontal line cuts (dotted lines in (a)–(c)) of the GISAXS images of the HATCN films on a TAPC layer show the separated wings corresponding to regularly distributed HATCN nano-grains.

highly hydrophilic. These facts indicate that HATCN formed regularly arranged nano-grains on the relatively hydrophobic TAPC surface, whereas HATCN did not form grains and seemed to be perfect film on the hydrophilic surfaces, such as Bphen, B3PYMPM, and TPBi. The wings of the GISAXS data in the HATCN/TAPC film under the IZO layer indicate the presence of HATCN nano-grains after IZO sputtering. The effects of sputtering on the HATCN surface were elucidated by the x-ray off-specular reflection measurements, as shown in Fig. 5.3(a). The interference fringes (Kiessig fringes) in the x-ray specular reflectivity curves are related to the film thickness.¹⁴⁶ The period of the fringes is proportional to the inverse of the film thickness. Generally, interference fringes are not observed in the off-specular reflectivity curves due to a lack of correlation between the surfaces and the interfaces of the film. When a surface roughness is vertically correlated with the interface roughness, interference fringes are observed in the off-specular curves.¹⁴⁷

Figure 5.3(b) shows a schematic diagram of the specular and off-specular reflectivity measurements in reciprocal space. The offset angle for the off-specular measurement was 0.1° , which was enough to avoid the specular reflection because the rocking width of specular reflection at $2\Theta = 2^\circ$ was $0.03 \sim 0.04^\circ$. As shown in Fig. 5.3(a), the interference fringes were not observed in the HATCN films on the TAPC surface, indicating that the HATCN surface morphology did not correlate with the TAPC surface. In contrast, interference fringes were clearly observed in the HATCN films under the IZO layer. The film thickness, derived from the interference fringe, was 10.2 nm, consistent with the thickness of the IZO layer. The interference fringes in the HATCN films under IZO indicated that the IZO film was conformal on the HATCN grains, thereby retaining the inherent HATCN surface morphology.

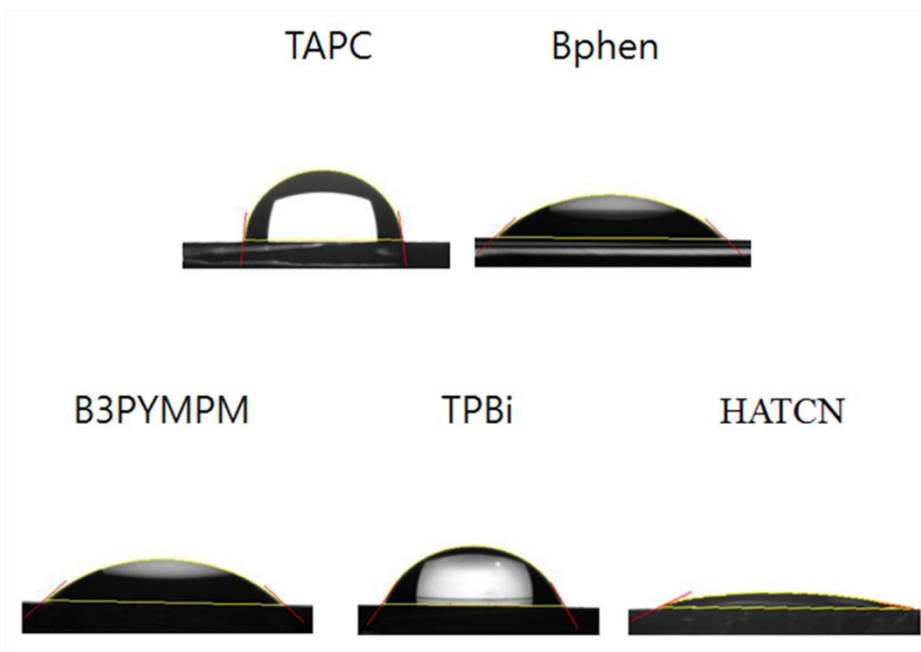


Fig. 5.2 Distilled water contact angle for TAPC, Bphen, B3PYMPM, TPBi, and HATCN, respectively.

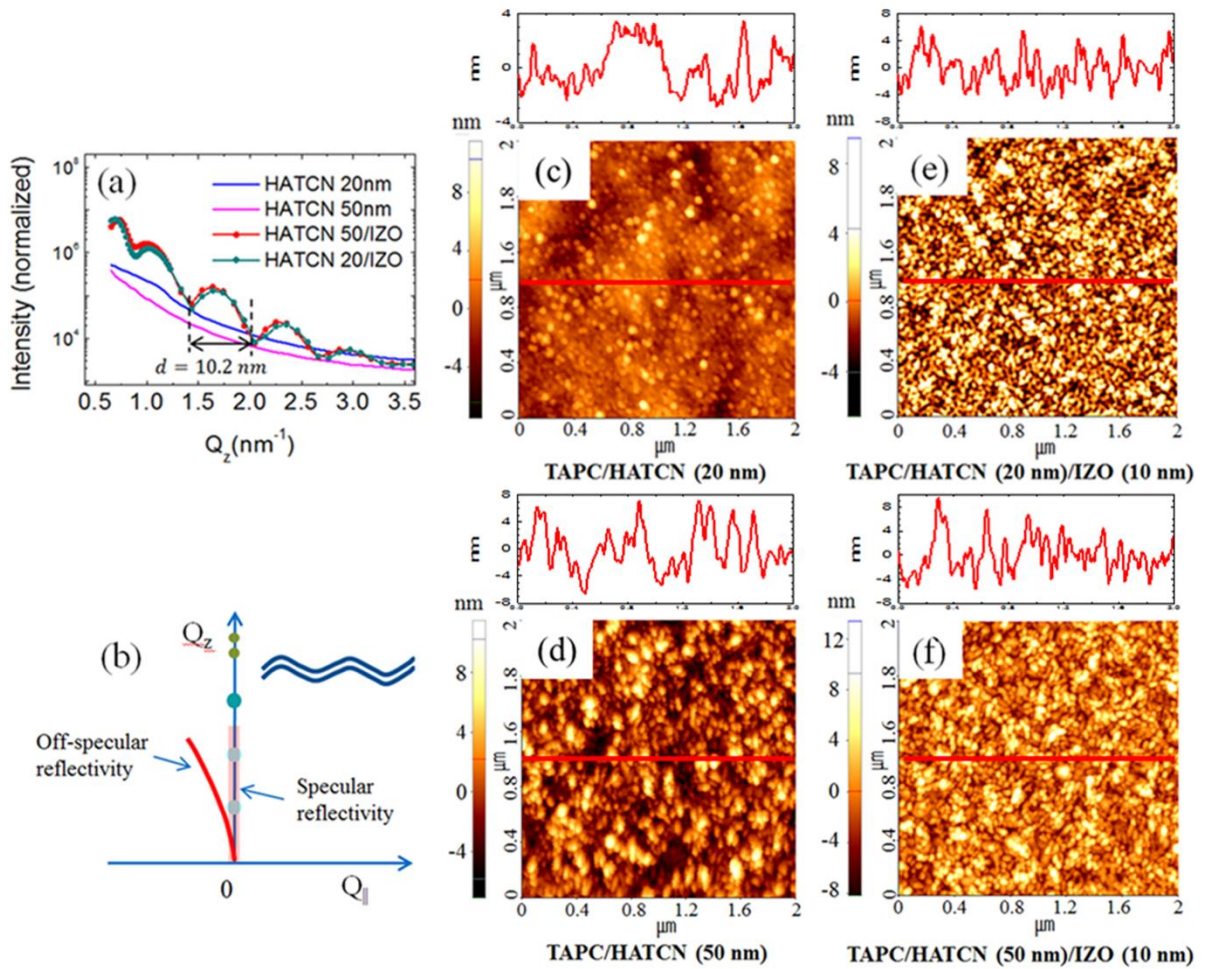


Fig. 5.3 (a) x-ray off-specular reflection data for the 20 nm and 50 nm thick HATCN layers grown on a 20 nm thick TAPC layer. The intensity modulations correspond to the 10 nm thick IZO layer grown on the HATCN layers. (b) Schematic diagram showing the specular and off-specular reflectivity in reciprocal space. (c)–(f) AFM images of the sample surfaces: TAPC/HATCN (20 nm), TAPC/HATCN (50 nm), TAPC/HATCN (20 nm)/IZO (10 nm), TAPC/HATCN (50 nm)/IZO (10 nm), respectively.

The AFM images of the HATCN films in Fig. 5.3(c)–(f) support the conformality of the IZO surface. Nanograin features were observed after the formation of an IZO layer, as shown in Fig. 5.3(e)–(f).

The average size and spacing of the nanograins were obtained through analysis of the scattering wings, shown in the horizontal line cuts of the GISAXS pattern. In order to clearly separate the SAXS wings, the line profile was fitted with 3 Gaussian peaks to consider the reflection rod at central position. Figure 5.4 shows the schematic diagram of the morphology obtained from the GISAXS analysis for HATCN films grown on the TAPC surface. For a 20 nm thick HATCN film, the average grain size and distance were 52 (\pm 17) nm. The grain size and distance slightly increase to 54 (\pm 20) nm in 50 nm thick HATCN films. The differences between 20 nm and 50 nm thick HATCN surfaces are the increase of the standard deviation at the 50 nm thick film, which means that the grains and the distance are more widely distributed in size and length in case of the 50 nm thick film. The HATCN surface apparently became rough as the film thickness increased due to island formation, as shown in Fig. 5.4, and these features were also observed in the AFM images shown in Fig. 5.3(c)–(f). As the thickness of the HATCN on the TAPC surface increases from 20 nm to 50 nm, surface morphology became rough. A peak-to-valley roughness (R_{pv}) and a root mean square roughness (R_{rms}) values in $2 \times 2 \mu\text{m}^2$ changed from 16.68 nm to 19.08 nm and from 1.79 nm to 2.71 nm, respectively. Moreover, relatively larger sized grains in the 50 nm thick HATCN layer were observed in the phase image of the films than those in the 20 nm thick HATCN layer shown in Fig. 5.5. The quantitative grain size of each film can hardly be estimated from the morphology and phase images directly so that power spectral density

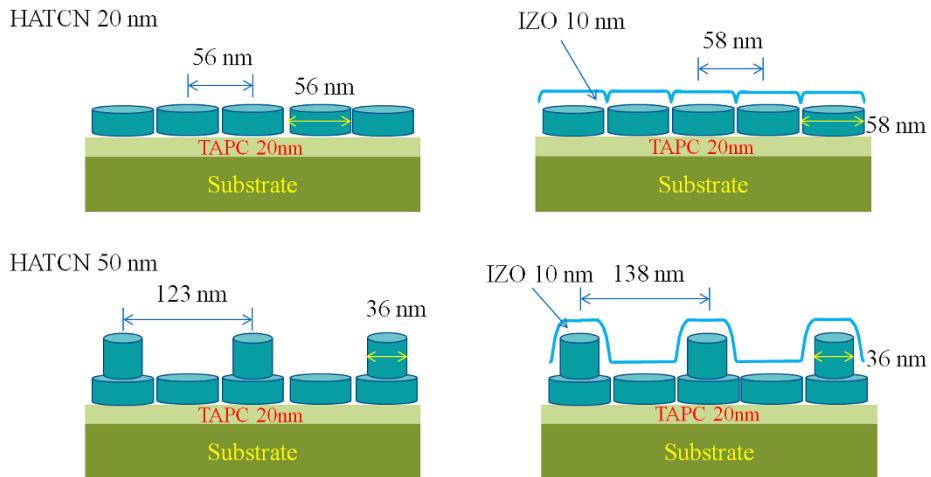


Fig. 5.4 Schematic diagrams of the HATCN nanograins on a 20 nm thick TAPC layer, based on the analysis of the GISAXS data. The morphology of the IZO layer grown by sputtering followed the HATCN nanograin morphology.

profiles from the images were additionally investigated using ABC of k-correlation model¹⁴⁸ to investigate the grain size of the films quantitatively in the figure 5.3(c) and (d). The model is defined as follows:

$$S(f) = \frac{A}{\left[1 + (B \times f)^2\right]^{\frac{C}{2}}}. \quad (1)$$

where A is related to the low frequency component of surface roughness, B is related to the grain size and C is the exponent of the power-law fall-of f at high frequencies. Fig. 5.6 shows the comparison between experimental and simulation results. From the analysis, the average grain size of the 50 nm thick HATCN was 68.8 nm and that of the 20 nm thick HATCN was 59.1 nm, respectively, and the results were comparable to the results from the x-ray analysis. Interestingly enough, the nano-grains and surface morphology were preserved under the sputtering formation of the IZO layer, as confirmed by the interference fringes in the off-specular x-ray reflectivity curves. Therefore, the 10 nm thick IZO layer was conformal on the HATCN grains, preserving the HATCN surface, as shown in Fig. 5.4. In these cases, the GISAXS wings mainly originated from the nano-grain features of the IZO surface.

The crystalline properties of the HATCN film were examined by GIWAXS (grazing incidence wide-angle x-ray scattering) measurement. Figure 5.7 shows a GIWAXS image of a 50 nm thick HATCN film grown on the TAPC surface. On the metal surface, the HATCN molecules were stacked along the (143) preferred orientation, as previously mentioned. In contrast, on the TAPC surface, the HATCN

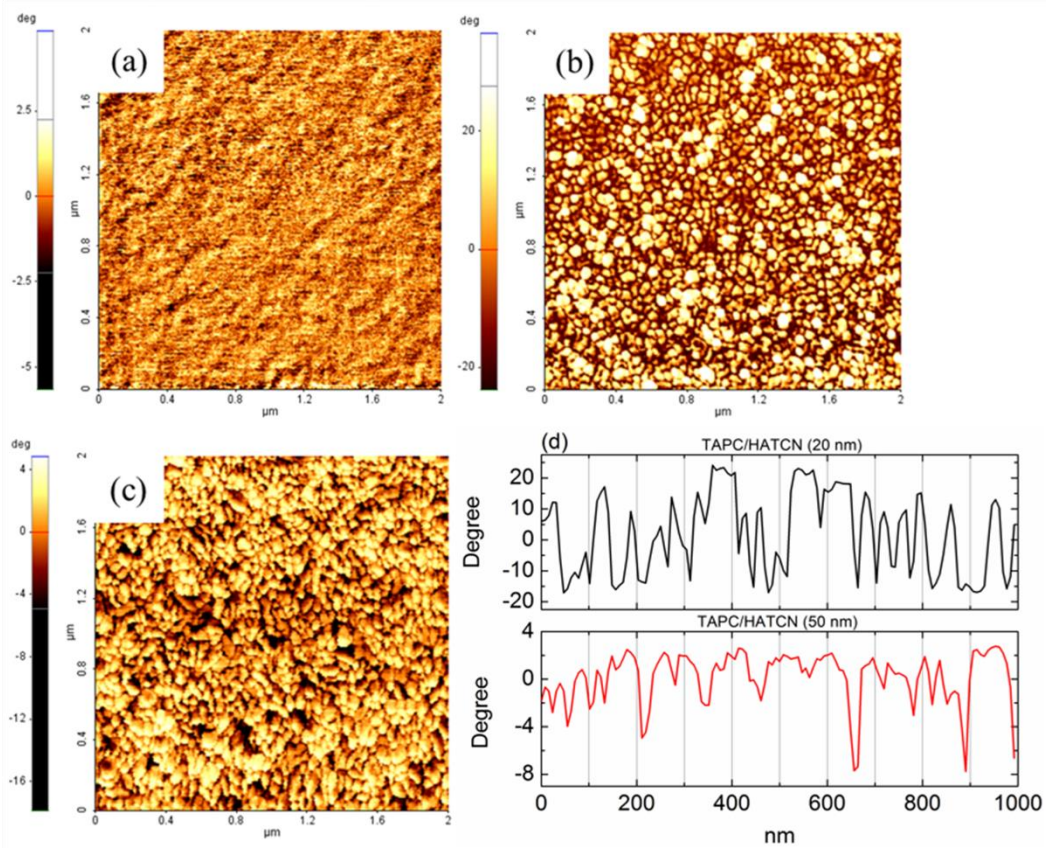


Fig. 5.5 The phase image of (a) TAPC (40 nm), (b) TAPC/HATCN (20 nm), and (c) TAPC/HATCN (50 nm), respectively, from AFM measurement. The figure (d) show the line scan images from the figure (b) and (c), respectively.

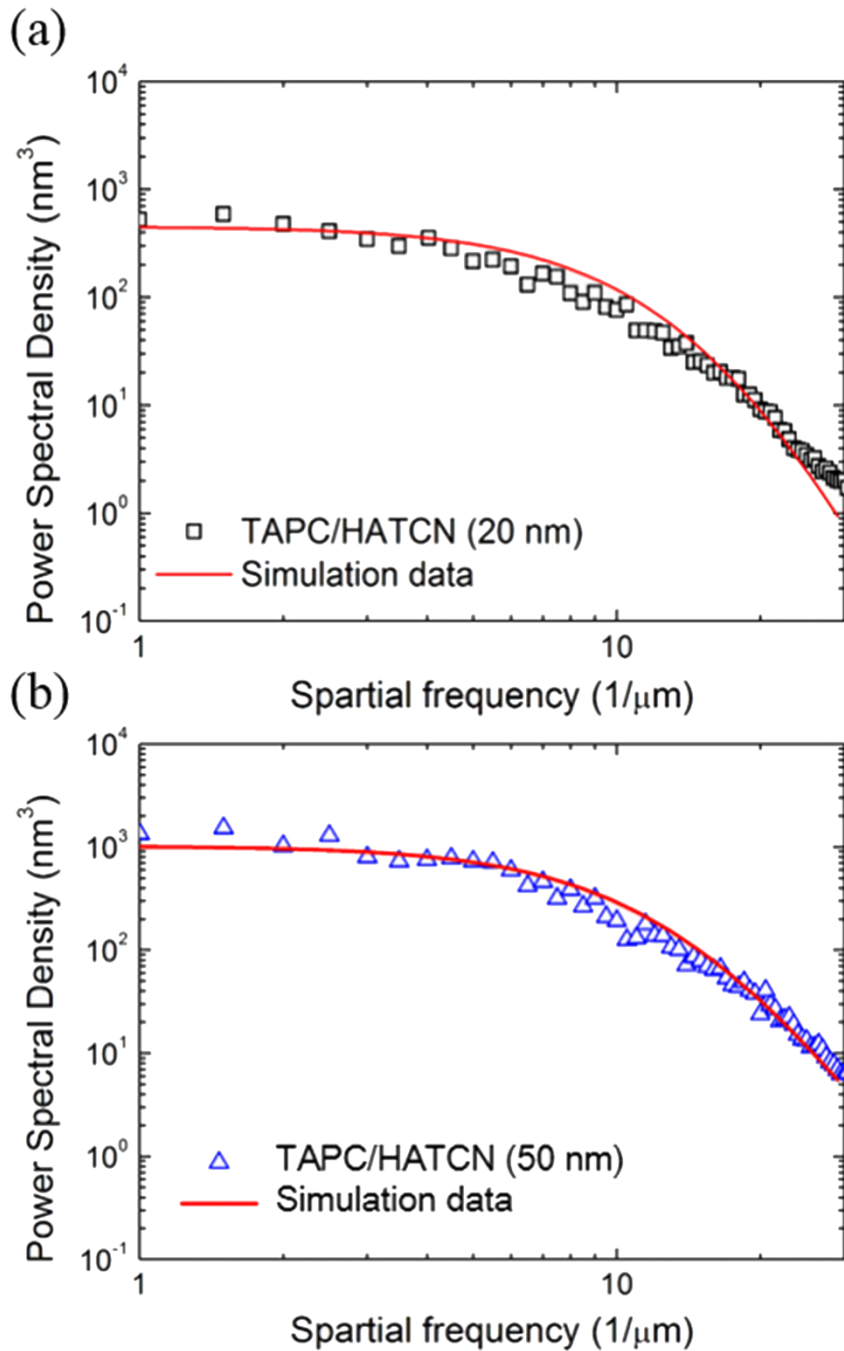


Fig. 5.6 Open symbols show Power Spectral Density (PSD) profiles of TAPC/HATCN (20 nm) and TAPC/HATCN (50 nm) films, respectively, from AFM measurements. Red line shows the simulation data using ABC model.

molecules were stacked along the (001) preferred orientation, as indicated in Fig. 5.7. The (110) and (220) peaks were observed in the horizontal direction, whereas a strong (003) peak was observed in the vertical direction. In the hexagonal system, (hk0) peaks were observed in the horizontal direction in a (001) preferred arrangement. The peaks relating to the intermolecular spacing, i.e., $d = 0.341$ nm and $d = 0.376$ nm, were also measured in the vertical direction; however, the peak corresponding to $d = 0.341$ nm was maximal at 45° relative to the surface normal, as shown in Fig. 5.7(a).

The crystallinity values of HATCN films on various ETL surfaces, including Bphen, TPBi, and B3PYMPM, were analyzed. Figure 5.8 shows the crystal size for the (110) and (003) HATCN diffraction peaks on the Bphen, TPBi, and B3PYMPM surfaces (error values are included in Fig. 5.8). The best HATCN film crystallinity was observed on the Bphen layer. In addition, the FWHM of the (001) peak along the circular direction was smallest on Bphen (23.0°) among them. (29.1° on TPBi and 29.2° on B3PYMPM) The integrated intensity of the (110) peak was also the largest on Bphen among them. (Bphen=92.8 cts, TPBi=64.1 cts, B3PYMPM=78.6 cts). Therefore, the crystallinity of HATCN was best in size, preferential ordering as well as peak intensity on Bphen.

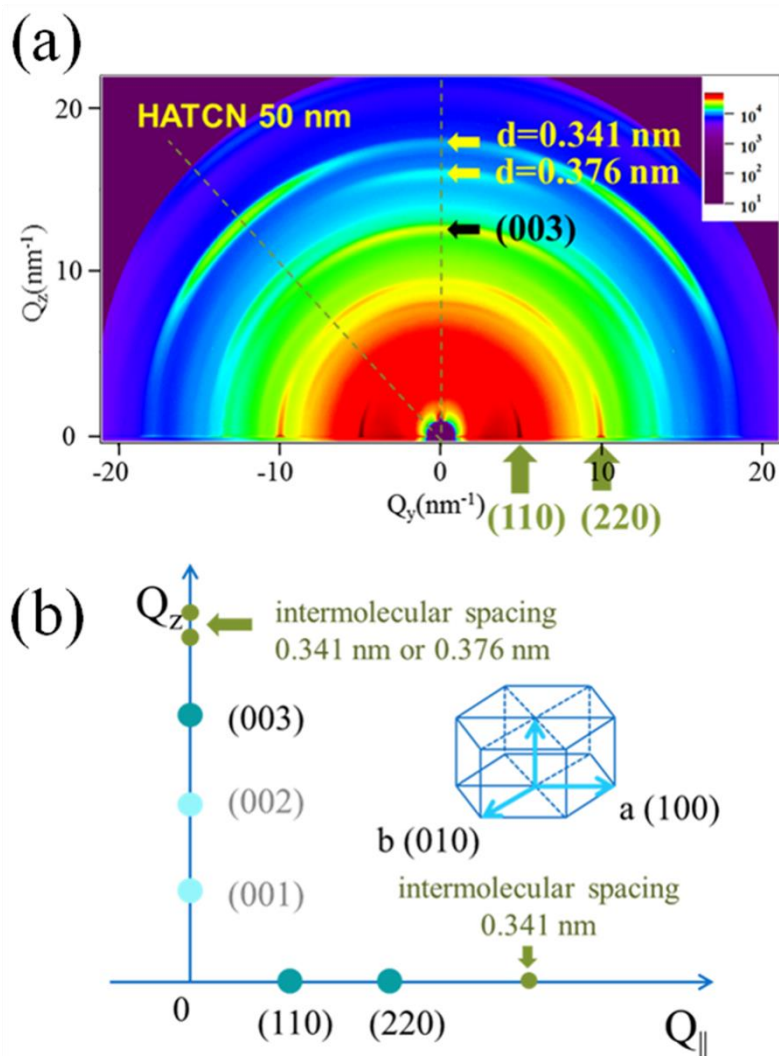
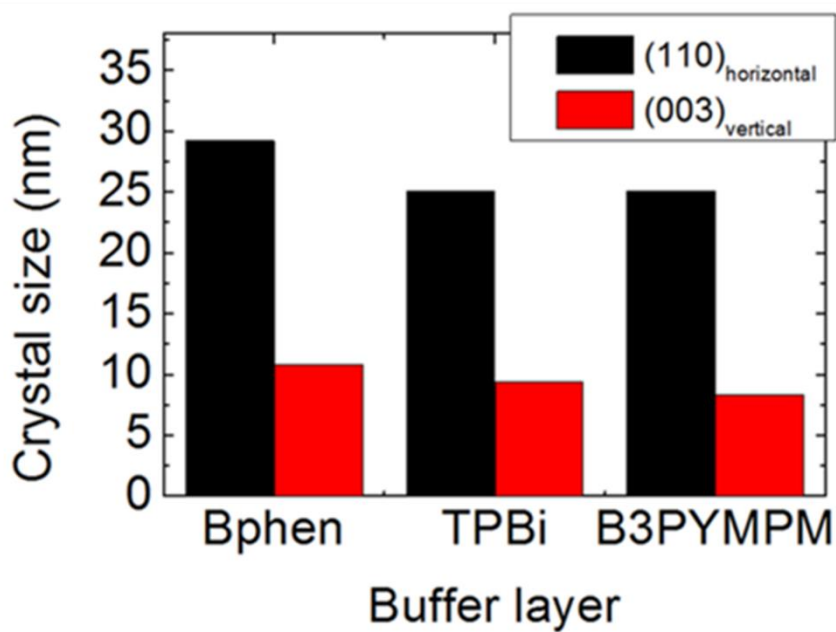


Fig. 5.7 (a) GIWAXS data of a 50 nm thick HATCN film grown on a 20 nm thick TAPC layer. (b) Reciprocal space of a preferentially ordered HATCN film with (001). In this configuration, (001) peaks are observed in the normal direction, while (hk0) peaks are observed in the horizontal direction, respectively.



Unit [nm]	(110) _{horizontal}		(003) _{vertical}	
Bphen	28.0	±0.16	10.6	±0.18
TPBi	24.4	±0.26	9.4	±0.11
B3PYMPM	24.2	±0.18	8.6	±0.12

Fig. 5.8 Crystal size of 50 nm thick HATCN films grown on different organic layers. Error values are also summarized.

5.4 Conclusion

HATCN molecules were found to be stacked with a (001) preferred orientation on four different organic surfaces. For the case of the TAPC organic layer (a hydrophobic surface), the HATCN film displayed regularly arranged nano-grains. As the film thickness increased, islands formed on top of the regularly arranged nano-grains. In contrast, the HATCN seemed to be almost perfect film without forming nano-grains on ETL surface. The nano-grains and the HATCN surface morphology were not affected by the formation of a transparent IZO electrode. The transparent electrode layer was conformal on the HATCN surface, thereby preserving the surface morphology. Unfortunately, the crystalline properties of the HATCN layers under the 10 nm thick IZO layer were not measured by GIWAXS due to strong x-ray attenuation in the IZO layer; however, the crystalline properties were retained after the formation of the IZO layer because the HATCN surface was not damaged by the sputtering process. These results indicate that the (001) preferentially-oriented HATCN layer on the organic layer was very stable under IZO sputtering.

Chapter 6. Langevin and trap-assisted recombination in phosphorescent OLEDs

6.1 Introduction

Understanding of the charge carrier recombination process and the emission of photons from excitons is of great importance to OLEDs, because these properties are intimately related to the performance of these devices. Under electrical excitation in phosphorescent dye-doped OLEDs (PhOLEDs), two different recombination and emission paths are available in the emission layer (EML). The first path is the formation of excitons on the host material, followed by energy transfer to the dopant via the Förster and/or Dexter mechanisms. The other path is direct recombination on the dopant via charge carrier trapping. The former is related to bimolecular recombination, i.e. Langevin recombination,¹⁴⁹ while the latter is trap-assisted recombination.^{150,151} These two mechanisms are mutually competitive under electrical excitation in PhOLEDs and it is difficult to determine which mechanism is dominant in the devices, although the determination of the mechanism may provide a critical clue toward the realization of high performance PhOLEDs. Recently, M. Kuik *et al.* reported the recombination and emission mechanisms in polymer LEDs based on various conjugated polymers.^{152,153} The conjugated polymers contain intrinsic electron traps so that the current was governed by trap-assisted recombination, but the photons were emitted via a Langevin type emission mechanism. Unfortunately, little fundamental research has been undertaken into this issue in PhOLEDs. In many cases, phosphorescent dyes are energetically located as

hole traps within a host layer, and it has been reported that the dopant accelerates the trapping of holes so that trap-assisted recombination is dominant, resulting in an increment in the efficiency of PhOLEDs.¹⁵⁴⁻¹⁶¹ However, energy transfer from host to dopant is an important mechanism that makes a contribution to the enhancement of the efficiency in PhOLEDs that cannot be ignored.^{158,162-165} For example, recently, green PhOLEDs with an almost ideal level of efficiency in terms of the quantum efficiency (EQE), driving voltage and efficiency roll-off, with an EQE of 29.1%, a turn-on voltage of 2.4 V and EQE of over 27% at 10,000 cd/m², were reported using an exciplex forming co-host. The excellent performance of the PhOLEDs was attributed to the formation of the exciplex in the host followed by energy transfer to the dopant.^{5,23} The proposed mechanism is markedly different from the trap-assisted recombination mechanism that is prevalent in most PhOLEDs reported to date.

In the present study, the charge recombination mechanisms were clarified in two different PhOLEDs: one with the exciplex forming co-host,^{5,23} and the other with a single host, i.e., CBP.^{4,166} The charge recombination, accumulation and light emission mechanisms were analyzed using the *J-V-L* characteristics of the devices in the diffusion current region, along with transient EL and capacitance-voltage (*C-V*) measurements. The results clearly showed that excitons are predominantly generated by Langevin recombination in the exciplex forming co-host, in contrast to the trap-assisted recombination on the emitter in the CBP-based PhOLED. Also, the trapped charge density in the PhOLEDs with the co-host system was lower than that in the PhOLEDs that were based on the CBP single host. These results indicated that the exciplex forming co-host boosts the recombination of the charge carriers in the host by Langevin recombination and boosts the light emission from the emitter

through energy transfer from the host rather than by trap-assisted recombination, even in the high current region. Low charge density in the PhOLEDs in the exciplex forming host must be related to the low efficiency roll-off caused by reduced exciton-polaron quenching.¹⁶⁷⁻¹⁷⁰

6.2 Experimental

High efficiency PhOLEDs with the following structures were fabricated to investigate the charge recombination mechanisms: ITO (70 nm)/TAPC (75 nm)/4,4',4''-Tris(carbazol-9-yl)triphenylamine (TCTA) (10 nm)/TCTA:B3PYMPM:bis(2-phenylpyridine)iridium(III)-acetylacetonate [Ir(ppy)₂(acac)] (1:1 molar ratio and 8 wt.%, 30 nm)/B3PYMPM (40 nm)/LiF (0.7 nm)/Al (100 nm) (device 1), and ITO (70 nm)/MoO₃ (1 nm)/CBP (90 nm)/CBP:Ir(ppy)₂(acac) (8 wt.%, 15 nm)/TPBi (65 nm)/LiF (0.7 nm)/Al (100 nm) (device 2). The structures of the devices, the HOMO and LUMO levels, and the chemical structures of the organic materials are shown in Fig. 6.1.

All layers were thermally deposited on a pre-cleaned glass substrate patterned with ITO under a base pressure of 5×10^{-7} Torr in evaporation chambers without breaking the vacuum. The active area of both devices was 2×2 mm². At the end of the fabrication process, all devices were encapsulated with glass lids using ultraviolet (UV) curable epoxy resin in a glove box filled with nitrogen gas, and a desiccant film was also attached inside the glass lid.

The *J-V-L* characteristics of the PhOLEDs were measured using a semiconductor parameter analyzer (Keithley 237) and a spectrophotometer (Photo

Research PR-650). To determine the recombination parameter in the diffusion current region, a programmable source meter (Keithley 2400) and a Si photodiode (1835C, Newport) were also used. The time-resolved EL intensity was obtained using a pulse generator (Agilent 8114A) and a spectrometer (SpectraPro-300i) connected to a photomultiplier tube (Acton Research, PD-438). The voltage pulses that were applied to the device corresponded to a current density of 10 mA cm^{-2} with a pulse width of $100 \text{ }\mu\text{s}$, and the frequencies of $100 \sim 900 \text{ Hz}$. The detection wavelength was 520 nm , which corresponds to the peak wavelength of $\text{Ir(ppy)}_2(\text{acac})$ emission. All signals were detected and integrated more than 1,000 times using an oscilloscope (Agilent 54642A). The voltage applied to each OLED was measured over a $1 \text{ M}\Omega$ resistance that was parallel to the OLED.

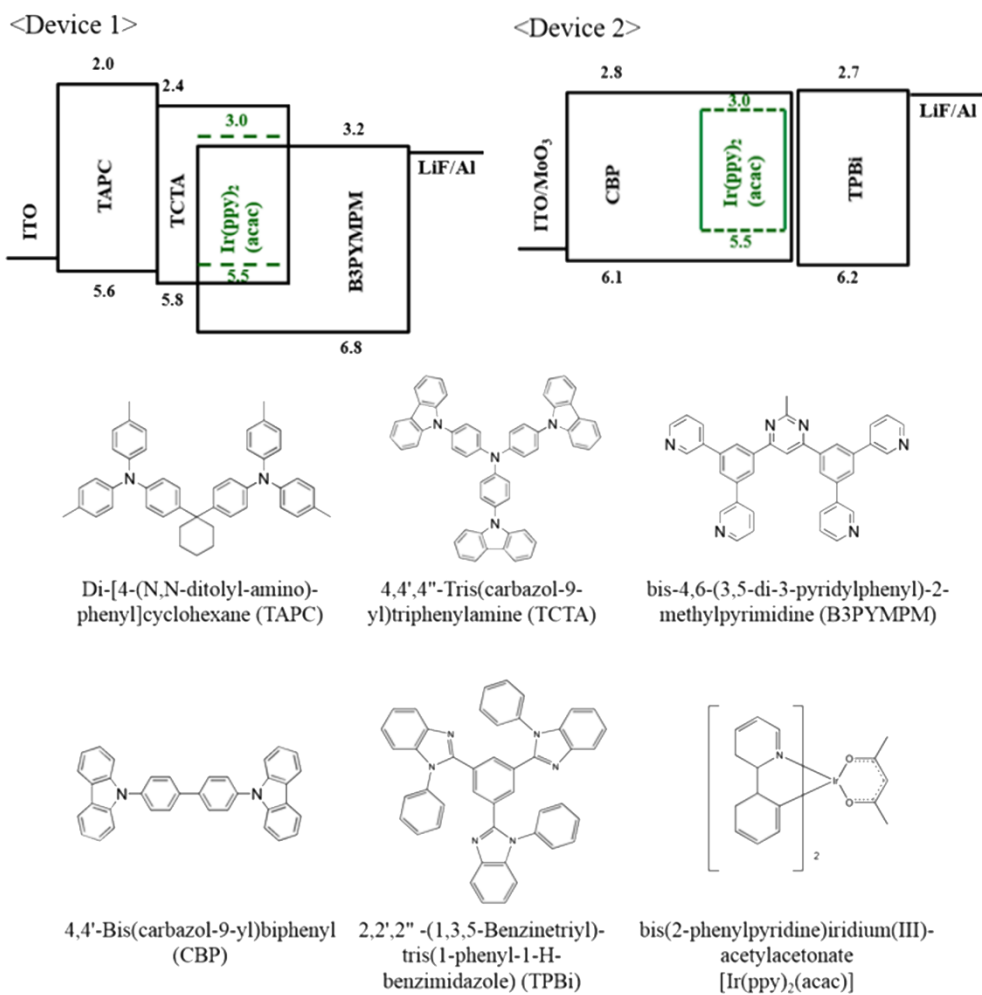


Fig. 6.1 Device structures, the energy levels of each layer, and the molecular structures of the two different PhOLEDs.

6.3 Result and Discussion

6.3.1. Device performance of the green PhOLEDs

Figure 6.2 shows the J - V - L and external quantum efficiency-luminance characteristics of the two PhOLEDs. Both PhOLEDs exhibit high efficiencies, with the maximum EQEs of 30% and 25% for device 1 and device 2, respectively. They also exhibit low efficiency roll-offs at high current densities, which correspond to 27% and 21% at 10,000 cd/m^2 in device 1 and device 2, respectively, and very low leakage currents in the low voltage region. The injection and turn-on voltages of device 1 are lower than those of device 2. The injection voltage at which the current increases abruptly is 2.0 V, and the turn-on voltage defined as the voltage at 1 cd/m^2 is 2.3 V in device 1. These values in device 1 are 0.5 V lower than those of device 2, indicating that the charges are efficiently injected from the electrodes and are transported to the emission layer under a low external bias in device 1. Another factor to be noted is that the dopant energy levels are differently located relative to the host layers. The same phosphorescent dopant, $\text{Ir}(\text{ppy})_2(\text{acac})$, was used in both PhOLEDs, but while this dopant is likely to act as both electron trap and hole trap in the CBP based PhOLED (device 2), it will only act as a hole trap in the exciplex forming co-host based PhOLED (device 1). It is expected that trap-assisted recombination will be more predominant in device 2 than in device 1. These characteristics will be analyzed and discussed based on the J - V - L , transient electroluminescence, and capacitance-voltage characteristics in the next section.

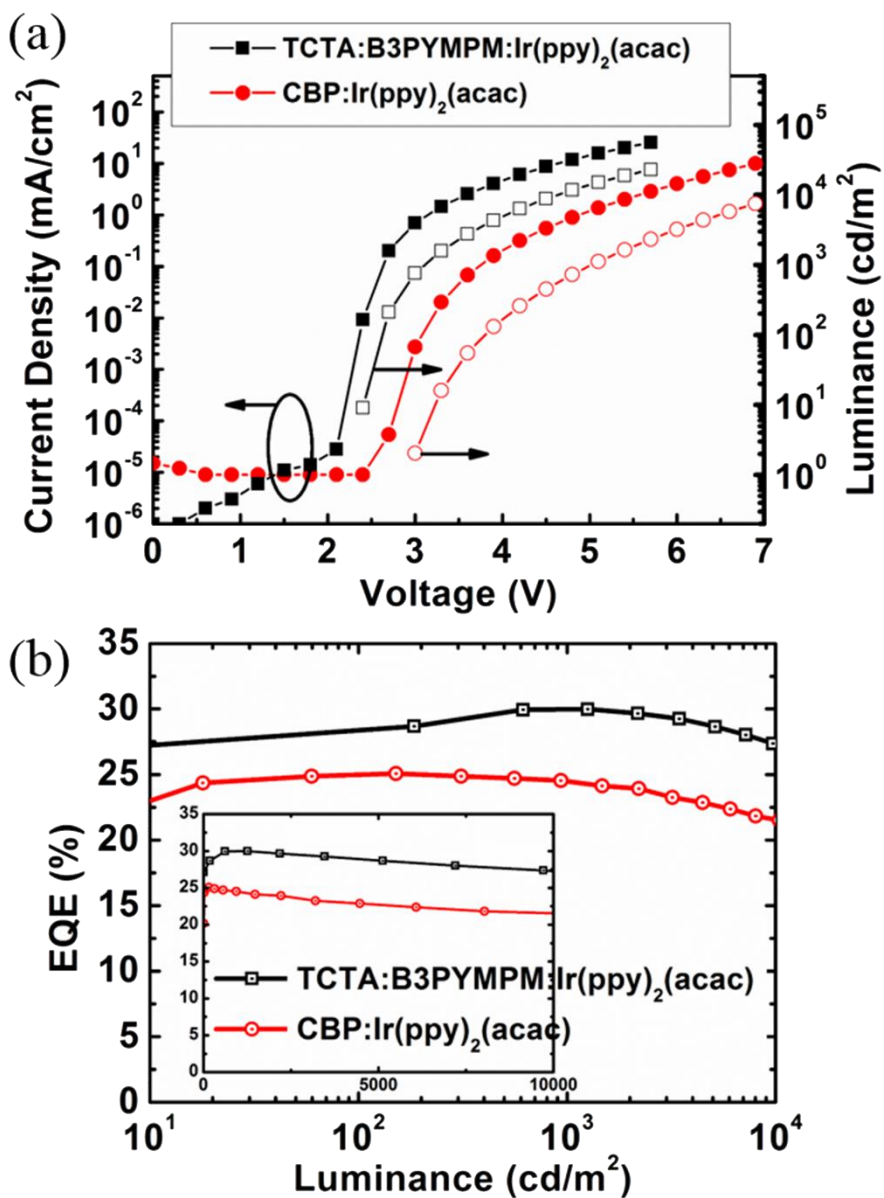


Fig. 6.2 (a) *J-V-L* characteristics and (b) (semi-log scale) EQE-luminance (η -*L*) characteristics of the TCTA:B3PYMPM:Ir(ppy)₂(acac) based PhOLED (device 1) and the CBP:Ir(ppy)₂(acac) based PhOLED (device 2). The inset of Fig. 2(b) is depicted in a linear scale.

6.3.2. Determination of the recombination type in the PhOLEDs

Formation of excitons on the host molecules by Langevin recombination and subsequent energy transfer to the dopant must compete with trap-assisted recombination in the PhOLEDs under electrical pumping, and the different mechanisms will affect the performance of the devices significantly. Bimolecular and trap-assisted recombination of the charge carriers and the emission of excitons are reflected in the J - V - L characteristics of the devices, and can be described using the Shockley diode equation in the diffusion dominated region, which is given by⁹

$$J = J_0 \left[\exp\left(\frac{qV}{\eta kT}\right) - 1 \right], \quad (1)$$

where J_0 denotes the saturation current density, k is the Boltzmann constant, T is the temperature, and q is the unit charge. The recombination parameter (η) in equation (1) is directly connected to the density of the recombination center, and varies from 1 to 2 depending on the recombination mechanism, with 1 for Langevin recombination and 2 for trap-assisted recombination. This parameter can therefore be used to investigate the major recombination and emission mechanisms in PhOLEDs under electrical excitation.^{152,153,171,172} The J - V - L characteristics of devices 1 and 2 in the diffusion current region are shown in Fig. 6.3(a). It is interesting to note that the currents flowed when $V < V_{bi}$ (the built-in potential that corresponds to the flat band condition of the device) because of the diffusion current from the metal reservoir to the organic layer. As a result, the voltages where the currents begin to rise abruptly are 2.0 V and 2.5 V in device 1 and device 2, respectively, and the turn-

on voltages where light emission begins to rise are 2.05 V and 2.6 V in device 1 and device 2, respectively. The voltage gaps between injection voltage and turn-on voltage are just 0.05 V and 0.1 V in device 1 and device 2, respectively, because there is a low energy barrier for charge transport inside the devices. Interestingly, the turn-on voltage of 2.05 V in device 1 is much lower than the voltage that corresponds to the emitted photon energy ($V = h\nu / q$) of 2.4 eV of the phosphorescent dopant, Ir(ppy)₂(acac), and this is attributed to the device diffusion current. The recombination parameters of the devices were extracted using equation (2), and the results are depicted in Fig. 6.3(b).

$$\eta = \left(\frac{kT}{q} \frac{\partial \ln J}{\partial V} \right)^{-1}. \quad (2)$$

The η value of device 2 approaches 2 in the plateau of the curve, indicating that trap-assisted recombination is dominant in the system. In contrast, the η value is approximately 1.4 in device 1, indicating the dominance of Langevin recombination in the device. This Langevin recombination dominance indicates that the electron-hole recombination occurs predominantly in the host molecules in device 1; i.e., the formation of the exciplex. Although the dopant is energetically located at a hole trap in the device 1 host, the exciplex forming co-host stimulates exciplex formation in the host, and subsequent energy transfer from the exciplex to the dopant rather than by trap-assisted recombination on dopant molecules, as observed in device 2.

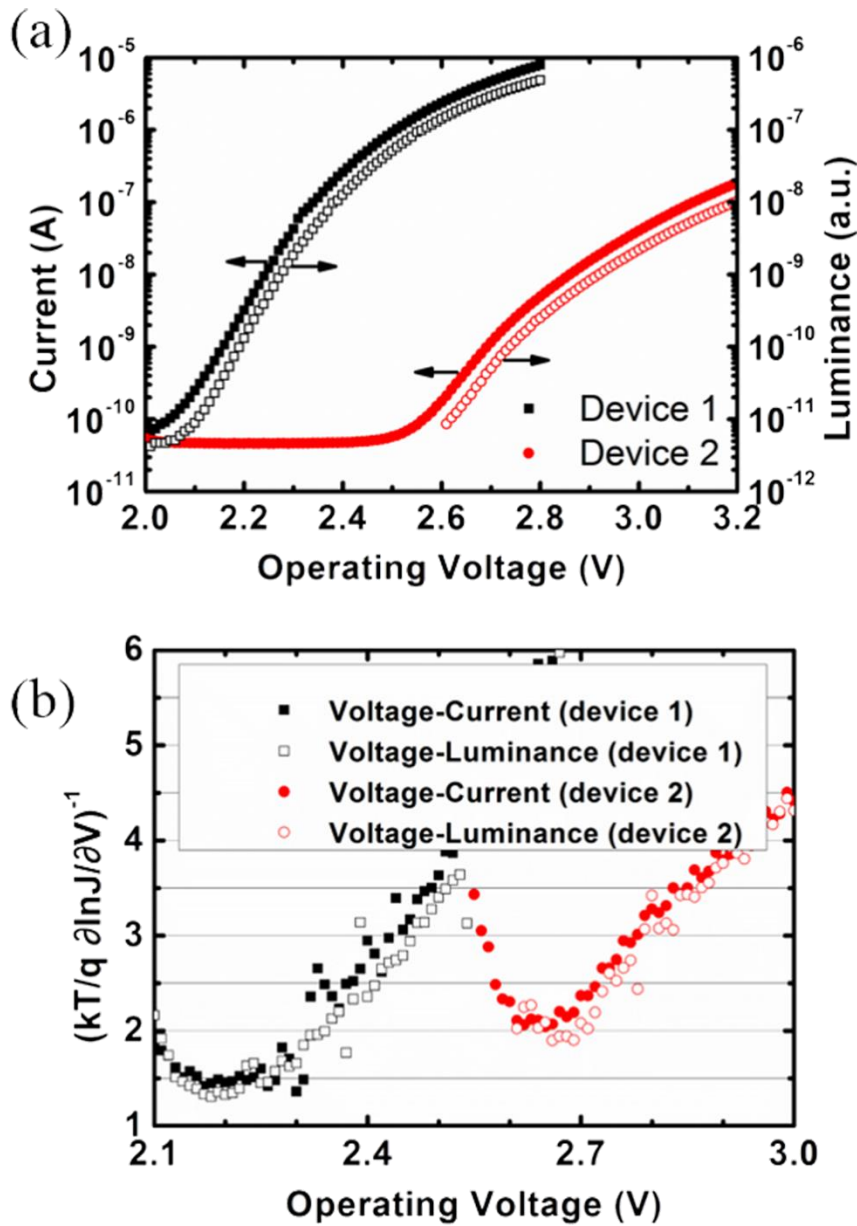


Fig. 6.3 (a) J - V - L characteristics of the two PhOLEDs in diffusion dominated current region. (b) The recombination parameter (η) was calculated from Fig. 6.3(a) by using equation (2).

6.3.3. Time resolved electroluminescence

The recombination characteristics were also analyzed based on the results of the transient EL measurements. Figure 6.4 shows the normalized time resolved EL characteristics of the devices. The voltage pulse width was 100 μs , and the pulse was periodically applied to the devices with a frequency of 100 Hz. The voltage pulse height corresponds to a current density of 10 mA/cm^2 . The magnitude of the reverse bias after the voltage turn-off was varied up to saturation, as shown in Fig. 6.4. Device 1 showed no difference in the turn-on region and was independent of the magnitude of the reverse bias applied after the pulse turn-off (Fig. 6.4a). In contrast, device 2 showed an initial overshoot in the turn-on region. The overshoot was reduced and the rise time was increased as the reverse bias magnitude increased to -5 V , as shown in Fig. 6.4b. The dependence of the overshoot and the rise time on the reverse bias magnitude after the turn-off in device 2 indicates that residual trapped charges exist after the voltage pulse turn-off for at least 10 μs , until the next pulse is applied. A reverse bias of more than -5 V was required to sweep out the trapped charges in device 2 during the off-time. The luminance overshoot must be related to the recombination of the trapped charges and to the recombination of the injected charges.¹⁷³⁻¹⁷⁵

Further evidence of the existence of trapped charges can be obtained from the frequency dependent behavior of the transient EL, as shown in Fig. 6.5. The rise time becomes shorter as the frequency increases in device 2. In contrast, there is no change in the rise time with increasing frequency in device 1. When the excitation pulse frequency increases from 100 to 900 Hz, the number of trapped charges in the

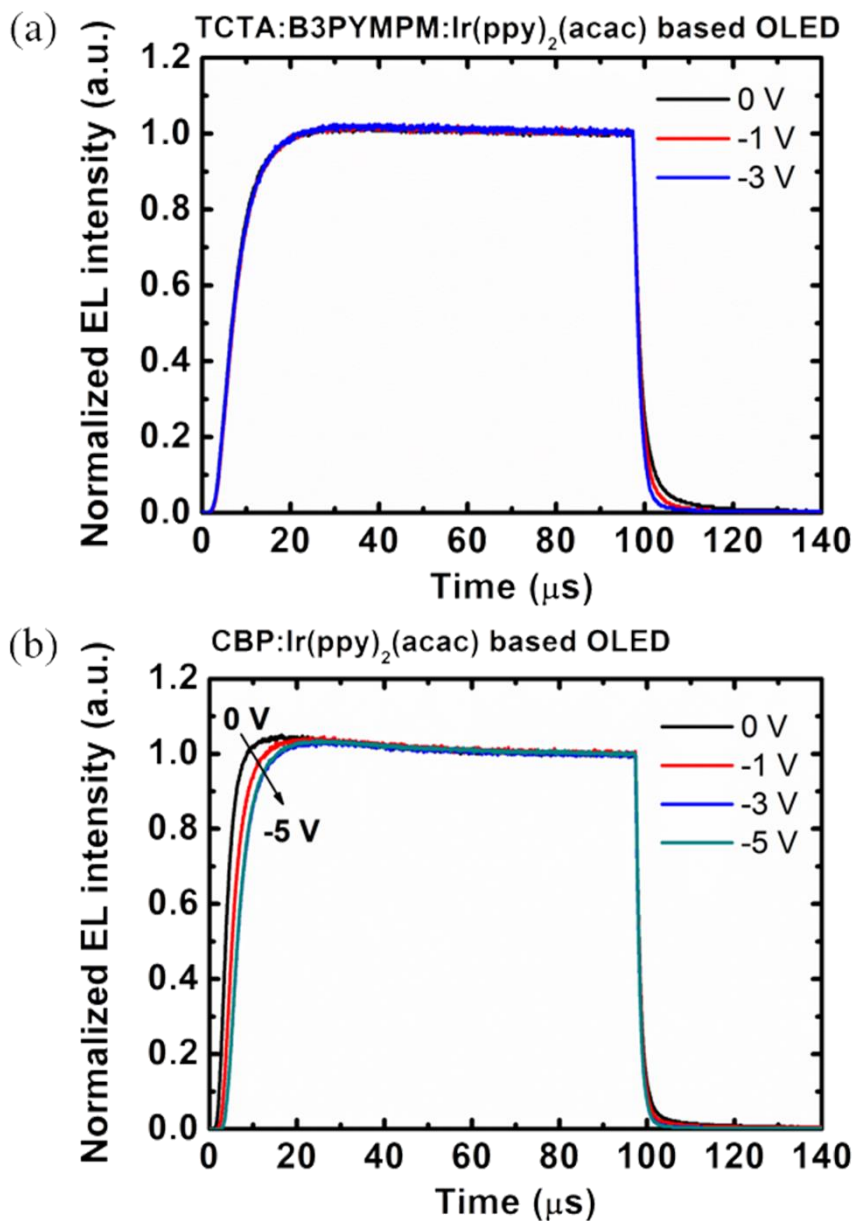


Fig. 6.4 Normalized intensity of transient EL, depending on the reverse bias after turn-off of the voltage pulse in (a) device 1 and (b) device 2. The voltage pulse width was 100 μs and the pulse frequency was 100 Hz. The voltage pulse height corresponds to a current density of 10 mA/cm². The magnitude of the reverse bias after the voltage turn-off was gradually increased up to saturation. The initial overshoots caused by the trapped charges in the emission layer are observed only in device 2, and they gradually decrease as the reverse bias magnitude increases.

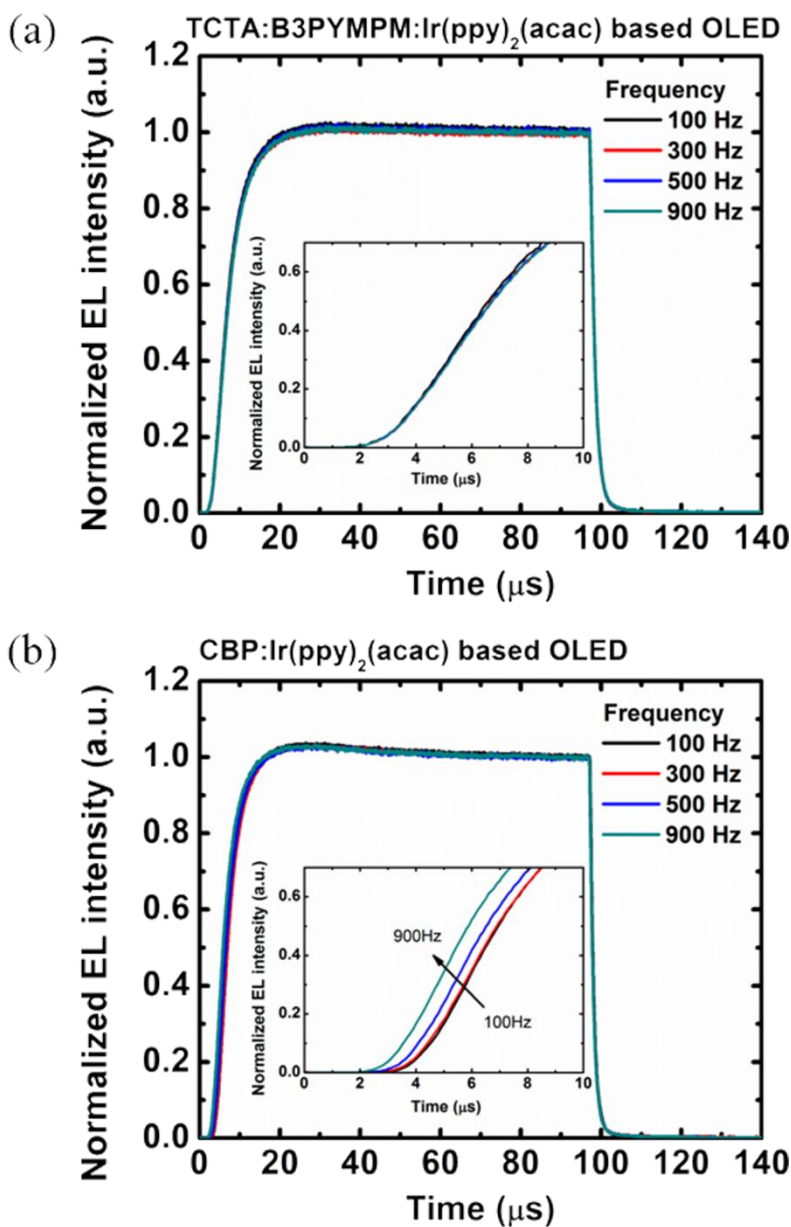


Fig. 6.5 Normalized transient EL intensity depending on the frequency of the voltage pulse in (a) device 1, and (b) device 2. The voltage pulse width was 100 μs and the voltage pulse height corresponds to a current density of 10 mA/cm². The frequency of the voltage pulse was gradually increased from 100 Hz to 900 Hz. The initial part of the transient EL was magnified, as shown in the inset. The initial overshoots are still observed and the luminance onset time gradually increases as the frequency increases in device 2. In contrast, there are no changes in device 1 that depend on variation of the frequency.

EML increases because the trapped charge relaxation time is fixed within the device. As a result, the luminance onset time becomes faster because of the increased numbers of remaining charges as the pulse frequency increases. This phenomenon occurs only in device 2, and not in device 1, supporting the dominance of trap-assisted recombination in device 2 and the dominance of bimolecular Langevin recombination in device 1. The frequency dependence of the transient EL shows a clear difference between a trap-assisted recombination dominant device and a Langevin recombination dominant device.

Both the initial overshoot in the transient EL and the transient overshoot or spike at the decay part of the transient EL have been studied to investigate charge trapping in the small molecule based PhOLEDs, and the results are shown in Fig. 6.6. The spike after the voltage turn-off was attributed to recombination of the trapped charges on the dopant state in the EML.^{160,161} Although there are no remarkable overshoots in the turn-off region, the luminance decay behavior differed between the two PhOLEDs. As with our previous study,⁵ the slow luminance decay up to 350 ns after the voltage pulse turn-off showed independence from the magnitude of the reverse bias voltage in device 1 (Fig. 6.6a). The initially prolonged luminance of up to 350 ns, independent of the reverse bias, is attributed to energy transfer from the neutral host excitons to the dopant, followed by emission from the dopant. Similar behavior was also observed in device 2 (Fig. 6.6b), but the initially prolonged time of the luminance was 140 ns and this value is less than half of that of device 1.

Based on the J - V - L and transient EL behavior of these devices, it can be concluded that Langevin recombination is dominant over trap-assisted

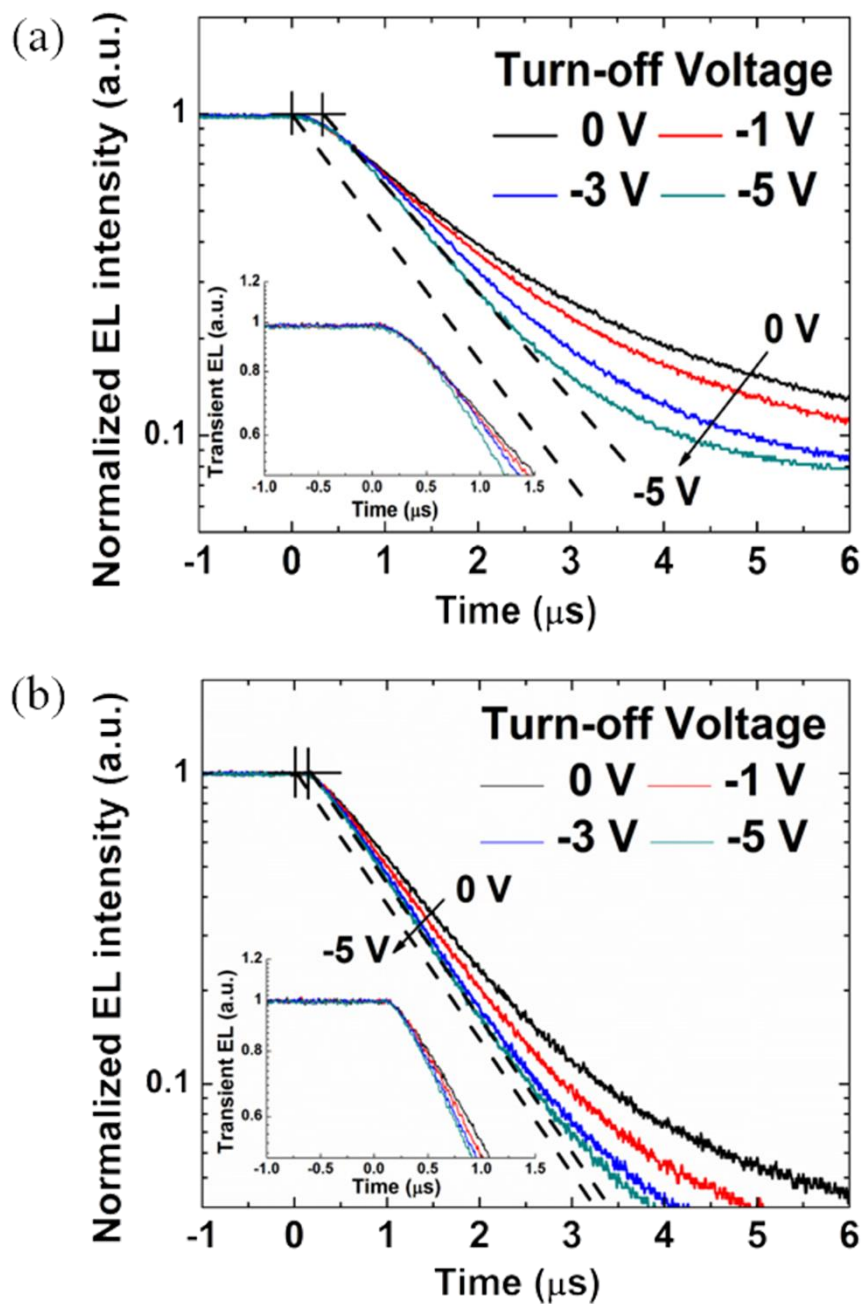


Fig. 6.6 Normalized intensity of the transient EL at the decay part, depending on the reverse bias of the voltage pulse after turn-off in (a) device 1, and (b) device 2.

recombination in device 1 with its small number of trapped charges. In contrast, trap-assisted recombination is predominant in device 2 because of its large number of trapped charges.

6.3.4. Analysis of trapped charges from C-V measurements

The trapped charge behavior was also analyzed from the viewpoint of the device capacitance-voltage (C - V) characteristics, as shown in Fig. 6.7, where the J - V curves have been added for comparison. The capacitance behavior of the two devices showed significant differences. The capacitance of device 1 shows a small peak. This peak starts to increase at approximately 2 V, corresponding to the injection voltage, and reaches a maximum at 2.4 V, followed by a reduction to ground level at around 2.8 V. The existence of the peak in the C - V curve indicates the accumulation of the charges inside the device, and these accumulated charges disappear at 2.8 V. The energy diagram shown in Fig. 1 and the J - V curve of device 1 suggest that some of the diffused charges begin to accumulate at the TAPC/TCTA junction and this accumulation increases up to 2.4 V, which might correspond to the flat band condition. Above that voltage, injection by thermionic emission at the junction becomes efficient for reduction of the accumulated charges. Above 2.8 V, the TAPC/TCTA junction does not behave like an injection barrier any more, which is probably because of the energy barrier lowering effect. Increasing the injected current at voltages above 2.8 V gradually increases the capacitance because of the existence of locally unbalanced electron and hole densities.

In contrast, device 2 showed a much higher peak in the C - V curve at a higher voltage than device 1. The capacitance began to slowly rise at 2.5 V up to 3.1 V because of the contribution of the diffusion current, and then increased sharply to a maximum value at 5.4 V. Referring again to the energy diagram shown in Fig. 1, the capacitance must arise from the accumulated charges on the dopant molecules,

because there are no organic junctions for the injected holes to reach the EML and the energy barrier between TPBi and CBP for the injected electrons to reach the EML is only 0.1 eV. The accumulated charges might be holes, because the hole mobility of the CBP layer ($\sim 10^{-3}$ cm²/Vs) is two orders of magnitude higher than the electron mobility of the TPBi layer. In addition, the Poole-Frankel constant (β) of the TPBi layer is more than three times higher than that of the CBP layer, indicating that the electron transport in this device is more sensitive to the external field. Therefore, it can be inferred that the hole currents are dominant over the electron currents to an extent that the extra holes are accumulated in the EML, particularly on the dopant molecules, during light emission at up to 5.4 V. As the bias then increases to more than 5.4 V, the accumulated holes are rapidly annihilated by recombination with the injected electrons at the high bias, because of the increased mobility from the high β value. The *C-V* characteristics in device 2 are similar to the characteristics that were previously reported when using bilayer structured OLEDs.¹⁷⁶⁻¹⁷⁸

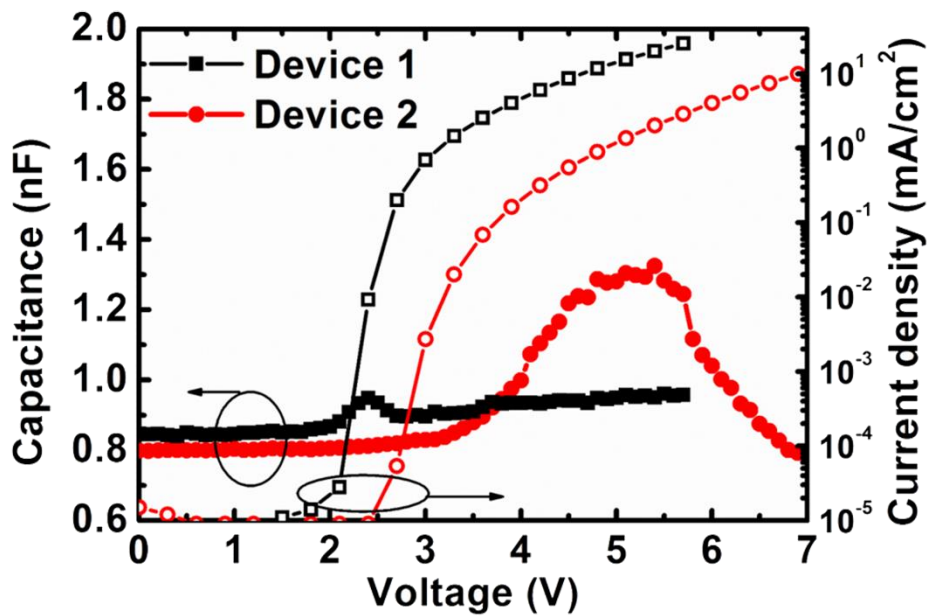


Fig. 6.7 Capacitance-voltage (C-V) plots and current density-voltage curves for the two different PhOLEDs.

6.4 Conclusion

In summary, the J - V characteristics in the diffusion current region and the transient EL and C - V measurements clearly demonstrated that the Langevin recombination and energy transfer process are dominant over trap-assisted recombination in the green PhOLED with the exciplex forming co-host system. The exciplex forming system can be considered to be a quasi-host that has its HOMO and LUMO levels as the HOMO of the hole transport material (donor) and the LUMO of the electron transport material (acceptor). In addition, its triplet energy level is almost the same as that of the singlet, meaning that a quasi-host is able to be selected such that its HOMO – LUMO gap is very close to the phosphorescent dopant. In that way, the trap energy of the dopant can be minimized, easing the Langevin recombination process, as in the case of this study of the exciplex forming host. The low polaron density combined with the efficient energy transfer from exciplex to dopant results in a low efficiency roll-off in the device. In contrast, single host systems generally have a large singlet-triplet energy gap, such that a host with a large HOMO – LUMO gap must have a higher triplet energy than the triplet gap of the phosphorescent dopant. Therefore, single host systems generally have high trap energies, which results in the dominance of trap-assisted recombination in the PhOLEDs.

Chapter 7. Summary and Outlook

During the last decades, OLEDs have been rapidly developed and already commercialized in the small sized display such as digital camera, MP3, and mobile phone, as well as in the large sized 55-inch TVs in 2013. In addition, small sized flexible devices are ready to be commercialized in the near future. To realize a high performance flexible OLEDs, high quality of substrate, TFTs, OLEDs, and encapsulation technologies have to be combined with each other. The barrier coated plastic, oxide TFTs, inverted OLEDs, and thin film encapsulation methods are the promising candidates for the purposes, because these are suitable for low permeability, low processing temperature, and simple device structures with high performance.

This thesis has described what the issues exist, how to improve the efficiency and how to realize the ultimate efficiency in the inverted OLEDs for highly efficient flexible or transparent devices. Requirements for the high quality OLEDs are low driving and turn-on voltage, high EQE, and low efficiency roll-off, and these factors were achieved by using the following methods. Management of the charge injection characteristics by doping technology leads to a good charge balance, $\gamma = 1$. Use of the exciplex host, TCTA:B3PYMPM, and energy transfer to phosphorescent dye, Ir(ppy)₂(acac), leads to efficient light harvest, $\eta_{ST} = 1$, and reduce the TTA due to broad distribution of the excitons. In addition, it results in the reduction of the residual charges attributing to Langevin recombination dominance, and low driving voltage of the device due to low energy barriers at the interfaces and efficient energy

transfer mechanism in the EML with the exciplex forming co-host. Based on the above methods, 29.1% of the max. EQE and 27.8% of the EQE at 10,000 cd m^{-2} in the conventional OLED and 23.6% of the max. EQE and 21.0% of the EQE at 10,000 cd m^{-2} in the inverted top emitting OLEDs, respectively, were realized. All the devices showed low turn-on voltage of 2.4 V at 1 cd m^{-2} . The lower efficiency in the iOLED than in the conventional OLED is attributed to low electrical charge balance so that it can be optimized further and in progress now. In addition, a highly efficient transparent iOLED was realized by using a very efficient organic buffer layer, 1, 4, 5, 8, 9, 11-hexaazatriphenylene-hexacarbonitrile (HATCN).

It is interesting to note that the energy level of the exciplex forming hosts are easily adjusted and selected without synthesizing new materials to achieve an efficient charge transfer to specific dopants having different band gaps, because there are already a lot of synthesized organic materials in this field. Thus, what researchers have to do is a selection of proper material and check the formation of the exciplex and efficient energy transfer from host to dopant under photo- or electric-excitation. Of course, if the fundamental mechanism for the system is precisely understood, the efforts are significantly reduced. It is also required to focus on the development of the horizontally oriented emitters with high quantum efficiency for further enhancement of the EQE over 40% in the iOLEDs, because a phosphorescent emitter with a horizontal orientation and a high PL quantum efficiency influences on the EQE under micro-cavity environments. Practically, a horizontally oriented emitter with $q_{\text{PL}} = 0.95$ and $\Theta = 0.95$ are required for 40% of EQE in the ideally operated PhOLEDs, and theoretically 46% of EQE can be achievable using an emitter with

$q_{PL} = 1$ and $\Theta = 1$. Finally, over 90% of EQE is able to be realized by using the transparent iOLEDs combined with the above factors and additional out-coupling structures, because the negligible SP loss are exist in the transparent iOLEDs having both transparent electrodes, instead of the metal electrodes.

Over 200 lm W^{-1} of power efficiency is realizable in white OLEDs when the above factors are ideally combined, and it has been actively under investigation. Moreover, the white OLEDs will remarkably contribute to the highly efficient flexible devices for display and lighting devices beyond the previous light sources.

Bibliography

1. C. Tang and S. VanSlyke, *Appl. Phys. Lett.* 51, 913 (1987).
2. M. Baldo, D. O'brien, Y. You, A. Shoustikov, S. Sibley, M. Thompson and S. Forrest, *Nature* 395, 151 (1998).
3. D. Tanaka, H. Sasabe, Y.-J. Li, S.-J. Su, T. Takeda and J. Kido, *Jpn. J. Appl. Phys.* 46, L10 (2007).
4. M. Helander, Z. Wang, J. Qiu, M. Greiner, D. Puzzo, Z. Liu and Z. Lu, *Science* 332, 944 (2011).
5. Y.-S. Park, S. Lee, K.-H. Kim, S.-Y. Kim, J.-H. Lee and J.-J. Kim, *Adv. Funct. Mater.* 23, 4914 (2013).
6. K. Goushi, K. Yoshida, K. Sato and C. Adachi, *Nature Photonics* 6, 253 (2012).
7. D. Baigent, R. Marks, N. Greenham, R. Friend, S. Moratti and A. Holmes, *Appl. Phys. Lett.* 65, 2636 (1994).
8. V. Bulovic, G. Gu, P. Burrows, S. Forrest and M. Thompson, *Nature* 380, 29 (1996).
9. W. Shockley, *Bell Syst. Tech. J* 28, 435 (1949).
10. M. A. Lampert and P. Mark, *Current Injection in Solids* (Academic, New York, 1970).
11. T. Tsutsui, E. Aminaka, C. Lin and D.-U. Kim, *Phil. Trans. R. Soc. A* 355, 801 (1997).
12. J.-S. Kim, P. K. Ho, N. C. Greenham and R. H. Friend, *J. Appl. Phys.* 88, 1073 (2000).
13. H.-W. Lin, C.-L. Lin, H.-H. Chang, Y.-T. Lin, C.-C. Wu, Y.-M. Chen, R.-T. Chen, Y.-Y. Chien and K.-T. Wong, *J. Appl. Phys.* 95, 881 (2004).

14. D. Yokoyama, A. Sakaguchi, M. Suzuki and C. Adachi, *Appl. Phys. Lett.* 93, 173302 (2008).
15. S. Nowy, J. Frischeisen and W. Brütting, presented at the SPIE Photonic Devices+ Applications, 2009 (unpublished).
16. D. Yokoyama, A. Sakaguchi, M. Suzuki and C. Adachi, *Org. Electron.* 10, 127 (2009).
17. J. Frischeisen, D. Yokoyama, C. Adachi and W. Brütting, *Appl. Phys. Lett.* 96, 073302 (2010).
18. D. Yokoyama, Y. Setoguchi, A. Sakaguchi, M. Suzuki and C. Adachi, *Adv. Funct. Mater.* 20, 386 (2010).
19. M. Flämmich, J. Frischeisen, D. S. Setz, D. Michaelis, B. C. Krummacher, T. D. Schmidt, W. Brütting and N. Danz, *Org. Electron.* 12, 1663 (2011).
20. T. D. Schmidt, D. S. Setz, M. Flammich, J. Frischeisen, D. Michaelis, B. C. Krummacher, N. Danz and W. Brütting, *Appl. Phys. Lett.* 99, 163302 (2011).
21. P. Liehm, C. Murawski, M. Furno, B. Lüssem, K. Leo and M. C. Gather, *Appl. Phys. Lett.* 101, 253304 (2012).
22. L. Penninck, F. Steinbacher, R. Krause and K. Neyts, *Org. Electron.* 13, 3079 (2012).
23. S.-Y. Kim, W. I. Jeong, C. Mayr, Y.-S. Park, K.-H. Kim, J.-H. Lee, C.-K. Moon, W. Brütting and J.-J. Kim, *Adv. Funct. Mater.* 23, 3896 (2013).
24. M. Furno, R. Meerheim, S. Hofmann, B. Lüssem and K. Leo, *Phys. Rev. B* 85, 115205 (2012).
25. W. Brütting, J. Frischeisen, T. D. Schmidt, B. J. Scholz and C. Mayr, *Phys. Status Solidi (a)* 210, 44 (2013).

26. D. L. Dexter, *J. Chem. Phys.* 21, 836 (1953).
27. T. Förster, *Discuss. Faraday Soc.* 7, 27 (1959).
28. K. Nomura, H. Ohta, A. Takagi, T. Kamiya, M. Hirano and H. Hosono, *Nature* 432, 488 (2004).
29. J.-S. Park, T.-W. Kim, D. Stryakhilev, J.-S. Lee, S.-G. An, Y.-S. Pyo, D.-B. Lee, Y. G. Mo, D.-U. Jin and H. K. Chung, *Appl. Phys. Lett.* 95, 013503 (2009).
30. W. S. Wong and A. Salleo, *Flexible electronics: materials and applications* (Springer, 2009).
31. <http://www.idtechex.com/research/reports/metal-oxide-tft-backplanes-for-displays-2013-2018-analysis-trends-forecasts-000334.asp?viewopt=desc>
32. C.-C. Wu, C.-W. Chen, C.-L. Lin and C.-J. Yang, *J. Display Technol.* 1, 248 (2005).
33. H. H. Hsieh, T. T. Tsai, C. Y. Chang, H. H. Wang, J. Y. Huang, S. F. Hsu, Y. C. Wu, T. C. Tsai, C. S. Chuang and L. H. Chang, presented at the SID Symposium Digest of Technical Papers, 2010 (unpublished).
34. T. Kamiya, K. Nomura and H. Hosono, *Science and Technology of Adv. Mater.* 11, 044305 (2010).
35. Y. G. Mo, M. Kim, C. K. Kang, J. H. Jeong, Y. S. Park, C. G. Choi, H. D. Kim and S. S. Kim, presented at the SID Symposium Digest of Technical Papers, 2010 (unpublished).
36. T. Tanabe, S. Amano, H. Miyake, A. Suzuki, R. Komatsu, J. Koyama, S. Yamazaki, K. Okazaki, M. Katayama and H. Matsukizono, presented at the SID Symposium Digest of Technical Papers, 2012 (unpublished).

37. J.-H. Lee, P.-S. Wang, H.-D. Park, C.-I. Wu and J.-J. Kim, *Org. Electron.* 12, 1763 (2011).
38. H. Heil, J. Steiger, S. Karg, M. Gastel, H. Ortner, H. Von Seggern and M. Stobel, *J. Appl. Phys.* 89, 420 (2001).
39. I. D. Parker, *J. Appl. Phys.* 75, 1656 (1994).
40. M. Stossel, J. Staudigel, F. Steuber, J. Simmerer and A. Winnacker, *Appl. Phys. a-Mater.* 68, 387 (1999).
41. R. Murayama, S. Kawami, T. Wakimoto, H. Sato, H. Nakada, T. Namiki, K. Imai and M. Nomura, presented at the Jpn. Soc. Appl. Phys., Extended Abstracts (54th Autumn Meeting, 1993), 1993 (unpublished).
42. E. I. Haskal, A. Curioni, P. F. Seidler and W. Andreoni, *Appl. Phys. Lett.* 71, 1151 (1997).
43. J. Kido and T. Matsumoto, *Appl. Phys. Lett.* 73, 2866 (1998).
44. T. Oyamada, H. Sasabe, C. Adachi, S. Murase, T. Tominaga and C. Maeda, *Appl. Phys. Lett.* 86, 033503 (2005).
45. T. Hasegawa, S. Miura, T. Moriyama, T. Kimura, I. Takaya, Y. Osato and H. Mizutani, presented at the SID Symposium Digest of Technical Papers, 2004 (unpublished).
46. C.-I. Wu, C.-T. Lin, Y.-H. Chen, M.-H. Chen, Y.-J. Lu and C.-C. Wu, *Appl. Phys. Lett.* 88, 152104 (2006).
47. D.-S. Leem, S.-Y. Kim, J.-J. Kim, M.-H. Chen and C.-I. Wu, *Electrochem. Solid-State Lett.* 12, J8 (2009).
48. J. Huang, Z. Xu and Y. Yang, *Adv. Funct. Mater.* 17, 1966 (2007).
49. M.-H. Chen and C.-I. Wu, *J. Appl. Phys.* 104, 113713 (2008).

50. M.-H. Chen, Y.-H. Chen, C.-T. Lin, G.-R. Lee, C.-I. Wu, D.-S. Leem, J.-J. Kim and T.-W. Pi, *J. Appl. Phys.* 105, 113714 (2009).
51. M.-H. Chen, Y.-J. Lu, Y.-J. Chang, C.-C. Wu and C.-I. Wu, *Electrochem. Solid-State Lett.* 13, H203 (2010).
52. K. Walzer, B. Maennig, M. Pfeiffer and K. Leo, *Chem. Rev.* 107, 1233 (2007).
53. J.-H. Lee, D.-S. Leem, H.-J. Kim and J.-J. Kim, *Appl. Phys. Lett.* 94, 123306 (2009).
54. J.-H. Lee, H.-M. Kim, K.-B. Kim, R. Kabe, P. Anzenbacher and J.-J. Kim, *Appl. Phys. Lett.* 98, 173303 (2011).
55. J. -H. Lee and J. -J. Kim, *Phys. Status Solidi A* 209, 1399 (2012).
56. W. Gao and A. Kahn, *Appl. Phys. Lett.* 79, 4040 (2001).
57. G. Parthasarathy, C. Shen, A. Kahn and S. Forrest, *J. Appl. Phys.* 89, 4986 (2001).
58. X. Zhou, M. Pfeiffer, J. Huang, J. Blochwitz-Nimoth, D. Qin, A. Werner, J. Drechsel, B. Maennig and K. Leo, *Appl. Phys. Lett.* 81, 922 (2002).
59. X. Zhou, J. Blochwitz-Nimoth, M. Pfeiffer, B. Maennig, J. Drechsel, A. Werner and K. Leo, *Synt. Met.* 138, 193 (2003).
60. C.-W. Chen, C.-L. Lin and C.-C. Wu, *Appl. Phys. Lett.* 85, 2469 (2004).
61. S.-Y. Chen, T.-Y. Chu, J.-F. Chen, C.-Y. Su and C. H. Chen, *Appl. Phys. Lett.* 89, 053518 (2006).
62. T.-Y. Chu, J.-F. Chen, S.-Y. Chen, C.-J. Chen and C. H. Chen, *Appl. Phys. Lett.* 89, 053503 (2006).
63. J. Meyer, P. Görrn, S. Hamwi, H.-H. Johannes, T. Riedl and W. Kowalsky, *Appl. Phys. Lett.* 93, 073308 (2008).
64. W. Gao and A. Kahn, *J. Phys.: Condens. Matter* 15, S2757 (2003).

65. W. Gao and A. Kahn, *Appl. Phys. Lett.* 82, 4815 (2003).
66. A. Kahn, W. Zhao, W. Gao, H. Vázquez and F. Flores, *Chem. Phys.* 325, 129 (2006).
67. T.-Y. Chu, S.-Y. Chen, J.-F. Chen and C. H. Chen, *Jpn. J. Appl. Phys.* 45, 4948 (2006).
68. F. Wang, T. Xiong, X. Qiao and D. Ma, *Org. Electron.* 10, 266 (2009).
69. P.-S. Wang, I.-W. Wu, and C.-I. Wu, *J. Appl. Phys.* 108, 103714 (2010).
70. C. Yun, H. Cho, H. Kang, Y. M. Lee, Y. Park, and S. Yoo, *Appl. Phys. Lett.* 95, 053301 (2009).
71. J. Hou, J. Wu, Z. Xie, and L. Wang, *Appl. Phys. Lett.* 95, 203508 (2009).
72. H. Choi, S. Kim, W. Kim, K. Hong, and J. Lee, *J. Appl. Phys.* 100, 064106 (2006).
73. H. Lee, I. Park, J. Kwak, D. Y. Yoon, and C. Lee, *Appl. Phys. Lett.* 96, 153306 (2010).
74. S. Y. Ryu, C. H. Lee, I. S. Oh, S. Y. Song, K. H. Hwang, H. S. Hwang, M. H. Han, B. H. Hwang, H. K. Baik, Y. S. Kim, and J. Y. Lee, *Electrochem. Solid-State Lett.* 13, J43 (2010).
75. Q. Wang, Z. Deng, and D. Ma, *Opt. Express* 17, 17269 (2009).
76. M. Thomschke, S. Hofmann, S. Olthof, M. Anderson, H. Kleemann, M. Schober, B. Lüsse, and K. Leo, *Appl. Phys. Lett.* 98, 083304 (2011).
77. S. Braun, M. P. de Jong, W. Osikowicz, and W. R. Salaneck, *Appl. Phys. Lett.* 91, 202108 (2007).
78. D.-S. Leem, H.-D. Park, J.-W. Kang, J.-H. Lee, J. W. Kim, and J.-J. Kim, *Appl. Phys. Lett.* 91, 011113 (2007).
79. J.-H. Lee, D.-S. Leem, and J.-J. Kim, *Org. Electron.* 11, 486 (2010).

80. C.-I. Wu, G. -R. Lee, and T. -W. Pi, *Appl. Phys. Lett.*, 87, 212108 (2005).
81. M. Y. Chan, S. L. Lai, K. M. Lau, C. S. Lee, and S. T. Lee, *Appl. Phys. Lett.* 89, 163515 (2006).
82. D.-S. Leem, S. O. Jung, S.-O. Kim, J. -W. Park, J. W. Kim, Y. -S. Park, Y.-H. Kim, S.-K. Kwon and J.-J. Kim, *J. Mater. Chem.* 19, 8824 (2009).
83. Z.Q. Gao, C.S. Lee, I. Bello and S.T. Lee, *Appl. Phys. Lett.* 74, 865 (1999).
84. Y.-S. Park, W.-I. Jeong and J.-J. Kim, *J. Appl. Phys.* 110, 124519 (2011).
85. L. Xiao, Z. Chen, B. Qu, J. Luo, S. Kong, Q. Gong and J. Kido, *Adv. Mater.* 23, 926 (2011).
86. H. Ishii, K. Sugiyama, E. Ito and K. Seki, *Adv. Mater.* 11, 972 (1999).
87. S. Tsang, Z. Lu and Y. Tao, *Appl. Phys. Lett.* 90, 132115 (2007).
88. S. Braun, W. R. Salaneck and M. Fahlman, *Adv. Mater.* 21, 1450 (2009).
89. W. Chen, D. Qi, X. Gao and A. T. S. Wee, *Prog. Surf. Sci.* 84, 279 (2009).
90. N. Koch, S. Duhm, J. P. Rabe, A. Vollmer and R. L. Johnson, *Phys. Rev. Lett.* 95, 237601 (2005).
91. H. Kanno, R. J. Holmes, Y. Sun, S. Kena Cohen and S. R. Forrest, *Adv. Mater.* 18, 339 (2006).
92. M. Y. Chan, S. L. Lai, K. M. Lau, M. K. Fung, C. S. Lee and S. T. Lee, *Adv. Funct. Mater.* 17, 2509 (2007).
93. P. Destruel, H. Bock, I. Seguy, P. Jolinat, M. Oukachmih and E. Bedel Pereira, *Polym. Int.* 55, 601 (2006).
94. K. Fehse, S. Olthof, K. Walzer, K. Leo, R. L. Johnson, H. Glowatzki, B. Broker and N. Koch, *J. Appl. Phys.* 102, 073719 (2007).

95. T. Chiba, K. Nakayama, Y. J. Pu, T. Nishina, M. Yokoyama and J. Kido, *Chem. Phys. Lett.* 502, 118 (2011).
96. D.-S. Leem, S.-Y. Kim, J.-H. Lee and J.-J. Kim, *J. Appl. Phys.* 106, 063114 (2009).
97. C. Y. Wu, M. H. Ho, S. Y. Su and C. H. Chen, *J. Soc. Inf. Display.* 18, 76 (2010).
98. C. Falkenberg, S. Olthof, R. Rieger, M. Baumgarten, K. Muellen, K. Leo and M. Riede, *Sol. Energ. Mat. Sol. C.* 95, 6 (2010).
99. G. Gu, V. Bulović, P. E. Burrows, S. R. Forrest and M. E. Thompson, *Appl. Phys. Lett.* 68, 2606 (1996).
100. P. Görrn, M. Sander, J. Meyer, M. Kröger, E. Becker, H. H. Johannes, W. Kowalsky and T. Riedl, *Adv. Mater.* 18, 738 (2006).
101. A. Yamamori, S. Hayashi, T. Koyama and Y. Taniguchi, *Appl. Phys. Lett.* 78, 3343 (2001).
102. M. Pfeiffer, S. R. Forrest, X. Zhou and K. Leo, *Org. Electron.*, 4, 21 (2003).
103. S. Han, X. Feng, Z. H. Lu, D. Johnson and R. Wood, *Appl. Phys. Lett.* 82, 2715 (2003).
104. J. Lewis, S. Grego, B. Chalamala, E. Vick and D. Temple, *Appl. Phys. Lett.* 85, 3450 (2004).
105. S. Y. Ryu, J. H. Noh, B. H. Hwang, C. S. Kim, S. J. Jo, J. T. Kim, H. S. Hwang, H. K. Baik, H. S. Jeong, C. H. Lee, S. Y. Song, S. H. Choi and S. Y. Park, *Appl. Phys. Lett.* 92, 023306 (2008).
106. K. S. Yook, S. O. Jeon, C. W. Joo and J. Y. Lee, *Appl. Phys. Lett.* 93, 013301 (2008).

107. J. Lee, S. Hofmann, M. Furno, M. Thomschke, Y. H. Kim, B. Lüsse and K. Leo, *Opt. Lett.* 36, 1443 (2011).
108. J. Meyer, T. Winkler, S. Hamwi, S. Schmale, H.-H. Johannes, T. Weimann, P. Hinze, W. Kowalsky and T. Riedl, *Adv. Mater.* 20, 3839 (2008).
109. H. H. Hsieh, T. T. Tsai, C. Y. Chang, S. F. Hsu, C. S. Chuang and Y. Lin, *J. Soc. Inf. Display*, 19, 323 (2011).
110. S. Ju, J. F. Li, J. Liu, P. C. Chen, Y. G. Ha, F. Ishikawa, H. Chang, C. W. Zhou, A. Facchetti, D. B. Janes and T. J. Marks, *Nano Lett.* 8, 997 (2008).
111. T. Dobbertin, O. Werner, J. Meyer, A. Kammoun, D. Schneider, T. Riedl, E. Becker, H. H. Johannes and W. Kowalsky, *Appl. Phys. Lett.* 83, 5071 (2003).
112. T. Dobbertin, M. Kroeger, D. Heithecker, D. Schneider, D. Metzendorf, H. Neuner, E. Becker, H. H. Johannes and W. Kowalsky, *Appl. Phys. Lett.* 82, 284 (2003).
113. V. Bulović, P. Tian, P. E. Burrows, M. R. Gokhale, S. R. Forrest, and M. E. Thompson, *Appl. Phys. Lett.* 70, 2954 (1997).
114. G. Parthasarathy, C. Adachi, P.E. Burrows, and S.R. Forrest, *Appl. Phys. Lett.* 76, 2128 (2000).
115. S. K. Deb, *Philos. Mag.* 27, 801 (1973).
116. L. S. Liao, W. K. Slusarek, T. K. Hatwar, M. L. Ricks, and D. L. Dustin, *Adv. Mater. (Weinheim, Ger.)* 20, 324 (2008).
117. L. S. Liao and K. P. Klubek, *Appl. Phys. Lett.* 92, 223311 (2008).
118. Y. K. Kim, J. W. Kim and Y. Park, *Appl. Phys. Lett.* 94, 063305 (2009).
119. S. M. Park, Y. H. Kim, Y. Yi, H.-Y. Oh, and J. W. Kim, *Appl. Phys. Lett.* 97, 063308 (2010).
120. Measured by spectroscopic ellipsometer.

121. R. Chance, A. Prock and R. Silbey, *Adv. Chem. Phys.* 1 (1978).
122. S.-Y. Kim and J.-J. Kim, *Org. Electron.* 11, 1010 (2010).
123. P. Szalay, J. Galán-Mascarós, R. Clerac and K. Dunbar, *Synth. Met.* 122, 535 (2001).
124. P. Frank, T. Djuric, M. Koini, I. Salzmann, R. Rieger, K. Müllen, R. Resel, N. Koch and A. Winkler, *J. Phys. Chem. C.* 114, 6650 (2010).
125. P. Szalay, J. Galan-Mascaros, B. Schottel, J. Bacsa, L. Perez, A. Ichimura, A. Chouai and K. Dunbar, *J. Cluster Sci.* 15, 503 (2004).
126. S. Lee, J.-H. Lee, J.-H. Lee and J.-J. Kim, *Adv. Funct. Mater.* 22, 855 (2012).
127. W. S. Jeon, J. S. Park, L. Li, D. C. Lim, Y. H. Son, M. C. Suh, J. H. Kwon, *Org. Electron.* 13, 939 (2012).
128. D.M de Leeuw, M.M.J Simenon, A.R Brown, R.E.F Einerhand, *Synth. Met.* 87, 53 (1997).
129. T. Matsushima, H. Murata, *Appl. Phys. Lett.* 95, 203306 (2009).
130. J. Blochwitz, T. Fritz, M. Pfeiffer, K. Leo, D. M. Alloway, P. A. Lee, N. R. Armstrong, *Org. Electron.* 2, 97 (2001).
131. W. Gao, A. Kahn, *Org. Electron.* 3, 53 (2002).
132. M. Kröger, S. Hamwi, J. Meyer, T. Riedl, W. Kowalsky, A. Kahn, *Org. Electron.* 10, 932 (2009).
133. J.-H. Lee, H.-M. Kim, K.-B. Kim, J.-J. Kim, *Org. Electron.* 12, 950 (2011).
134. Z. B. Wang, M. G. Helander, M. T. Greiner, J. Qiu, and Z. H. Lu, *Phys. Rev. B* 80, 235325 (2009).
135. M. T. Greiner, M. G. Helander, W.-M. Tang, Z.-B. Wang, J. Qiu and Z.-H. Lu, *Nat. Mater.* 11, 76 (2011).

136. T. Chiba, Y.-J. Pu, R. Miyazaki, K.-I Nakayama, H. Sasabe, J. Kido, *Org. Electron.* 12, 710 (2011).
137. B. B. Diouf, W. S. Jeon, J. S. Park, J. W. Choi, Y. H. Son, D. C. Lim, Y. J. Doh, J. H. Kwon, *Synth. Met.* 161, 2087 (2011).
138. K. S. Yook, B. D. Chin, J. Y. Lee, B. E. Lassiter, and S. R. Forrest, *Appl. Phys. Lett.* 99, 043308 (2011).
139. M. Zhang, H. Wang, C. W. Tang, *Org. Electron.* 13, 249 (2012).
140. J.-H. Lee, S. Lee, J.-B. Kim, J. Jang, and J.-J. Kim, *J. Mater. Chem.* 22, 15262 (2012).
141. B. Bröker, O. T. Hofmann, G. M. Rangger, P. Frank, R.-P. Blum, R. Rieger, L. Venema, A. Vollmer, K. Müllen, J. P. Rabe, A. Winkler, P. Rudolf, E. Zojer, and N. Koch, *Phys. Rev. Lett.* 104, 246805 (2010).
142. P. Frank, N. Koch, M. Koinia, R. Rieger, K. Müllen, R. Resel, A. Winkler, *Chem. Phys. Lett.* 473, 321 (2009).
143. H. J. Kim, J. W. Kim, J.-J. Kim, *Electron. Mater. Lett.* 7, 93 (2011).
144. H. J. Kim, J. W. Kim, H. H. Lee, T.-M. Kim, J. Jang, J.-J. Kim, *J. Phys. Chem. Lett.* 2, 1710 (2011).
145. J. Cui, Q. Huang, J. C. G. Veinot, H. Yan, Q. Wang, G. R. Hutchison, A. G. Richter, G. Evmenenko, P. Dutta, T. J. Marks, *Langmuir* 18, 9958 (2002).
146. M. Tolan, *in X-ray Scattering from Soft-Matter Thin Films* 1999, Ch. 2.
147. C. Thompson, G. Palasantzas, Y. P. Feng, S. K. Sinha, J. Krim, *Phys. Rev. B* 49, 4902 (1994).
148. R. Gavrila, A. Dinescu, D. Mardare, *Rom. J. Inform. Sci. Technol.* 10, 291 (2007).

149. P. Langevin, *Ann. Chim. Phys* 28, 122 (1903).
150. R. N. Hall, *Phys. Rev.* 87, 387 (1952).
151. W. Shockley and W. Read Jr, *Phys. Rev.* 87, 835 (1952).
152. M. Kuik, L. J. A. Koster, G. A. H. Wetzelaer, and P. W. M. Blom, *Phys. Rev. Lett.* 107, 256805 (2011).
153. M. Kuik, H. T. Nicolai, M. Lenes, G.-J. A. H. Wetzelaer, M. Lu, and P. W. M. Blom, *Appl. Phys. Lett.* 98, 093301 (2011).
154. P. A. Lane, L. C. Palilis, D. F. O'Brien, C. Giebeler, A. J. Cadby, D. G. Lidzey, A. J. Campbell, W. Blau, and D. D. C. Bradley, *Phys. Rev. B* 63, 235206 (2001).
155. J. Mäkinen, I. G. Hill, and Z. H. Kafafi, *J. Appl. Phys.* 92, 1598 (2002).
156. X. Gong, J. C. Ostrowski, D. Moses, G. C. Bazan, and A. J. Heeger, *Adv. Funct. Mater.* 13, 439 (2003).
157. A. J. Sandee, C. K. Williams, N. R. Evans, J. E. Davies, C. E. Boothby, A. Köhler, R. H. Friend, A. B. Holmes, *J. Am. Chem. Soc.* 126, 7041 (2004).
158. G. He, M. Pfeiffer, K. Leo, M. Hofmann, J. Birnstock, R. Pudzich, and J. Salbeck, *Appl. Phys. Lett.* 85, 3911 (2004).
159. H. Yersin, *Top. Curr. Chem.* 241, 1 (2004).
160. R. Liu, Z. Gan, R. Shinar, J. Shinar, *Phys. Rev. B*, 83, 245302 (2011).
161. C. Weichsel, L. Burtone, S. Reineke, S. I. Hintschich, M. C. Gather, K. Leo, and B. Lüssem, *Phys. Rev. B* 86, 075204 (2012).
162. M. A. Baldo, S. Lamansky, P. E. Burrows, M. E. Thompson, and S. R. Forrest, *Appl. Phys. Lett.* 75, 4 (1999).
163. M. A. Baldo, M. E. Thompson, and S. R. Forrest, *Nature* 403, 750 (2000).

164. Z. G. Gao, B. X. Mi, H. L. Tam, K. W. Cheah, C. H. Chen, M. S. Wong, S. T. Lee, and C. S. Lee, *Adv. Mater.* 20, 774 (2008).
165. W. S. Jeon, T. J. Park, S. Y. Kim, R. Pode, J. Jang, J. H. Kwon, *Org. Electron.* 10, 240 (2009).
166. Z. B. Wang, M. G. Helander, J. Qiu, D. P. Puzzo, M. T. Greiner, Z. W. Liu, and Z. H. Lu, *Appl. Phys. Lett.* 98, 073310 (2011).
167. M. A. Baldo, C. Adachi, and S. R. Forrest, *Phys. Rev. B* 62, 10967 (2000).
168. J. Kalinowski, W. Stampor, J. Mężyk, M. Cocchi, D. Virgili, V. Fattori, and P. Di Marco, *Phys. Rev. B* 66, 235321 (2002).
169. S. Reineke, K. Walzer, and K. Leo, *Phys. Rev. B* 75, 125328 (2007).
170. D. Song, S. Zhao, Y. Luo, and H. Aziz, *Appl. Phys. Lett.* 97, 243304 (2010).
171. P. Ashburn, D. Morgan, and M. Howes, *Solid-State Electron.* 18, 569 (1975).
172. G. A. H. Wetzelaer, M. Kuik, H. T. Nicolai, and P. W. M. Blom, *Phys. Rev. B* 83, 165204 (2011).
173. V. Savvateev, A. Yakimov, and D. Davidov, *Adv. Mater.* 11, 519 (1999).
174. C. W. Ma, O. Lengyel, J. Kovac, I. Bello, C. S. Lee, S. T. Lee, *Chem. Phys. Lett.* 397, 87 (2004).
175. H. Kajii, K. Takahashi, J.-S. Kim, and Y. Ohmori, *J. J. Appl. Phys.* 45, 3721 (2006).
176. W. Brütting, H. Riel, T. Beierlein, and W. Riess, *J. Appl. Phys.* 89, 1704 (2001).
177. S. Nowy, W. Ren, A. Elschner, W. Lövenich, and W. Brütting, *J. Appl. Phys.* 107, 054501 (2010).
178. K. S. Yook, S. O. Jeon, S. Y. Min, J. Y. Lee, H. J. Yang, T. Noh, S. K. Kang, and T. W. Lee, *Adv. Funct. Mater.* 20, 1797 (2010).

초 록

차세대 디스플레이 및 조명 구현을 위해서 최근 유연한 소자 및 투명 유기발광 소자에 대한 연구가 활발하게 진행되고 있는데, 고효율의 유연한 소자를 구현하기 위해서는 기존의 공정 조건과 다른 큰 변화가 이뤄져야 한다. 대표적으로, 부러지기 쉬운 유리 기판에서 유연성이 좋은 플라스틱 기판으로의 대체가 불가피한데, 플라스틱 기판은 온도에 민감하기 때문에 공정 조건을 200℃ 이하로 낮추어야 공정에서의 손상을 최소화할 수 있다. 플라스틱 기판 위에 구동 회로 및 유기 발광 소자 형성 시 저온 공정 조건에서도 전하 이동도 특성이 좋고 유연성 및 대면적 공정에도 유리한 산화물 박막 트랜지스터와 인버티드 유기발광 소자의 조합이 가장 이상적이라 생각되고 있는데, 안타깝게도 현재로서는 인버티드 유기 발광 소자의 효율이 일반 소자에 비해 50% 이상 떨어지기 때문에 이를 극복하기 위해 일반 구조의 유기 발광 소자와 더불어 복잡한 보상회로가 추가적으로 이용되고 있다. 만약, 인버티드 소자의 효율을 대폭 향상시킬 수 있다면, 간단하면서도 새로운 구조를 가진 발광 소자를 구현할 수 있기 때문에 디스플레이 및 조명으로의 응용에 있어서 지평을 넓힐 수 있을 것이라 예상된다.

본 학위 논문에서는, 인버티드 유기 발광 소자의 효율을 극대화하기 위해 극복해야 할 문제들에 대해 논의하고, 이를 바탕으로 이상적인 소자 구조를 제안하였으며, 더불어 고효율의 소자가 구동되는 메커니즘에 대한 분석 결과를 상세히 기술하였다.

인버티드 소자에서의 핵심 쟁점은 바닥전극에서 유기물 층으로의 전자 주입 문제이다. 원활한 전자주입을 위해 n-도핑을 이용한 연구가 많이 진행되었고, 금속 전극과 도핑된 유기물 층 계면연구가 활발히 진행되어 왔다. 그럼에도 불구하고 여전히 16% 이하의 낮은 효율의 인버티드 소자들이 보고되었는데, 이것의 원인을 밝히고 더불어 소자 효율을 향상시키기 위해 제 2 장에서는 금속/도핑된 유기물 층 계면 뿐만 아니라 도핑된 유기물/유기물 층 계면 장벽의 중요성에 대한 연구를 진행하였다. 그 결과 도핑된 유기물/유기물 층 계면 장벽이 전류-전압 특성에 큰 영향을 주는 것을 밝혔고, B3PYMPM 물질을 이용해 동종 접합 계면의 전자 주입 장벽을 줄여 20%의 외부 발광 효율 및 80 lm/W 의 전력효율을 가진 인버티드 소자를 구현하였으며, 이는 세계 최고 효율을 가진 인버티드 소자에 해당한다.

제 3 장에서는 바닥 전극의 일함수에 구애 받지 않고 전자를 주입할 수 있는 새로운 전자 주입 구조로써, 유기물 이중 p-n 접합을 제안하였다. 0.3V 의 낮은 역방향 전압에서 $100\text{mA}/\text{cm}^2$ 의 높은 전류를 생성하는 p-CuPC 와 Bphen 으로 이뤄진 유기물 이중 접합을 이용하여 바닥전극의 종류에 무관하게 전자를 주입할 수 있는 방법을 고안하였고, 유연한 디스플레이 구현에 큰 이점을 줄 것이라 예상한다.

고품질 인버티드 소자 구현을 위해서는 전자 주입과 더불어 구조적인 관점에서 상부 투명전극을 형성하는 것 또한 중요한데, 이를 위해 제 4 장에서는 고품위 투명 유기 발광 다이오드 구현을 위한 유기물 완충층에 대한 연구 및 결과를 기술하였다. 상부 투명전극 형성 시 스퍼터 공정 과정에서 유기물들이 심하게 손상되는 문제가 있어, 이를 해결하기 위한 방안으로 HATCN 이라는 새로운 물질을 유기물 완충층에 도입하였다. 그 결과 유기물 손상 없이 IZO 투명 전극을 효과적으로 형성하였고, 이를 투명 유기 발광 소자에 접목시켜 $67\text{ cd}/\text{A}$, $67\text{ lm}/\text{W}$ 의 고효율을 가진 투명소자를 구현하였다. 소자의 평균 투과도 또한 81%로 매우 높은 값을 보이고 있는데, 이는 HATCN 이 완충층 및 정공 주입, 그리고 광학적 특성이 모두 좋기 때문이다.

제 5 장에서는 HATCN 이 IZO 형성과정에서 유기물을 효과적으로 막아줄 수 있었던 이유에 대해 구조적으로 접근하여 해석한 결과를 명시하였다. 엑스레이 분석을 통해 HATCN 박막의 구조 및 분자 배열에 관해 분석하였고, 그 결과 HATCN 은 유기물 층 위에 $(001)_{\text{hex}}$ 방향으로 배향이 주로 되어 있는 것을 알 수 있었고, 이는 IZO 투명 전극 형성 후에도 계속 유지가 됨을 확인하였다. 즉, HATCN 의 특정 배향 및 성장에 의해 강한 스퍼터 에너지로부터 하부 유기물을 효과적으로 보호할 수 있음을 분석하였다.

앞서 기술한 전자 주입 특성, 효과적인 상부 투명 전극 형성 기술을 바탕으로 엑시플렉스를 형성하는 호스트를 도입하여 $110\text{ cd}/\text{A}$, 24% 의 외부발광효율을 보이는 인버티드 상부 유기 발광 소자를 제작하였다. 이 소자는 고휘도에서의 효율 감소 또한 매우 작은 특성을 보이고 있는데, 이러한 특성을 가지는 이유에 대해 원인을 분석하였고, 이를 제 6 장에서 논의하였다. 확산 전류가 우세한 영역에서의 전류-전압-휘도 특성 분석, 트랜지언트 발광 특성, 캐패시턴스 특성 분석을 통해 CBP 단일 호스트와는 달리 엑시플렉스 공동 호스트에서는 Langevin 결합이 trap-assisted 결합 보다 우세함을 분석하였고, 소자 구동 시 내부에 쌓이는 전하가 상대적으로 작은 것을 확인하였다. 따라서 엑시플렉스를 형성하는 공동 호스트를 소자에 적용할 경우, 도펀트의 에너지

레벨에 속박된 전하량이 적어져서 좋은 클-오프 특성과 낮은 구동 전압을 동시에 만족하는 궁극적인 유기발광 소자를 제작할 수 있음을 밝혔다.

주요어 : 인버티드 유기 발광 다이오드, 투명 발광 다이오드, 유연한 소자, 전하 결합 및 발광 기작, 전자 주입 특성

학 번 : 2010-30783